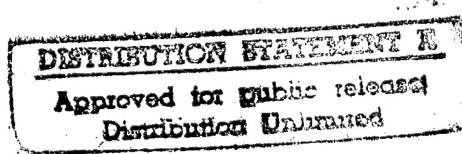


UNIVERSITY OF Miami

February 27, 1996

Dr. Jeffrey Simmen
ONR 3210A
Office of Naval Research
Ballston Centre Tower One
800 North Quincy Street
Arlington, VA 22217-5660



Dear Dr. Simmen:

Enclosed please find three copies of Dr. Tokuo Yamamoto's Final Technical Report for our ONR Contract No. N00014-89J-1146 entitled "Measurement and Modeling of Low Frequency Acoustic Wave Propagation and Scattering in Shallow Water with Comprehensive Subbottom Structure" and publications generated from this grant.

We hope the report is satisfactory for your needs.

Sincerely,



Anne M. Hoey
Administrative Assistant

cc: Administrative Grants Officer, Regional Office Atlanta (1)
Director of Naval Research Laboratory, Code 2627 (1)
 Defense Technical Information Center (2)
Office of Naval Research ONR 00CC1 (Patent)

19960305 014

Rosenstiel School of Marine and Atmospheric Science
Division of Applied Marine Physics
4600 Rickenbacker Causeway
Miami, Florida 33149-1098
Office 305-361-4160
Fax 305-361-4701

100% QUALITY INSPECTED 1

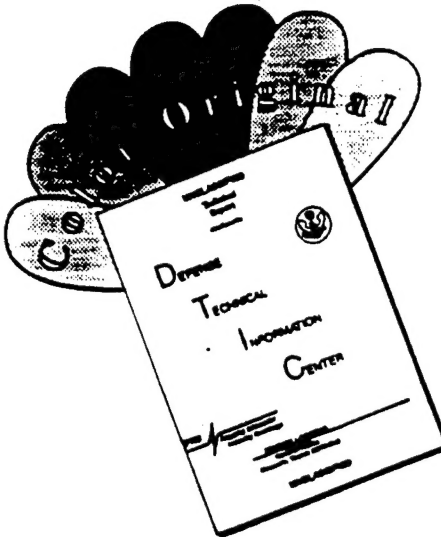
REPORT DOCUMENTATION PAGE

FORM APPROVED
OMB No. 0704-0183

Public reporting burden for this collection of information is estimated to average 1 hour per response, including the time for reviewing instructions, searching existing data sources, gathering and maintaining the data needed and completing and reviewing the collector, of information. Send comments regarding this burden estimate or any other aspect of the collection of information, including suggestions for reducing the burden to Washington Headquarters Services, Directorate for Information Operations and Reports, 1215 Jefferson Davis Highway, Suite 1204, Arlington, VA 22202-4302 and to the Office of Management and Budget, Paperwork Reduction Project (0704-0183), Washington, DC 20503.

1. AGENCY USE ONLY (Leave blank)	2. REPORT DATE	3. REPORT TYPE AND DATES COVERED	
	2/23/96	Final Technical Report 10/1/92-9/30/95	
4. TITLE AND SUBTITLE OF REPORT		5. FUNDING NUMBERS	
Measurement and Modeling of Low Frequency Acoustic Wave Propagation and Scattering in Shallow Water with Comprehensive Subbottom Structure		N0001489J-1146	
6. AUTHOR(S)		7. PERFORMING ORGANIZATION NAME(S) AND ADDRESS(ES)	
Measurements		Rosenstiel School of Marine and Atmospheric Sciences University of Miami 4600 Rickenbacker Causeway Miami, Florida 33149	
8. SPONSORING/MONITORING AGENCY NAME(S) AND ADDRESS(ES)		9. PERFORMING ORGANIZATION REPORT NUMBER:	
Office of Naval Research Ballston Tower One 800 North Quincy Street Arlington, Virginia 22217-5660		668432	
11. SUPPLEMENTARY NOTES: N/A			
12a. DISTRIBUTION AVAILABILITY STATEMENT		12b. DISTRIBUTION CODE	
Unlimited			
13. ABSTRACT (Maximum 200 words) A high resolution acoustic crosswell tomography technique was developed for accurate measurements of variabilities of density, velocity, shear strength and permeability within the sediments. An analytical expression for the three-dimensional wave number spectra of these sediment properties has been obtained. Acoustics scattering from sediment volume has been obtained as a function of the three dimensional spectra of velocity and density variabilities. Work continues to quantify the relation between the variabilities of sediment properties and acoustic bottom scattering. A method to measure the ocean wave directional spectra using a single buried ocean bottom seismometer and a pressure sensor has been developed and sea-tested successfully.			
14. SUBJECT TERMS		15. NUMBER OF PAGES:	
		16. PRICE CODE	
17. SECURITY CLASSIFICATION OF REPORT: Unclassified	18. SECURITY CLASSIFICATION OF THIS PAGE	19. SECURITY CLASSIFICATION OF ABSTRACT	20. LIMITATION OF ABSTRACT

DISCLAIMER NOTICE



THIS DOCUMENT IS BEST
QUALITY AVAILABLE. THE COPY
FURNISHED TO DTIC CONTAINED
A SIGNIFICANT NUMBER OF
COLOR PAGES WHICH DO NOT
REPRODUCE LEGIBLY ON BLACK
AND WHITE MICROFICHE.

MEASUREMENTS AND MODELING OF LOW FREQUENCY ACOUSTIC WAVE PROPAGATION AND SCATTERING IN SHALLOW WATER WITH COMPREHENSIVE SUBBOTTOM STRUCTURE MEASUREMENTS

SUMMARY OF RESULTS

Work has been focused on the field measurements of the velocity fluctuation and the geoacoustic properties within the seabed using the cross-well tomography and the 3-D reflection-scattering system, "Kite", and modeling of the acoustic wave scattering by the velocity fluctuation within the sediment volume.

Considerable efforts also went into the data analysis and publication of the SAMSON data on the gravity wave and microseism generation and propagation, and the broadband OBS data on the pressure and seismic pulse generated by passage of ships. Publications generated from this grant are listed at the end of this report. Publications (1,10,11,12,15) are attached with this report.

1. Acoustic Cross-Well Tomography and Propagation/Scattering Experiments

We have successfully developed the high resolution cross-well acoustic tomography method for the purpose of imaging the structure of the ocean bottom using the pulse compression technique. Using the phase modulated pseudo-random binary sequence codes, one can generate and propagate a narrow bandwidth acoustic pulse simulating a laser-like acoustic pulse. Simply changing the carrier frequency, we can measure the acoustic wave propagation through sediments one frequency at a time without suffering the pulse degradation due to the velocity dispersion. We have successfully applied this technique to extract the permeability image of the Florida-Bahamas Carbonate Platform near Ft. Myers, Florida. The velocity of the mud layer does not change much among the different frequencies indicating the impermeable nature of this layer. The limestone layer shows high contrast from 1kHz to 250 Hz indicating the large permeability on the order of 300 darcies which agrees with a direct permeability measurement of this layer. The sand layer shows less velocity dispersion; an indication of less permeability. The velocity fluctuation within the F-B Platform is very strong

of the order of +/-75% of the mean which generates strong scattering of the acoustic waves. The 3-D wave number spectra of the velocity fluctuation within the volume for various sediment provinces have been generated from the laser acoustic cross-well experiments. Our data are the only 3-D wave number spectra data measured; thus widely used for volume scattering calculations. The laser tomography method has been published in GEOPHYSICS [1]. This paper earned a best paper award by the Society of Exploration Geophysicist. The results from the Florida-Bahamas Platform experiments were presented at 1994 SEG Meeting [2] and in another GEOPHYSICS paper [15].

The propagation and scattering of the acoustic waves at frequencies from 100 to 10,000Hz through ocean bottom sediments has been experimented at the Florida-Bahamas Carbonate Platform, near Ft. Myers. The incidents waves, the reflected waves, the refracted waves and the scattered waves are identifiable and they create a very complicated wave field all together. This technique is very useful for studying the acoustic wave scattering within the sediment volume. The results was presented in an invited paper [3] for the 1994 ASA Spring Meeting. A US patent (No. 5,142,500) was awarded for the acoustic crosswell tomography.

2. 3-D High Resolution Reflection/Scattering System 'Kite'

The 48-ch hydrophone array geometry of 'Kite' was built and sea-tested. The unique array configuration enables us to form a very narrow beam (3 degree at .1kHz) which can be steered 180 degrees. A broadband (.1 to 20kHz) 210 dB programmable projector and airguns were used as the sources. When towed behind a ship, the 'Kite' surveys the 4 km wide path of water column and subbottom reflectors and scatters at a speed of up to 6 knots. The penetration depth is 5 km below the seafloor and the resolution as high as 10 cm near the seafloor. The results have been presented at 1992 ASA [4] and 1993 SEG [5] meetings and a paper is pending for publication in GEOPHYSICS [6].

3. Analysis of Acoustic Wave Scattering from Sediment Volume

An exact solution for a plane acoustic wave scattered by a randomly fluctuating sediment with a constant vertical velocity gradient has been obtained analytically [7] . The measured 3-D wave number spectra from the cross-well tomography of the seabed sediments are used in the calculations. The silt bottom shows approximately 20 dB stronger backscattering strength as compared to the sand bottom because the velocity fluctuation in the silt bottom is of the order of +/-25% of the mean velocity where as it is only +/-5 % in the sand bottom. The velocity fluctuation of the carbonate bottom is of the order of +/- 50% and the backscattering strength is 20 dB more than the silt bottom. These comparisons strongly suggest that the measurements of the scattering strengths of the bottom sediments, through inverse analyses, will provide sediment properties accurately and quickly. Two M.S. theses [7,8] and a Ph.D. thesis [9] have been generated on this subject. One JASA paper [10] has been published. Work continues to quantify the physics of bottom backscatter.

4. SAMSON and NSWC data analyses

The 100 day continuos data from the 6-point buried OBS arrays during the ONR SAMSON Experiments has been analyzed and published in two papers; one in JGR Ocean [11] and one in ASEC Journal of Ocean, etc. [12] . One Ph.D. [13] degree has been awarded. A US patent (no. 5,243,565) was awarded for the buried ocean wave directional spectrometer.

The data from the broadband buried OBS Experiments at the Chesapeake Bay has been analyzed. A M.S. thesis [14] and a classified report has been generated from the work. A new sensing technique of moving objects has been found and NSWC has built many broadband buried OBSs for their future research.

PUBLICATION LIST

- [1] YAMAMOTO, T., NYE, T., AND KURU, M., 1994, Porosity, permeability, shear strength: cross-swell tomography below an iron foundry: *Geophysics*, 59(10), pp 1530-1531.
- [2] Yamamoto, T., Nye, T., and Kuru, M., 1994, Permeability structure within a limestone aquifer imaged by cross-well acoustics tomography at multiple

frequencies: Expanded abstracts, the 64th SEG annual meeting.

[3] Yamamoto, T., 1994, Porosity, permeability, shear strength images of the seabed measured through acoustic cross-well experiments: Invited Paper, ASA 1994 Spring Meeting.

[4] Yamamoto, T., and Shon, H., 1992, Data processing for high resolution 3-D subbottom imaging system 'Kite' : ASA Spring Meeting.

[5] Rogers, A., Yamamoto, T., Shon, H., and Shi, W., 1993, The high resolution 3-D seismic survey system 'Kite' : Expanded Abstracts, the 63rd SEG annual meting, 531-535.

[6] Yamamoto, T., and Shon, H., 1993, Data processing for high resolution 3-D subbottom imaging system 'Kite' : Geophysics, submitted.

[7] Shi, W., 1993, Acoustic backscattering in the ocean due to density and sound velocity fluctuations in sediments: M.S. Thesis, University of Miami, Coral Gables, FL. (T. Yamamoto, adviser)

[8] Rogers, A., 1992, Experimental study of the sediment effect on acoustic wave propagation in the shallow ocean: M.S. Thesis, University of Miami, Coral Gables, FL. (T. Yamamoto, adviser)

[9] Briggs, K.B., 1994, High-frequency acoustic scattering from sediment interface roughness and volume inhomogeneities: Ph.D. Thesis, University of Miami, Coral Gables, FL.(T. Yamamoto, adviser)

[10] Rogers, A., Yamamoto, T., and Carey, W., 1993, Experimental investigation of sediment effect on acoustic wave propagation in the shallow ocean: Journal of Acoustical Society of America, 93 (4), 1747-1761.

[11] Nye, T. and Yamamoto, T., 1994, Concurrent measurements of the directional spectra of microseismis energy and surface gravity waves:

Journal of Geophysical Research, Oceans, 99(c7) pp
14321-14338.

- [12] Nye, T. and Yamamoto, T., 1994, Field test of the buried ocean wave directional spectrometer (BOWDS) system: Journal of Waterway, Port, Coastal, and Ocean Engineering, 120(5) pp 451-467.
- [13] Nye, T., 1992, Measurements of the directional spectra of surface gravity waves and seafloor microseisms using a pressure sensor and two buried horizontal seismometers, Ph.D. Thesis, University of Miami, Coral Gables, FL. (T. Yamamoto, adviser).
- [14] Theophanis, S., 1993, Measurements of broad band seismicity and their applications in the Chesapeake Bay: M.S. Thesis, University of Miami, Coral Gables, FL. (T. Yamamoto, adviser).
- [15] Yamamoto, T., Nye, T., and Kuru, M., 1995, Imaging the permeability structure of a limestone aquifer by crosswell acoustic tomography: Geophysics, 60 (6) pp 1634-1645.

Experimental investigation of sediment effect on acoustic wave propagation in the shallow ocean

Andrew K. Rogers and Tokuo Yamamoto

University of Miami, Geoacoustic Laboratory, Rosenstiel School of Marine and Atmospheric Science, 4600 Rickenbacker Causeway, Miami, Florida 33149-1098

William Carey

Defense Advanced Research Projects Agency, 3701 N. Fairfax Drive, Arlington, Virginia 22203-1714

(Received 5 February 1992; revised 28 August 1992; accepted 2 December 1992)

In shallow water the sediment layers have very strong effects on the propagation of acoustic waves. An effort to study the effects of the sediment has been made using 50- to 600-Hz continuous wave acoustic propagation data taken by Carey ["Hudson canyon experiment," FY88 Ocean Acoustic report, NUSC (1988)] at the Atlantic margin coring project (AMCOR) borehole 6010 off the coast of New Jersey combined with sediment properties measured at that site by Yamamoto *et al.* ["Experimental verification and application of bottom shear modulus profile (BSMP) method," *Oceans '91 Proceedings* (1991)] of the University of Miami Geoacoustic Laboratory using the bottom shear modulus profiler (BSMP) method. Excellent agreement was found between the model and data indicating the acceptability of BSMP sediment values as input for acoustic propagation studies. The introduction of shear or tangential stresses in the model was found to have no effect upon which modes propagated but only on their modal intensity. The higher the order of the mode the greater the penetration in the seafloor and the stronger the shear effect on the intensity. A sub-seafloor acoustic waveguide was investigated for the site and found to give possible explanation for enhanced intensity of modes that propagate strongly within that region. The intrinsic attenuation was determined using a method of matching modal intensity from model calculations with measured data. Biot theory was utilized and depth-dependent intrinsic sediment attenuation profiles were found for seven frequencies between 50 and 600 Hz. The depth-averaged attenuation for the first mode at each frequency and the first mode that penetrates to 100 m was found. The frequency dependence of the mode attenuation was determined. The attenuation values agreed well with previous experimental acoustic reflection data taken by Mitchell and Focke [J. Acoust. Soc. Am. 67, 1582-1589 (1980)] but were much lower than values for attenuation in this frequency range determined by Hamilton's [Geophysics 36, 266-284 (1971)] extrapolation of high-frequency laboratory and field measurements to the <1-kHz range. The effect of interface and volume scattering on transmission loss was determined using the acoustic model and a thin layer representation of the scattering interface. The result showed scattering to significantly contribute to energy loss beyond a kilometer or so and to have increased significance as frequency is increased.

PACS numbers: 43.30.Ma, 43.30.Bp

INTRODUCTION

The study of acoustic propagation requires knowledge of the properties of the acoustic environment. In the ocean these properties include sound-speed profiles, boundary roughnesses, and attenuation profiles for the various media constituting the area of study. Much effort is made to obtain accurate measurements of these properties some of which are more easily obtained than others. The first thorough and quantitative analysis of sound propagation in shallow water was made by Pekeris.¹ His idealized model was based upon a constant, lossless water layer overlying a semi-infinite fluid layer with higher sound velocity and density. He also gave a less-detailed treatment of a three-layer model. The Pekeris model was extended by Tolstoy^{2,3}

to apply to a many layered environment. Tolstoy assumed many homogeneous layers with constant sound velocity and density.

In the 1960's propagation loss mechanisms were introduced into the model, first by Tolstoy,⁴ who assumed an elastic bottom including absorption, and later rough surface scattering was developed by Clay.⁵

The 1970's saw the introduction of digital computers and the ability to handle large numerical problems more efficiently with their use. Arbitrary sound-speed and attenuation profiles were put into the acoustic model by Inginito.⁶ The study of attenuation in ocean sediments was also pursued by Hovem.⁷ A large quantity of work on attenuation was performed during the 70's by Hamilton^{8,9} and Stoll¹⁰ using the Biot theory.^{11,12} This theory of acoustic propagation in porous media gives the losses due to the

relative movement of the fluid and the skeletal frame and loss due to grain to grain friction. More recently work by Jensen and Kuperman¹³ has presented shallow water optimum frequency predictions.

Furthering the work of Inginito,⁶ and Mitchell and Focke¹⁴ examined the frequency dependence of attenuation in deep ocean marine sediments. The most comprehensive compilations of the work on attenuation in marine sediments have been put together by Hamilton¹⁵ and Kibblewhite.¹⁶

Yamamoto¹⁷ has used Biot theory to set criteria for different sediment types. Biot's work was extended by Yamamoto and Turgut¹⁸ by deriving mathematical expressions for the intrinsic permeability and the viscous correction factor.

Recent work has produced several acoustic propagation computer codes. Of particular importance to this paper is the seismo-acoustic propagation code SAFARI developed by Schmidt.¹⁹ SAFARI solves the isotropic elastic seabed problem using the depth-dependent Green's function. A version of the parabolic equation code using the split-step method has also been under continued development for several years by Tappert.²⁰ A normal mode code SNAP has also been developed at SACLANTCEN.²¹

Particular interest in this paper is put upon the development of one of the more elusive of acoustic properties, the attenuation profile. During the development of the attenuation model several other properties of the acoustic environment are also observed and discussed, such as the effect of the sound-speed profile and sediment layer inhomogeneities.

The seabottom parameter that has the strongest effect upon acoustic propagation is the compressional wave velocity profile. The acoustic impedance is the main influence on acoustic penetration into the seabed. Shear waves in the sediment also influence the acoustic penetration but with considerably less effect. The greater the penetration depth the greater the effect that the sediment layers have upon the acoustic propagation. Once within the seabottom the acoustic energy is either reflected or refracted back into the water column or dispersed by strong loss mechanisms in the bottom. The amount of loss within the bottom is controlled primarily by the sediment attenuation profile. The meaning of the word attenuation is sometimes vague. For the purpose of clarity we will say that it is considered here as "that portion of the decrease in seismic or sonar signal strength with distance not depending upon geometrical spreading. This decrease depends on the physical characteristics of the transmitting media, involving reflection, scattering, and absorption."²² Attenuation of the propagating energy is a function of both distance traveled and frequency and is often approximated as:

$$\alpha(x,y,z) = b(x,y,z) f^m. \quad (1)$$

Here, α is attenuation in dB per unit distance, b is a constant of proportionality, and f is frequency. The factor m usually ranges from less than 1 to around 2 depending upon sediment type and analysis technique. There has been very little experimental data available for attenuation anal-

ysis, particularly in the low-frequency (< 1 kHz) range. Because of this the values for attenuation of different sediment types have not as yet been fully established.¹⁴ A compilation of much of the existing data available was put together by Hamilton,¹⁵ Kibblewhite,¹⁶ and Stoll.²³ It is rare to have both experimentally measured sediment profiles and acoustic propagation data for the same area as is the case here. It is one objective of this study to make a contribution of experimental *in situ* data to the low-frequency attenuation database.

Over the last 6 years the University of Miami Geodynamics group has been involved in an ongoing investigation of seabed properties using a passive remote sensing method and instrumentation system known as the bottom shear modulus profiler (henceforth BSMP). The BSMP measures small seabed accelerations created by variations in hydrodynamic pressure caused by passing surface gravity waves. Spectral analysis and geophysical inverse methods are then applied to the data yielding the sediment shear modulus with depth profile. Knowing shear modulus, other seabed properties may be calculated including bulk density, porosity, and shear and compressional wave speeds.²⁴ The BSMP instrumentation and methods have been tested extensively. Over 1500 hours of data have been taken at several sites offshore of New Jersey, George's Bank, South Florida, and North Carolina. Of particular interest to this investigation is the New Jersey Atlantic Margin Coring project site experiment conducted in 1987. At this site, in the vicinity of Atlantic margin coring project (AMCOR) borehole 6010, a shallow water acoustic propagation study was performed by Carey.²⁵ This study, because it is in an area where sediment properties have been determined previously, provides a unique opportunity to incorporate the BSMP database with an investigation of continuous wave acoustic propagation. In shallow water the role of the sediment is of primary importance when attempting to describe acoustic wave propagation. The case presented is bottom-limited, meaning that the sound velocity is less at the bottom than the velocity at either the source or receiver depths. All propagation beyond range of a kilometer strongly interacts with the bottom. Hence, in this bottom-limited condition, the acoustic properties of the sediment dominate the propagation and are an essential ingredient of propagation modeling. Often an accurate description of the sediment in a given area is not available to aid in the description of shallow water acoustic propagation and many assumptions must be made about sediment properties.

In this paper we make efforts to describe the Hudson Canyon acoustic transmission results using BSMP sediment values. The environmental model, once developed successfully, is used as a tool for determining the following: (1) the acceptability of BSMP sediment values as representation of the actual seabed properties; (2) the effect of shear and compressional speeds in the sediment upon the normal modes and on the transmission loss with range and depth; (3) the existence and effect of a secondary waveguide within the sediment layers; (4) the effect of surface and volume scattering upon transmission loss; (5) the fre-

quency dependence of intrinsic attenuation in the sediment. To obtain an accurate representation, three established computer codes were used as the basis for this study: the seismo-acoustic fast-field algorithm for range-independent environments (SAFARI), the parabolic equation (PE) approximation, and the SACLANTCEN normal-mode acoustic propagation code (SNAP). The seismo-acoustic fast-field algorithm for range-independent environments, SAFARI, uses a fast-field approach to solve the acoustic wave equation yielding in principle an exact solution for range-independent cases.¹⁹ This program performs a single frequency calculation of the total wave field at any number of depths and ranges for either a single compressional source or a vertical phased source array. For this application a single compressional source was used with various receiver configurations. Transmission loss versus range, Hankel transform integrands, and range/depth contour plots of transmission loss were obtained for comparison with data. The parabolic equation code, PE, solves the acoustic wave equation problem directly. Used here is the PE code based on the split-step Fourier algorithm.²⁰ This PE code was chosen because of the ability to efficiently handle range dependent environments. The SACLANTCEN normal-mode acoustic propagation code, SNAP,²¹ was used here for its ability to provide the normal modes of propagation. This code also calculates transmission loss.

These three codes allowed determination of the acceptability of results from our representation of the acoustic environment. Since each provided the transmission loss as a function of range, calculated levels of loss were compared with experimentally measured levels, as well as the horizontal wave-number spectrum. Calculations performed with each of the three codes and a variation of environmental input parameters provided a means of determining the key environmental parameters governing the acoustic propagation.

I. EXPERIMENTAL RESULTS

A. BSMP methods

The seismo-acoustic environments encountered in the ocean are very complex in shallow water areas. In addition to spatial variability the properties of the water column are time dependent and can change over the period of a day. These changes are due to any one or combination of tide changes, current flows, internal waves, eddys, and diurnal temperature variations all of which lead to salinity and density changes. Since seismo-acoustic propagation is highly dependent on the material properties of the environment an exact computer model would require knowledge of all these properties to a fraction of a wavelength. Such information is not realistically available therefore some error is inherent. In acoustic studies made over tracks with durations of less than a few hours the problems of environmentally time-dependent changes are not pronounced. Standard traditional methods for obtaining environmental information are sonar depth soundings, CTD, and SVP measurements along the acoustic track. The sediment

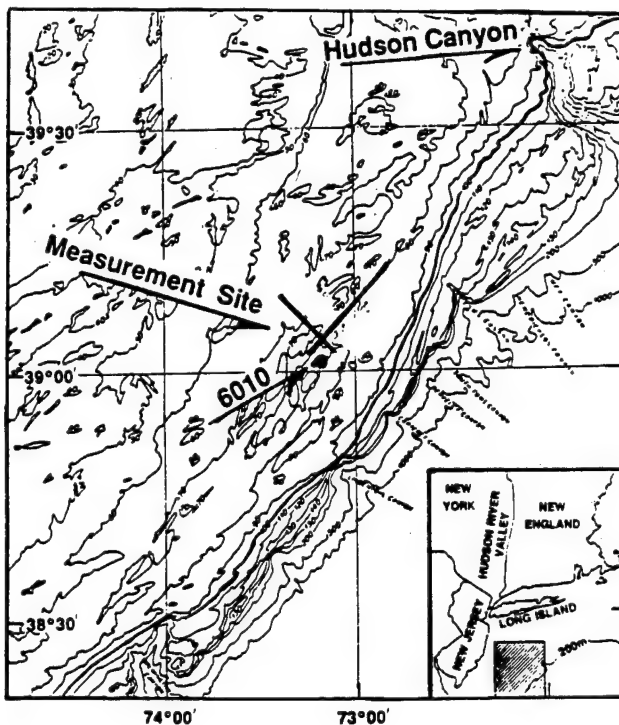


FIG. 1. Map of the New Jersey continental shelf. Marked is the location of the AMCOR borehole site 6010.

properties for most areas are unknown beyond the uppermost layer. Short cores or grab samples have been the standard methods for finding the properties but do not yield information below a meter or so and the sediment is usually disturbed when it is evaluated. As a result assumptions are made about the shear speed, compressional speed, and attenuation profiles which as a result can lead to anomalous results. The deep layer effects are especially important at low frequencies. Methods for determining these profiles accurately must be developed for nonspeculative environmental modeling.

A relatively new system for measurement of sediment properties has been developed by the Geoacoustics laboratory at the University of Miami named the bottom shear modulus profiler (BSMP). BSMP makes realtime measurements of small amplitude low-frequency (0.001–1.0 Hz) seabed motions created by passage of surface gravity waves and seabed microseisms. Vertical accelerations and pressure data are processed using spectral analysis techniques and geophysical inverse methods.²⁵ The system utilizes both an instrumentation system and inversion technique developed by Yamamoto and co-workers.^{25,26} The advantage of the BSMP over other methods is that it uniquely determines the low velocity layers within the seabed without disturbing the sediment environment. Comparisons of BSMP results with results from other measurement techniques have been made giving excellent results.^{27,28} The deployment methods and complete descriptions of the theory behind the methods of data collection and analysis have been well documented.²⁴

The experiments of interest to this paper were con-

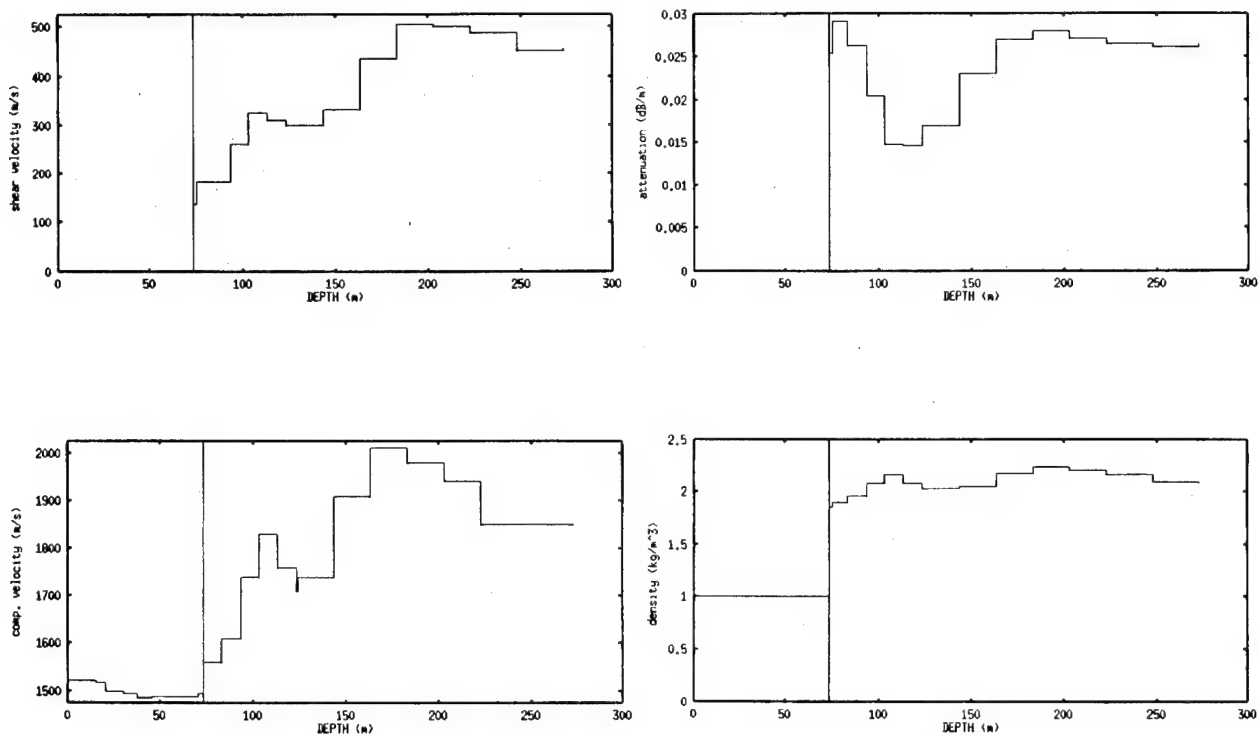


FIG. 2. Depth profiles of AMCOR 6010 environment determined from CTD and SVP measurements and BSMP, compressional and shear speeds, density, and Biot, Yamamoto, Turgut attenuation.

ducted in 1987 with an array of seismic sensors near the AMCOR site 6010, the location of Carey's cw acoustic propagation experiment (Fig. 1). The AMCOR 6010 site lies in 73 m of water. The area consists of mainly sands and silty clays. The wavelengths of the surface gravity waves enabled penetration at the AMCOR 6010 site to a depth of 200 m, which is more than enough information for the frequencies considered here where acoustic penetration even at the lowest frequencies was only ~ 100 m, although all the data were used for completeness. Resolution of the BSMP system is governed by the wavelengths of the surface gravity waves. The vertical resolution is nominally 1/5 the water depth. At this AMCOR site, comparison of BSMP results with borehole compressional logs show agreement $\pm 10\%$ to 120 m. The penetration of the inversion is 1/2 the longest wavelength propagating at the surface. The depth profiles to be used here were calculated by Trevor and Yamamoto.²⁴

The depth profiles of compressional wave velocity, shear wave velocity and density determined by BSMP for the AMCOR 6010 site are in Fig. 2(a)–(c), respectfully. The attenuation profile [Fig. 2(d)] was estimated using Biot theory and the shear modulus and density values determined by BSMP. Note the slow velocity section between ~ 25 m and ~ 100 m within the sediment. It will be shown that this section behaves as a waveguide.

B. Acoustic data

Carey²⁹ set up the continuous wave acoustic experiment to take place at AMCOR 6010 because of the known

geophysical conditions. The area has been surveyed by several groups including the University of Miami, Woods Hole Oceanographic Institute, and the AMCOR and COST drilling operations.

The low-frequency (50–600 Hz) experiment took place in shallow water (73 m) during a period of calm sea state, less than Beaufort 2. A calibrated acoustic source was towed at roughly 36 m along the 73-m isobath radially to distances of 4 and 26 km. A changing depth case (73–58 m) was also measured for all frequencies. Ship speed was determined by constant engine speed operation. This resulted in speeds between 2 and 4 kn. A buoy-mounted acoustic transponder and loran C were used as navigation devices. The fixed position vertical hydrophone array consisted of 24 phones spaced 2.5 m apart extending from hydrophone 24 placed on the seafloor to hydrophone 1 at approximately 13-m depth. CTD and SVP measurements were made at regular intervals during the course of the various legs of the experiment. Data collection was made under conditions that can be considered as controlled as is possible in the ocean environment.^{29–31}

Synthetic aperture processing methods were used to produce measures horizontal wave-number spectra. Doppler shift was accounted for in the data processing and calibrated transmission loss as a function of range was obtained. A total of eight frequencies were used; 75, 275, 525, and 600 Hz on the outgoing leg from the receiving array and 50, 175, 375, and 425 Hz when inbound.

II. RESULTS AND DISCUSSION

A. Establishing an accurate model

To establish an accurate description of the acoustic data SAFARI is input the environmental parameters measured during the acoustic experiment and BSMP sediment values. This accurate model has excellent agreement with the data eigenvalues as well as a good match of transmission loss over range in both trend and mode interference length. The horizontal wave-number spectra are determined by the zeroth-order Hankel transform pair, which moves us back and forth between the range domain (pressure field) and the horizontal wave-number domain (depth-dependent Green's function) as applied to the measured pressure field. Suppressing the harmonic time dependence $e^{-i\omega t}$

$$p(r) = \int_0^\infty g(k_r) J_0(k_r r) k_r dk_r, \quad (2)$$

$$g(k_r) = \int_0^\infty p(r) J_0(k_r r) r dr. \quad (3)$$

Utilizing the efficiency of the FFT algorithm, Eq. (3) is evaluated via an asymptotic expansion of the zeroth-order Bessel function

$$g(k_r) = \left(\frac{2}{\pi k_r}\right)^{1/2} \int_0^\infty \sqrt{r} p(r) \cos\left(r k_r - \frac{\pi}{4}\right) dr, \quad (4)$$

$$J_0(x) \simeq \left(\frac{2}{\pi x}\right)^{1/2} \cos\left(x - \frac{\pi}{4}\right); \quad x \gg 1. \quad (5)$$

The normal modes of the waveguide show up as strong resonance peaks when the $p(r)$ data are transformed. The modal eigenvalues are then picked off at the peak locations of $|g(k_r)|$ and compared to data.^{32,33} The depth-dependent Green's functions also provide direct measurement of the

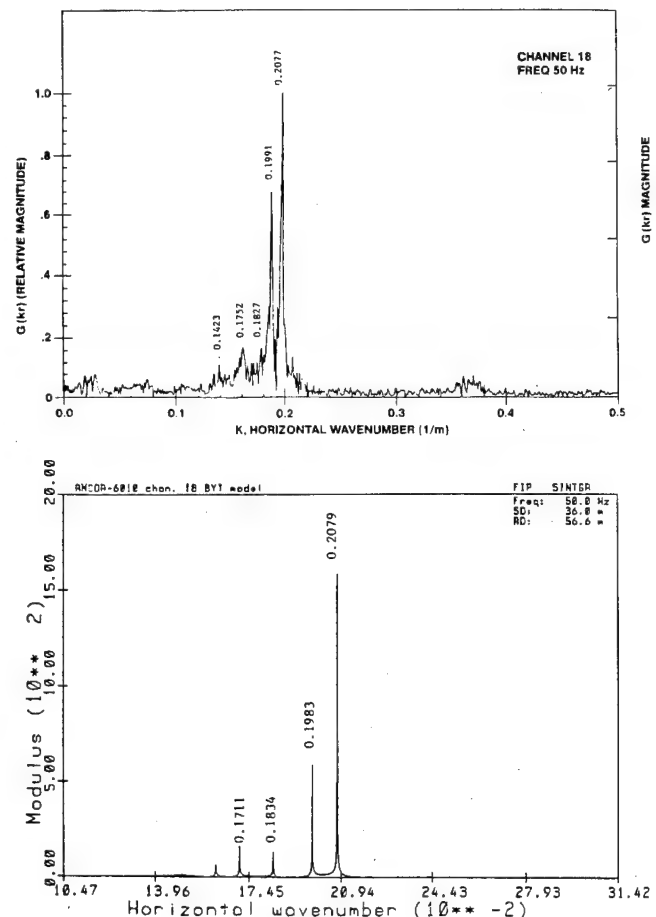


FIG. 3. Horizontal wave-number spectrums calculated for (a) the 50 Hz NUSC data channel 18 and (b) SAFARI model representation of channel 18 50-Hz propagation: note—abscissa scales are not the same.

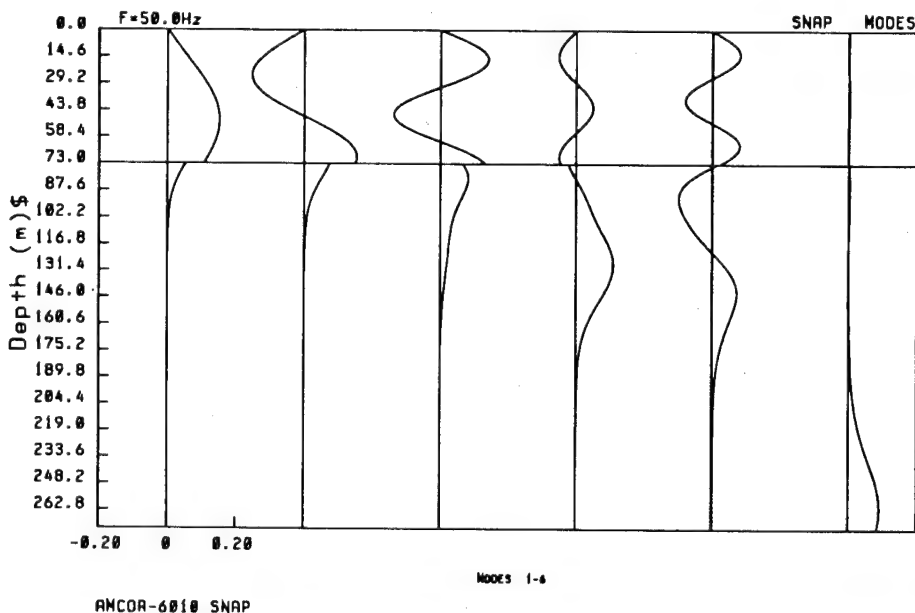


FIG. 4. SNAP model calculations for 50-Hz eigenfunctions propagating through AMCOR 6010 environment modeled with BSMP sediment values.

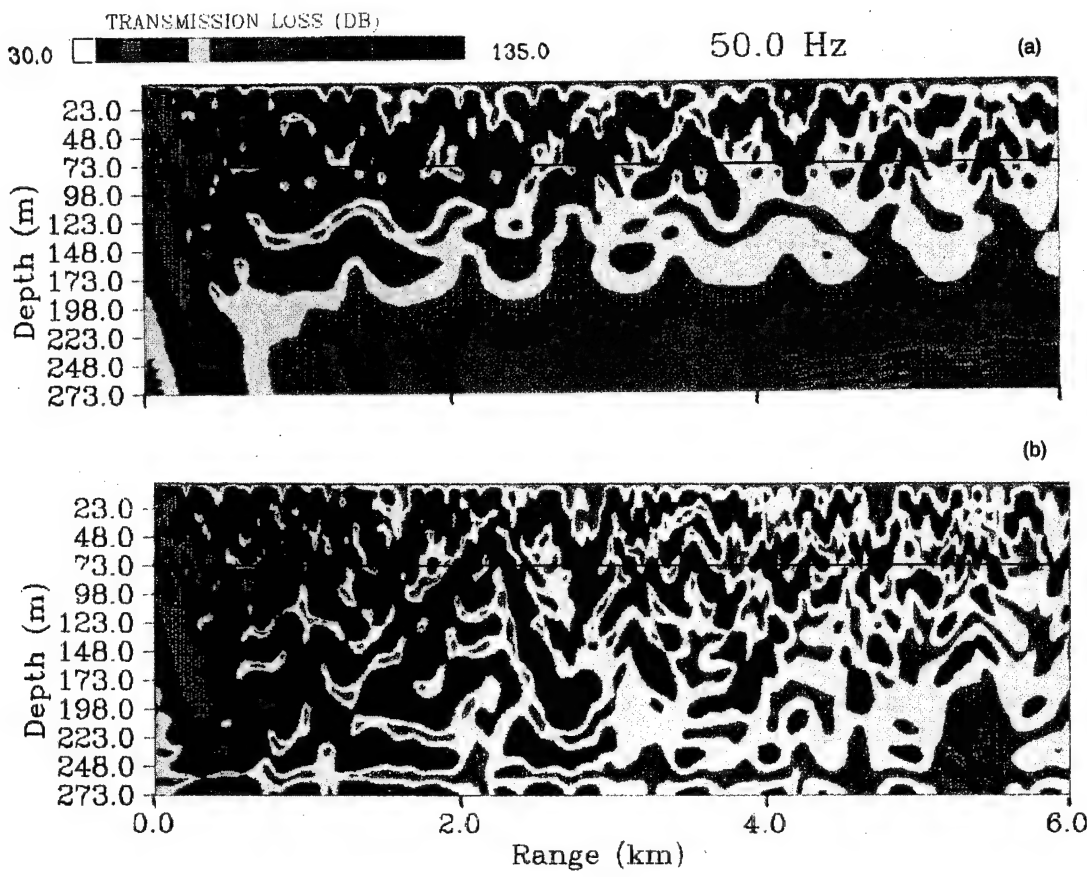


FIG. 5. Field plots at 50 Hz of transmission loss over depth and range calculated by SAFARI: (a) with shear wave included (b) no shear, i.e., fluid model.

amplitudes of the modal peaks. This will give some comparison of relative intensities of the modes. This is important for determination of attenuation loss because intensity change is a direct measure of loss.

The results obtained from BSMP were input into SAFARI along with a water column sound-speed profile and bathymetric information taken during the cw experiment. The initial model consisted of these input along with an assumed depth constant attenuation profile, no layer interface roughness or sea surface roughness was assumed. Carey's experiment took place in a sea state less than Beaufort scale level two so this is reasonable. Transmission loss versus range and wave-number spectral plots were calculated at 50 Hz. These results were compared to measurements and very favorable agreement between the data and the model was obtained. The most notable factor is that the horizontal wave numbers agreed to the third decimal place (Fig. 3). The experimental error has been estimated to be ± 0.003 and is verified by Cederberg.³⁴ These results would indicate that the BSMP input values are quite accurate and an acceptable input parameter for acoustic modeling.

Having established an accurate representation of the data using the model, the model may then be used as a tool for examining the effects of varying input parameters upon the acoustic propagation. The effect of the shear and compressional velocity profiles may be examined, changing

their properties and seeing the effect on the output. The shear speed profile can be entirely removed creating a fluid space, to examine the effect of shear upon the acoustic signal propagation, if any. It is unrealistic to remove totally the shear but for the purposes of examining the relative effect the total removal from the model is appropriate. The compressional velocity profile is the dominant factor governing acoustic propagation. Changes in the compressional speed profile will affect modal propagation significantly. Examination of the transmission loss curves computed by the model with those measured in the field can yield, through interpretation, information about the modal interference and the effect of scatterers and reflectors upon the mode propagation.

B. The effect of the shear velocity profile

To determine the effect of the sediment shear speed on acoustic propagation we used SAFARI rather than PE because it includes the tangential or shear stress while PE does not. SAFARI was run using all the environmental parameters described previously to determine transmission loss. Three different frequencies 50, 375, and 600 Hz were used for this study. SAFARI calculations with both an elastic shear supporting bottom and also a fluid bottom we could test the shear effect upon modal propagation.³⁵

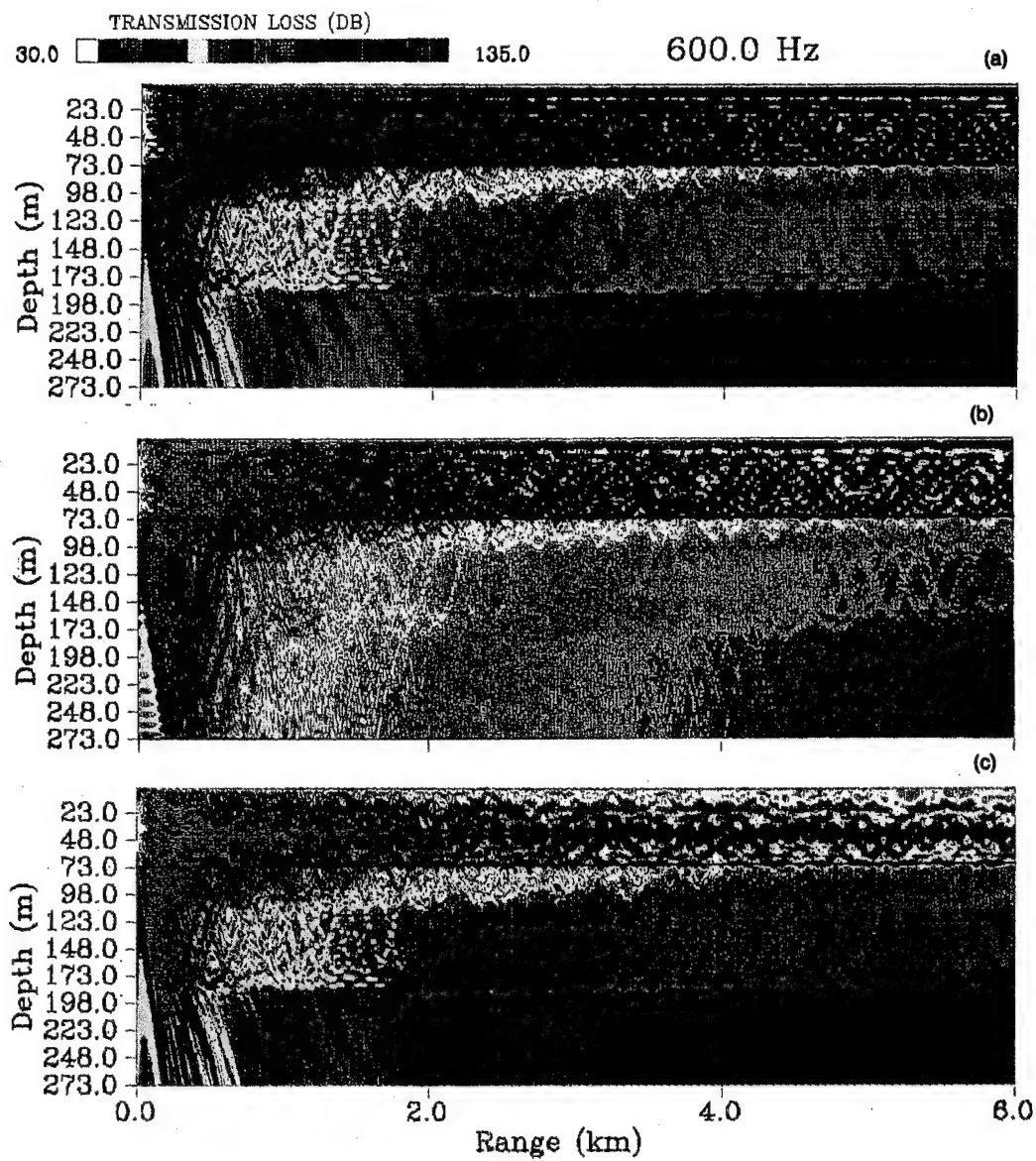


FIG. 6. Transmission loss as a function of depth and range at 600 Hz: (a) no scattering in model, shear included; (b) no scattering in model, no shear; (c) scattering modeled by attenuating layer at the water-sediment interface, shear included.

The shear loss itself did not affect which wave numbers propagated at these frequencies. It is important to note that one may treat the sediment bottom as fluid so long as energy dissipation due to shear conversion can be properly accounted for. This will simplify the computational effort tremendously. Removing the shear effects from the model, thus creating a completely fluid space, changed only the coherent transmission loss structure and thus the relative amplitudes of the modes. These effects occur in differing ways at different frequencies. It can be seen by inspection of the spectral structures that as the carrier frequency is increased the relative change in amplitude when shear is removed intensifies the higher-order modes more than lower-order modes. Thus they propagate stronger than when shear is included relative to the lower-order modes. To investigate this phenomenon the eigenfunctions were plotted using SNAP for several of the modes (Fig. 4).

It is seen that the higher-order modes penetrate much further in the sediment. The effect of removal of shear is that more energy is transmitted in those modes that penetrate the seafloor further. Removing the shear in the model takes away a loss mechanism in the sediment. Therefore when energy is introduced to the sediment it is not dissipated as readily and higher-order modes carry more energy to the receiver while the lower-order modes, which propagate almost exclusively within the water column, not being affected by changes in shear, relinquish some of their energy to the higher modes. This results in smearing of the spectrum across the discrete wave-number space. The effect is quite striking when only five or six modes are present such as in the low to mid frequencies. Figure 5 shows transmission loss at 50 Hz for cases with and without shear in the model. When the frequencies increase, the effect upon the modal spectrum becomes smeared (spread

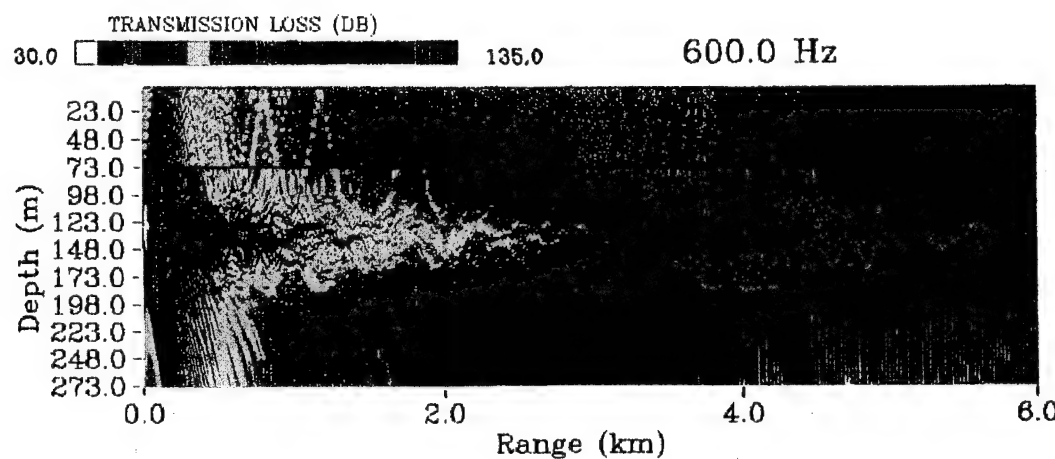
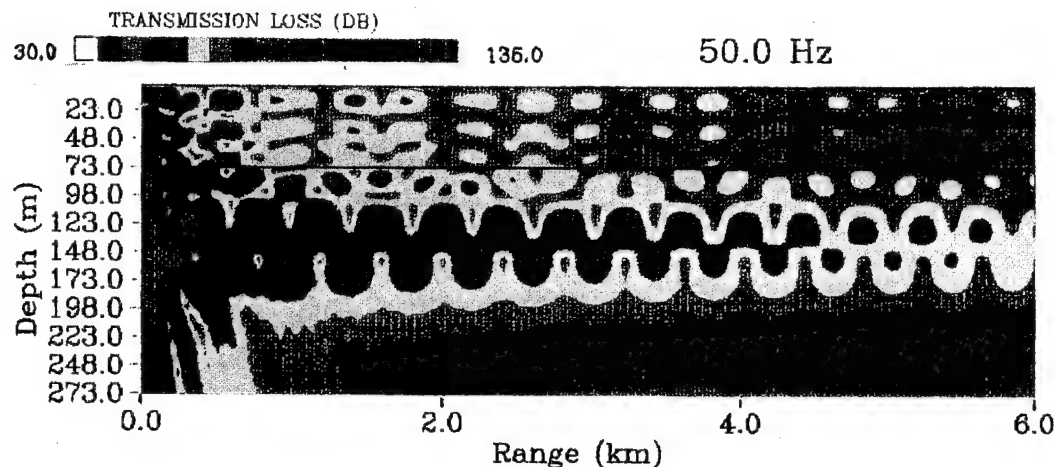


FIG. 7. Transmission loss as a function of range for 50- and 600-Hz propagations with source imbedded 52 m in sediment layers.

across the various modes) because of the large number of modes present. A good illustration of the change made in the high-frequency transmission loss field is in Fig. 6. It may be observed that as tangential stresses are removed the losses are significantly reduced throughout the frequency range considered (50–600 Hz).³⁶

C. The compressional speed profile effect on the acoustic wave field

The compressional speed profile has a large role in determining the acoustic normal modes which propagate. Any alteration made in the compressional speed profile, especially in the near surface gradient, will shift the horizontal wave numbers considerably. The fact that the calculated wave-number spectra compare so well with those measured indicates an acceptable representation of the compressional wave speed profile in the sub-seafloor layers and water column.

In this shallow water channel the most obvious acoustic waveguide is the water column itself. Reflections at the

free surface and seafloor provide a strong sound channel through which most of the acoustic energy propagates when a source is present in water. This is evident in Figs. 5(a) and 6(a) where sound transmission in the water column experiences a small loss compared to transmission in the sediment layers.

For the AMCOR 6010 site the BSMP profiles of density and sound speeds show an area from approximately 25 to 100 m within the seabed of reduced density and sound speed; a broad minimum that could act as a “potential well” (Fig. 2).³⁷ The significance of this phenomenon is that any sound entering this area will have a strong tendency to be trapped and propagate in this sub-seafloor channel. Figure 5(a) shows this sub-seafloor waveguide propagation.

To illustrate the effect of the minimum the source was moved to a level 52 m into the sediment and SAFARI was used to calculate the refractive effects of the sub-sediment waveguide. Figure 7 shows the calculated transmission loss field plots at 50 and 600 Hz for this configuration. These

show very strong propagation within this channel. Very little sound leaks into the other layers especially below 105 m in the seabed where there is a steeply increasing compressional wave speed gradient with depth (hard layer).

In the case of Carey's data set we see that by calculating the eigenfunctions with SNAP at 50 Hz, modes 3 and higher, $k_h=0.1821, 0.1765$, and 0.1679 , respectfully, interact with this sub-seafloor region (Fig. 4). Mode 4 in particular has a broad intensity maxima in this region. Figure 3 shows the measured horizontal wave-number spectrum with the fourth mode somewhat stronger than modes 3 or 5 at the receiver. Because of the favorable propagation in the sub-seafloor waveguide this mode has higher intensity than 3 or 5 at the receiver depth 56.6 m. Modes 1 and 2, $k_h=0.2077$ and 0.1984 , respectfully, naturally have the greater intensities because they are restricted largely to the water column where the losses are much less than in the sediment layers. However modes 3 and 5 experience less favorable propagation conditions and are attenuated.

This feature could be considered unique to the AMCOR 6010 site however it is interesting to the extent that it gives some useful physical reason for relative modal propagation seen in the measured transmission loss. Other shallow water areas may have different unique structures that may affect acoustic propagation. Thus, in shallow water acoustic propagation studies, detailed sub-seafloor profiling must be incorporated into calculations since these sub-seafloor features have strong effects upon the transmission. As the frequency is increased the depth of penetration in the sediment is less but interaction and attenuation are larger because of the smaller acoustic cross section with respect to the layering and roughness. Therefore the higher the frequency the more detailed information is needed near the water sediment interface. This detailed model of the seafloor must be a range-dependent one. The BSMP profile used here is a range-independent profile and the idea that the sub-sediment waveguide continues with range is only speculation although the measured sound transmission data are consistent with this speculation.

D. Intrinsic attenuation of acoustic waves by the sediment

The propagating modes for a given source frequency each interact differently with the environment and consequently interfere more strongly in some areas than in others (Fig. 8). The higher-order modes correspond to steeper ray grazing angles. Thus when the sound-speed profile increases with depth, as is the usual case, the higher-order modes penetrate deeper in the sediment, while the lower-order modes experience near total reflection at the water-sediment interface. Because each mode has a different amplitude variation with depth, in regions of high modal intensity the variation is sinusoidal and the number of peaks and notches (nodes and antinodes) increases with the number of propagating modes. Each mode experiences a unique attenuation corresponding to its depth distribution of intensity. When we place a hydrophone in the water column at some depth and tow a source radially from the hydrophone the received signal will exhibit a variation of

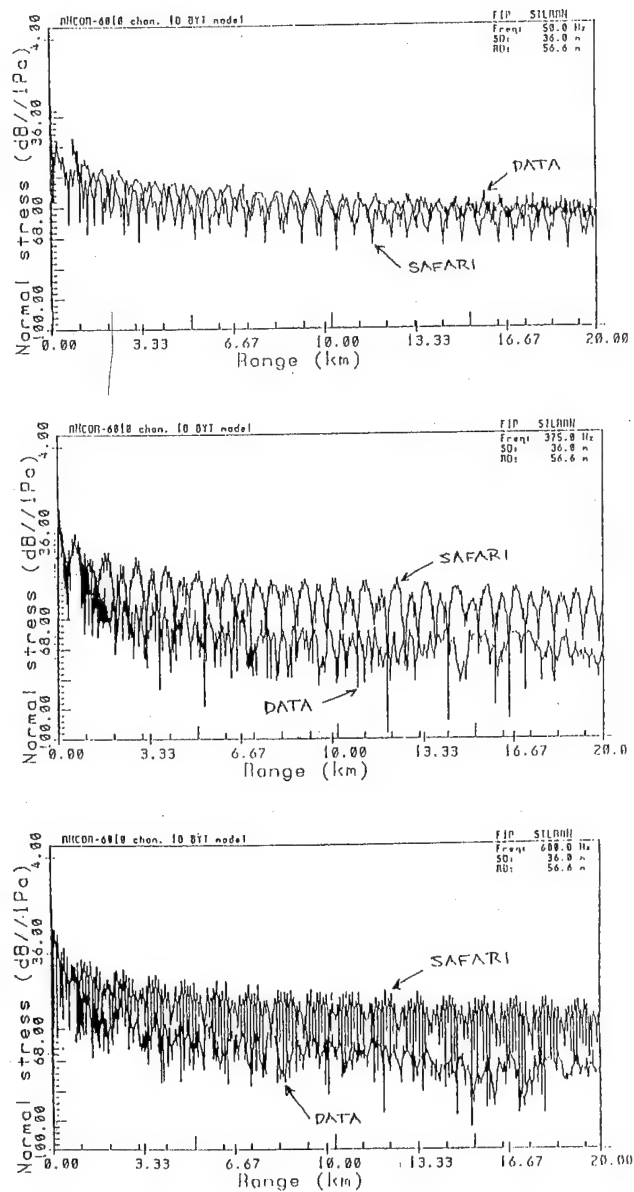


FIG. 8. Transmission loss over range 50, 375, and 600 Hz.

high and low amplitude due to the mode interference pattern. This interference governs the transmission loss pattern (*mode interference wavelength*) and the "frequency" of the occurrences of constructive interference increases with the number of modes.²² The shift in the computed results compared to the measured transmission loss with range is due to some change in the actual interference pattern. Since we observe the same number of propagating modes in both the transmission loss data and the computed interference pattern, the actual propagation must be perturbed by some effect not included in the calculation. Such an effect is most likely range-dependent scattering within the sediment, sub water-sediment interface reflector/refractors, and/or water column fluctuations, all spatial variations in the compressional speed profile. The modal interference comparison shows relatively good agreement

at short range and as range is increased the pattern becomes increasingly shifted from the data indicating a range-dependent effect.

The reflectors/refractors that make up the acoustic waveguide govern where these peaks and notches occur in the transmission loss field. The BSMP sediment profile and the SAFARI code are range independent thus any variations in range in the model are approximations of the actual loss mechanism estimated from the initial conditions supplied to the model. Although SAFARI is sufficient for many fields, in areas of strong sediment structure (relief of layers), range-dependent information is needed as SAFARI fails. The area at AMCOR 6010, as evidenced by the Woods Hole HUNTEC survey, has many hard sub-seafloor layers where old riverbeds were, these, as well as other strong deeper reflectors, span the acoustic track. This survey illustrates the variability of the area with range.³⁸ The 50-Hz case was input to the PE model with range-dependent bathymetry. Range-dependent sediment properties were not available so the BSMP values at AMCOR 6010 were extended in range as was the water column data. The PE calculations with homogeneous sediment layers but varying bathymetry yield a better result but more accurate range-dependent environmental information would be welcome.

At the lower frequencies excellent agreement was found between transmission loss trends (Fig. 8). As the frequency is increased the calculated transmission loss is less than the measured results. The differences increase with range, in other words, the real signal experiences a stronger loss as a function of range than does the computed representation of the acoustic wave. Most probably this is due to effects of interface scattering and volume scattering not considered in the calculation. The individual scatterers of this type are small compared to the acoustic wavelength, Rayleigh scatterers. BSMP resolution limits are greater than the acoustic wavelength or acoustic penetration depth giving rise to an underresolved sediment at high frequencies. Scattering of this kind accumulates with range and increases with frequency.³⁹

Any effect of bathymetry, currents, biologicals, or sub-sediment changes, etc. will affect the transmission of the signal. There is some variation in bathymetry over range, which in the "flat bottom" case is minor. More significant are the strong sub-seafloor reflectors shown by the Woods Hole 3-D HUNTEC survey. BSMP range-independent results show a strong reflector (compressional speed gradient) approximately 110 m below the sea floor as well as one 25 m beneath the sea floor (Fig. 2). The HUNTEC survey also shows the reflector ~25 m beneath the sea floor. These two independent surveys agree that reflectors do exist sub-seafloor and the HUNTEC survey establishes that the structure of these reflectors varies with range and depth. The HUNTEC survey does not yield any information on the actual sediment properties quantitatively as BSMP does but it does give a qualitative look at the structure. The AMCOR 6010 site lies in the Hudson Canyon region where the Hudson River has deposited sediments dating to at least Pleistocene. The area has quaternary sed-

iments overlying a strong reflecting layer and sub-seafloor "channels" producing a rough topography, the result of melting of the ice sheet and the transport of sediment during sea level regression, still stand and transgression. The models of transmission loss do not show any changes in the gradient position with range or depth therefore they contain less loss over range while the transmission loss from actual measured data displays a greater loss with range due to these scatterers. The ratio of the characteristic roughness scale size to acoustic wavelength increases resulting in an increase in scattering cross section and consequently higher attenuation.

Attenuation is an integral component of any transmission model. Attenuation may be due to scattering at rough surfaces, thermoelastic effects, bathymetric variations, volume scattering or absorption, frictional losses or shear wave conversion, and attenuation, but in practice it is that decrease in the signal's intensity in excess of that due to geometrical spreading. For long ranges we may assume that the effect is principally to produce for each mode a decrease in wave amplitude with range of $e^{-\delta_m R}$ over and above the cylindrical spreading $R^{-1/2}$.

Attenuation of the acoustic wave field in the bottom is determined by both the intrinsic sediment attenuation and the attenuation due to scattering losses. The intrinsic sediment attenuation is determined by a combination of two methods, the method of relative mode intensity and by using Biot theory for determination of the sediment attenuation profiles.⁴⁰

The method of relative mode intensities uses the horizontal wave-number spectrum and compares the relative intensities of the modes that propagate at a particular hydrophone depth. To establish a datum the mode with greatest intensity in the measured horizontal wave-number spectrum is set to one and the others normalized by that level. The disadvantage to this method is that establishing depth dependence is difficult unless we know how to separate the mode intensities with depth and weight each level accordingly so that a new depth separated attenuation profile may be established. This can be an exceedingly difficult task if the frequency is high and the spectrum contains many modes. Even for just a few modes it is not trivial.

Biot theory models the pore structure of sediments as either capillary tubes of equal diameter or as parallel walls of constant spacing. In nature the pore structure of sediments is not as simple as these approximations. Yamamoto and Turgut extend the theory of Biot by deriving the mathematical expressions for intrinsic permeability and the viscous correction factor for arbitrary pore size distribution.¹⁸ The complex phase velocities are found to be

$$V_n = V_{rn} + iV_{in} \quad (n=1, 2, \text{ and } 3) \quad (6)$$

and the specific attenuation is

$$Q_n^{-1} = 2V_{in}/V_{rn} \quad (n=1, 2, \text{ and } 3). \quad (7)$$

The subscripts $n=1,2,3$ refer to the fast compressional, slow compressional and shear velocities, respectively. Compressional wave attenuation has the greatest effect on individual mode intensities while shear wave attenuation af-

fects only the total attenuation of the propagation. To convert Q_n^{-1} to units of dB/m and give a frequency relationship we use

$$\alpha_n \left(\frac{\text{dB}}{\text{m}} \right) = 8.686 \pi \left(\frac{Q_n^{-1}}{V_{rn}} \right) f \quad (n=1, 2, \text{ and } 3). \quad (8)$$

This value α_n is the intrinsic attenuation produced as a function of depth for the frequency considered.

Once a depth-dependent intrinsic attenuation profile is developed it is helpful to get a value for a depth-averaged equivalent attenuation so that comparison may be made between these attenuation profiles and other data sets. To do this we determine the depth-averaged attenuation for each individual mode by weighting the sediment attenuation by the modal amplitude at depth. The horizontal wave number is decomposed to its real and imaginary parts

$$k_n = \kappa_n + i\delta_n, \quad (9)$$

where δ_n is the mode attenuation. A perturbation solution may be found for δ_n ,

$$\delta_n = \frac{\omega}{\kappa_n} \sum_{m=1}^M \rho_m \int_{z_{m-1}}^{z_m} \frac{\alpha(z)}{c(z)} |\psi_n(z)|^2 \frac{dz}{A_n}, \quad (10)$$

where

$$A_n = \sum_{m=1}^M \rho_m \int_{z_{m-1}}^{z_m} |\psi_n(z)|^2 dz \quad (11)$$

normalizes above and M is the number of layers. This may be reduced to an expression for intrinsic sediment attenuation by

$$\alpha(f) = \delta_n(f) / \gamma_n, \quad (12)$$

where

$$\gamma_n = \frac{\omega \rho_{\text{sed}}}{\kappa_n} \int_{\text{sed}} \frac{|\psi_n(z)|^2 dz}{c(z) A_n} \quad (13)$$

(Mitchell and Focke¹⁴). This procedure was performed on depth-dependent intrinsic attenuation profiles predicted by Biot theory. The advantage to these depth-averaged intrinsic sediment attenuations is the ability to examine the frequency dependence of the intrinsic mode attenuations and compare with work by others.

The depth-dependent intrinsic attenuation profiles for seven frequencies were calculated using BSMP sediment values. An example of an attenuation profile is given in Fig. 2. SAFARI calculations using these values compared with transmission loss measurements show excellent agreement in horizontal wave-number spectrum. Table I shows the relation of mode intensities in available data compared to SAFARI calculations employing attenuations calculated using extended Biot theory and the method of relative intensity of the modes.

Figure 9 is a compilation of data on attenuation versus frequency in unlithified marine sediments taken from work by Hamilton.¹⁵ The line labeled f^1 indicates the slope of the line with a first power frequency dependence. It can be seen that for most of the data to date attenuation follows approximately a first power frequency dependence espe-

TABLE I. Relative mode energies at 50 Hz, data and model.

Frequency (Hz)	Mode	Data	Rel. Md. model	BYT model
50	1	1.0	1.0	1.0
	2	0.673	0.375	0.429
	3	0.163	0.094	0.178
	4	0.166	0.125	0.178
	5	0.115	0.047	0.053
75	1	1.0	1.0	1.0
	2	0.599	0.447	0.696
	3	0.305	0.284	0.214
	4	0.554	0.391	0.589
	5	0.034	0.019	0.085
175	1	1.0
	2	0.435
	3	0.013
	4	0.174
	5	0.130
275	1	1.0
	2	0.208
	3	0.104
	4	0.083
	5	0.563
375	1	0.914
	2	0.420
	3	1.0
	4	0.160
	5	0.222
525	1	0.365
	2	0.277
	3	1.0
	4	0.378
	5	0.250
600	1	0.731
	2	0.086
	3	0.290
	4	1.0
	5	0.140

cially at frequencies higher than 1 kHz. At frequencies less than 1 kHz little data have been available for study and frequency dependence is still in question. To determine the intrinsic attenuation it is necessary to distinguish between sediment types. The predictions for sand by Stoll surely do not follow the first power of frequency. The variation with frequency by Stoll for silt is closer to a first power frequency dependence. The AMCOR 6010 site consists mostly of silty sand and silty clay overlying sand and sandy clay layers. The environment has many layers each contributing their own attenuation factor. The depth-averaged intrinsic attenuation for the first mode at each frequency was found as well as that mode which first penetrates to 100 m in the seafloor (Table II). It can be seen clearly that the attenuation results lie in a region well below the values found by Hamilton for frequencies between 50 and 600 Hz based on an extrapolation of the higher frequency findings and a linear first power frequency dependence. The reflection data from the water-sediment interface measured by Mitchell and Focke¹⁴ yield attenuation in deep ocean sediments in the 20- to 400-Hz range. These attenuation val-

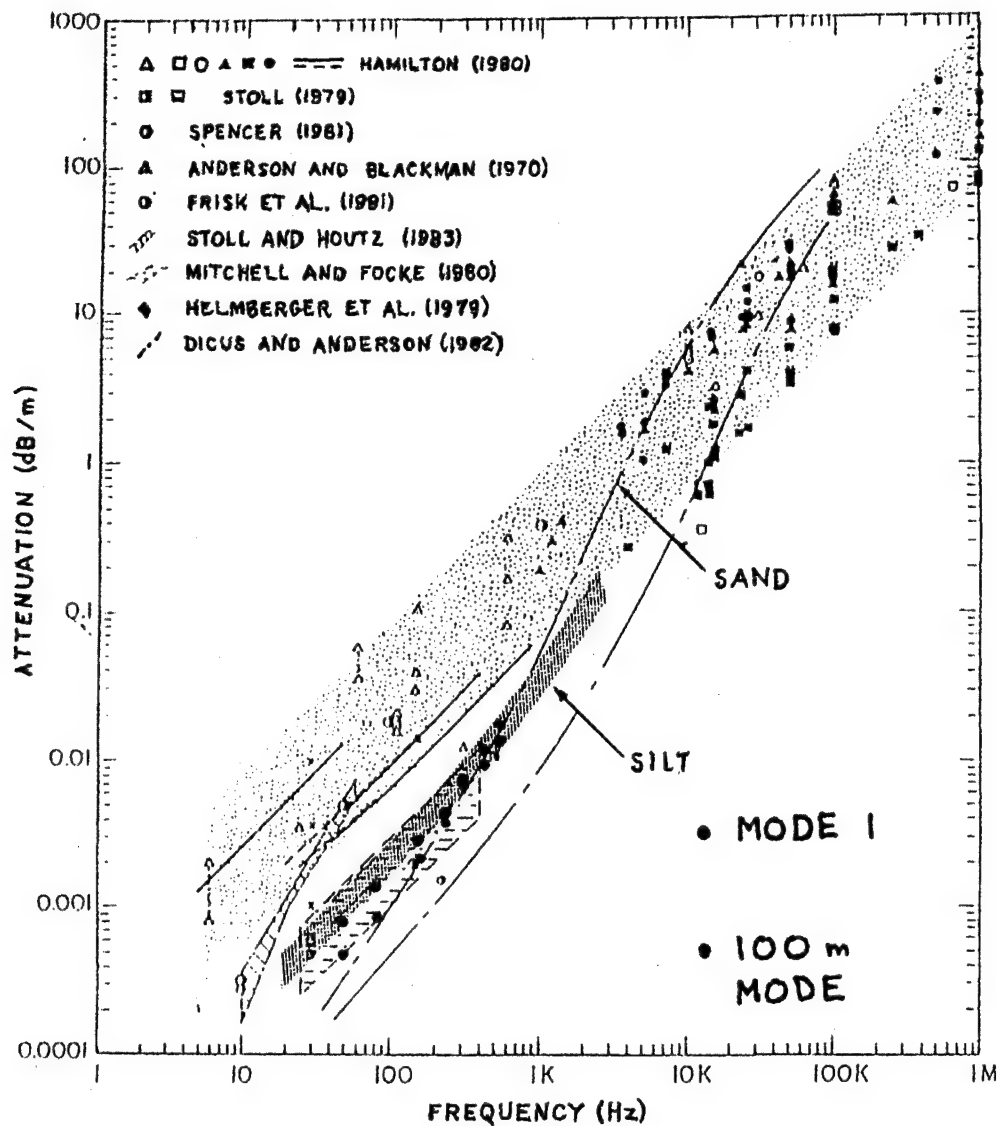


FIG. 9. Compilation of existing attenuation data with our result inlaid.

ues and our values for 50 to 600 Hz determined from *in situ* experimental measurements of silty sand and silty clay sediments and numerical models agree quite well.

The slope of the intrinsic sediment attenuation data compared to one another and other data was determined using the endpoints at 50 and 600 Hz. The resulting fit to data points for the first mode is

$$\alpha_{50,600} = 1.393(10^{-5})f^{1.008}(\text{dB/m}). \quad (14)$$

The resulting fit to the point for the first mode that penetrates to a depth of 100 m yields

$$\alpha_{50,600} = 6.336(10^{-6})f^{1.144}(\text{dB/m}). \quad (15)$$

These results agree with a first power dependence over this small region 50 to 600 Hz although our *in situ* attenuation levels are much lower than previously determined (Fig. 9).

Modes that have intensity maxima in the water column are affected by sediment attenuation less than modes having intensity maxima within the sediment. In Fig. 4

modes 1 and 2 constitute very intense propagation within the water column. On the other hand, modes 4 and 5 propagate more intensely within the sediment layers. Attenuation due to volume inhomogeneities or scattering layers near the intensity maxima cause the higher order, lower wave-number modes to be attenuated more rapidly. As frequency is increased more modes propagate to the receiver due to the increasing number of modes with intensity maxima within the water column. The interaction of these modes is in the first few meters of sediment on a scale much finer than that of low-frequency propagation. In shallow water these upper layers are mixed up, quaternary sediments containing structure the result of recent gravity wave interaction, biological activity, and littoral drift. Low-frequency sound has wavelengths long enough so as it is not affected by these upper layers as strongly because of a much lower scattering cross section.^{41,42} The result is a high intrinsic attenuation environment for high-frequency sound and thus attenuation increases with frequency.

TABLE II. Intrinsic attenuation values for the first two modes and 100-m mode.

Frequency (Hz)	Mode	k_h	α Attenuation (dB/m)
50	1	0.2079	7.175E-04
	2	0.1984	7.176E-04
	100 m	0.1765	5.57E-04
75	1	0.3141	1.09E-03
	2	0.3061	1.10E-03
	100 m	0.2650	7.53E-04
175	1	0.7637	2.61E-03
	2	0.7313	2.63E-03
	100 m	0.6199	2.13E-03
275	1	1.1591	4.12E-03
	2	1.1543	4.125E-03
	100 m	0.9864	3.61E-03
375	1	1.5817	5.45E-03
	2	1.5768	5.47E-03
	100 m	1.3525	5.24E-03
525	1	2.2156	7.71E-03
	2	2.2103	7.717E-03
	100 m	1.9014	8.02E-03
600	1	2.5326	8.775E-03
	2	2.5270	8.776E-03
	100 m	2.1626	9.55E-03

E. Scattering of acoustic waves by the sediment

To establish the relative magnitude of the scattering and volume attenuation combination, the difference between computed and measured transmission loss with range was determined as a function of frequency. The losses due to surface and volume scattering are attributed to this difference. The scattering loss may be represented in the model as a thin scattering layer at the water-sediment interface. The representation of the scattering loss within this layer was made by determining the fractional loss of intensity within the layer as

$$\Delta I/\langle I \rangle = \sqrt{\pi} \langle \mu^2 \rangle k^2 a L (1 - e^{-k^2 a^2}), \quad (16)$$

where $\mu = -c/c_0$ spatial fluctuation, k is the wave number, a is the correlation length, and L is the travel distance of the ray through the layer, which for a thin layer compared to the acoustic wavelength is approximated by the thickness of the layer itself (Aki and Richards³⁹). The quality factor Q^{-1} is thus determined by

$$Q^{-1} = \frac{1}{2\pi} \frac{\Delta I}{\langle I \rangle} \quad (17)$$

and the corresponding attenuation is entered in the model scattering layer. This method is used to determine the effect of scattering upon the acoustic propagation.

Since volume attenuation in the sediment has been included in the calculation this increase in loss is due to the surface and volume scattering not included in the SAFARI model. The difference in these trend levels at 20 km is measured and an estimation of the level of surface and volume scattering loss for increasing frequency is then

TABLE III. Scattering model parameters.

Frequency (Hz)	k_h	a	L	μ^2
375	1.5817	0.3 m	1.0 m	0.003
600	2.5326	0.3 m	0.4 m	0.003

made. Due to resolution of the BSMP, high frequencies that have a small acoustic cross section and shallow penetration depth are particularly affected. The method for representing the scattering losses in a thin surface layer as described previously was used for estimation and model assimilation. The values of the horizontal wave number k , correlation length a , layer thickness L , and variance μ^2 are obtained from core samples taken from Wilmington Canyon and are tabulated in Table III.⁴³ Using this scattering approximation method the transmission loss measurements reported by Carey *et al.* were accurately modeled, supporting the hypothesis that the increase in transmission loss with range was due to surface and volume scattering of some variety (Fig. 10). Calculated transmission loss as a function of range and depth are shown in Fig. 6(a) and (c) with and without the scattering at a frequency of 600 Hz. This method for the representation of the loss due to scattering loss is particularly useful in cases involving many layers like AMCOR 6010 where thirteen BSMP sediment layers were input and rough tomography is the case.

Figure 11 shows the attenuations determined for scattering and the intrinsic attenuation of the first mode and the first mode penetrating 100 m as well as the "total"

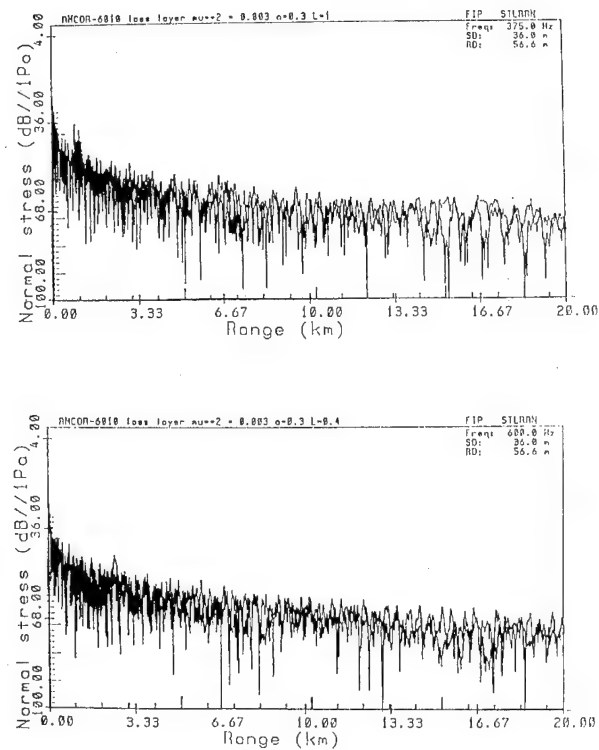


FIG. 10. Transmission loss modeled using thin layer scattering representation with data overlaid.

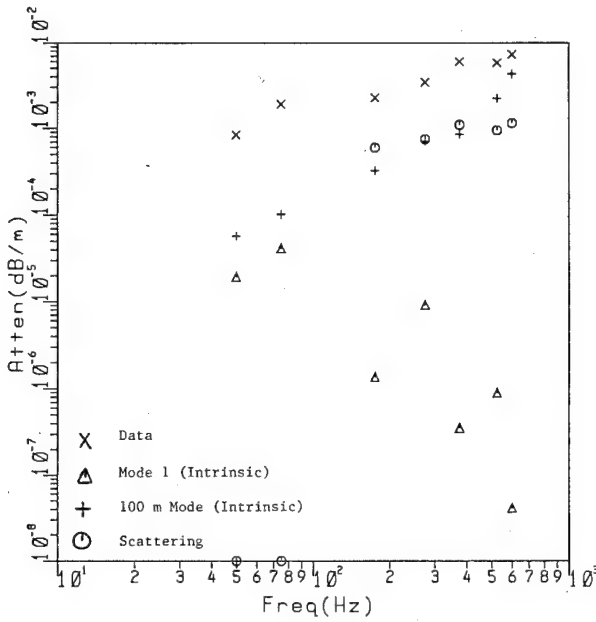


FIG. 11. Attenuations as functions of frequency determined for scattering, the first mode, the first 100-m penetrating mode, and from the transmission loss data.

attenuation of the acoustic signal determined from the transmission loss data. It is interesting to note for the intrinsic attenuation the trend with respect to frequency of the first mode; as frequency is increased there is a reduction in attenuation. This is due to lower sediment penetration depth of the mode with increasing frequency thus lower interaction with the attenuating sediment layers. In contrast, comparison of attenuation as a function of frequency for the mode which penetrates to 100 m shows an increase in attenuation with frequency due to higher attenuation at depth. Therefore attenuation of the mode is both a function of frequency and penetration depth.

III. SUMMARY AND CONCLUSIONS

It has been shown that the compressional and shear wave profiles experimentally obtained by the bottom shear modulus profiler system are viable inputs to acoustic propagation codes by comparison with real data. BSMP provides good resolution over depths required for both mid- and low-frequency acoustic propagation study. The SAFARI calculation based on BSMP environment profiles compared well with low-frequency acoustic propagation measurements. This very good agreement substantiates the BSMP for range independent study. Because of the horizontal resolution (~one water depth) of the BSMP method it could also be useful for range-dependent study as well.

The effect of the shear and compressional speed profiles upon modal structure and consequence transmission loss with range and depth were investigated. It was found that the calculation of the horizontal wave-number spectrum was highly sensitive to the compressional speed profile indicating the extreme importance of accurate near surface compressional speed profiles, not only of the water

column but also of the sediment layers. The calculations showed changes in shear would affect only the energy of the modal spectrum while leaving the eigenvalues themselves unaffected. It was also noted that the higher-order modes were more strongly affected by removing shear than the lower-order modes which propagate almost exclusively in the water column. As the frequency increases, the number of modes becomes large and only those modes with small grazing angles propagate. The higher-order, lower wave-number, modes are attenuated quickly. The net effect is a large group of modes which can be described by their coherent sum.

An anomaly of the AMCOR 6010 site was found in the sediment profiles, a sub-seafloor waveguide. This waveguide, although not as strong a propagator as the water column, was found to have a considerable effect upon the higher-order modes that propagated in this waveguide region. The effect of such sub-seafloor structures has been discussed and reiterates the need for accurate profiles.

The attenuation profile of the sediment was determined using a couple of techniques. The depth-independent profile was first found using the relative intensities of the various modes and methods for extending the mode matching method to a depth-dependent profile were discussed. The more accurate depth-dependent profile was achieved using extended Biot theory and BSMP measured porosity and shear modulus, implemented into the model and compared to the acoustic data. Very good agreement with measured data was found using this method without modification. The individual modal depth-averaged attenuations were found for the first mode of each frequency and the attenuation of the first mode penetrating 100 m. A comparison of intrinsic attenuation with frequency was made. The previous data accumulated by Hamilton was found to have attenuations quite a bit larger than our findings. These previous values were taken largely from extrapolations of higher frequency laboratory and field measurements to the low frequency <1-kHz range. Our results compare more closely with the experimentally determined sediment attenuations found by Mitchell and Focke⁴⁴ for deep ocean sediments to 100-m penetration. The comparison of these various attenuations yielded the frequency dependence of the attenuations. Comparison with previously accumulated data by Hamilton and Stoll shows our experimental analysis to be good for comparison with Biot models and adds to the present database of sediment intrinsic attenuation versus frequency information an experimentally determined set of values. The results of the study fall in a region in the plot from Hamilton and Stoll of what is said to be a sand and silt Biot model. This is consistent with the BSMP prediction for the sediment types at AMCOR 6010 of a combination of sands, silts, and clays.

Scattering was estimated using the transmission loss trends developed by SAFARI (with the intrinsic sediment loss) and the measured transmission loss. A hypothetical scattering model was employed and excellent agreement with the measured results was found. The attenuation due to scattering affects all modes of propagation and this agrees well with the observed case in the acoustic data.

Resolving the lack of range-dependent information and spatial resolution, a full dimensional model will extend study of these reverberative effects of sediment inhomogeneities on acoustic propagation and the attribution of the measured phenomenon to the environmental physics.

ACKNOWLEDGMENTS

Thanks for the contributing efforts of Fred Tappert, Lynne Maiocco, Kevin Smith, and Charlie Monjo. This work was supported by Marshall Orr of the Office of Naval Research, code 1125OA. The Hudson Canyon experiment was supported by ONR and NUSC IR.

- ¹C. L. Pekeris, "Theory of propagation of explosive sound in shallow water," *Geol. Soc. Am. Mem.* No. 27, 1-117 (1948).
- ²I. Tolstoy, "Resonant frequencies and high modes in a layered wave guide," *J. Acoust. Soc. Am.* **28**, 1182-1192 (1956).
- ³L. Tolstoy, "Shallow water test of the theory of layered waveguides," *J. Acoust. Soc. Am.* **30**, 348-361 (1958).
- ⁴I. Tolstoy, "Guided waves in a fluid with continuously variable velocity overlaying an elastic solid: theory and experiment," *J. Acoust. Soc. Am.* **32**, 81-87 (1960).
- ⁵C. S. Clay, "Coherence of waveguide propagation," *J. Acoust. Soc. Am.* **36**, 833-837 (1964).
- ⁶F. Ingenito, "Measurements of mode attenuation coefficients in shallow water," *J. Acoust. Soc. Am.* **53**, 858-863 (1973).
- ⁷J. M. Hovem, "Viscous attenuation of sound in saturated sand," *J. Acoust. Soc. Am.* **66**, 1807-1812 (1979).
- ⁸E. L. Hamilton, "Prediction of *in situ* acoustic and elastic properties of marine sediments," *Geophysics* **36**, 266-284 (1971).
- ⁹E. L. Hamilton, "Geoacoustic modeling of the sea floor," *J. Acoust. Soc. Am.* **68**, 1313-1336 (1980).
- ¹⁰R. D. Stoll, "Acoustic waves in ocean sediments," *Geophysics* **42**, 715-725 (1977).
- ¹¹M. A. Biot, "Theory of propagation of elastic waves in a fluid-saturated porous solid. I. Low frequency range," *J. Acoust. Soc. Am.* **26**, 168-178 (1956).
- ¹²M. A. Biot, "Mechanics of deformation and acoustic propagation in porous media," *J. Acoust. Soc. Am.* **33**, 1482-1498 (1962).
- ¹³F. B. Jensen and W. A. Kuperman, "Experimental acoustic modeling at SACLANTCEN," SACLANTCEN, Rep. No. SR-34, NATO SACLANT ASW Research Center, San Bartolomes, Italy (1979).
- ¹⁴S. Mitchell and K. Focke, "The role of the seabottomattenuation profile in shallow water acoustic propagation," *J. Acoust. Soc. Am.* **73**, 465-473 (1983).
- ¹⁵See Ref. 9.
- ¹⁶A. C. Kibblewhite, "Attenuation of sound in marine sediments: A review with emphasis on new low frequency data," *J. Acoust. Soc. Am.* **86**, 716-738 (1989).
- ¹⁷T. Yamamoto, "Acoustic propagation in the ocean with a poro-elastic bottom," *J. Acoust. Soc. Am.* **73**, 1587-1596 (1983).
- ¹⁸T. Yamamoto and A. Turgut, "Acoustic wave propagation through porous media with arbitrary pore size distributions," *J. Acoust. Soc. Am.* **83**, 1744-1751 (1988).
- ¹⁹H. Schmidt, "Seismo-acoustic fast field algorithm for range independent environments," SACLANT ASW Research Center, I19100 La Spezia, Italy (1987).
- ²⁰F. Tappert, "The parabolic approximation method," in *Wave Propagation and Underwater Acoustics*, edited by J. B. Keller and J. S. Papadakis (Springer-Verlag, Berlin, 1977), pp. 224-287.
- ²¹F. B. Jensen and M. C. Ferla, "SNAP: The SACLANTCEN normal-mode acoustic propagation model," SM-121, La Spezia, Italy (1979).
- ²²I. Tolstoy and C. S. Clay, "Ocean" Acoustics: theory and experiment in underwater sound," Hudson Laboratories, Columbia University (1986).
- ²³R. D. Stoll, *Sediment Acoustics*, Lecture Notes in Earth Sciences Vol. 26 (Springer-Verlag, New York, 1989).
- ²⁴M. Trevorrow and T. Yamamoto, "Summary of marine sedimentary shear modulus and acoustic speed profile results using a gravity wave inversion technique," *J. Acoust. Soc. Am.* **90**, 441-456 (1991).
- ²⁵T. Yamamoto, M. Trevorrow, M. Badiey, and A. Turgut, "Determination of the seabed porosity and shear modulus profiles using a gravity wave inversion," *Geophys. J. Int.* **98** (1), 173-182 (1989).
- ²⁶T. Yamamoto and T. Torii, "Seabed shear modulus profile inversions using surface gravity (water) wave-induced bottom motion," *Geophys. J. R. Astron. Soc.* **85**, 413-431 (1986).
- ²⁷T. Yamamoto, A. Rogers, and M. Trevorrow, "Experimental verification and application of bottom shear modulus profiler (BSMP) method," *Oceans '91, Proceedings* (1991).
- ²⁸M. Trevorrow, T. Yamamoto, M. Badiey, A. Turgut, and C. Conner, "Experimental verification of seabed shear modulus profile inversions using surface gravity (water) wave-induced seabed motion," *Geophys. J.* **93** (3), 419-436 (1988).
- ²⁹W. Carey, "Hudson canyon experiment," FY88 Ocean Acoustics report, NUSC (1988).
- ³⁰L. D. Maiocco, W. Carey, E. Parssinen, and J. Doutt, "Measurement of shallow water sound transmission on the New Jersey continental shelf," *J. Acoust. Soc. Am.* **86**, S8 (1989).
- ³¹W. Carey and L. D. Maiocco, "NUSC/ONR Hudson canyon experiment," NUSC FY90 IR/IED Report, TR 8871, 2-5 to 2-8 (1991).
- ³²G. V. Frisk and J. F. Lynch, "Shallow water waveguide characterization using the Hankel transform," *J. Acoust. Soc. Am.* **76**, 205-216 (1984).
- ³³J. Lynch, S. Rajan, and G. Frisk, "A comparison of broadband and narrow-band modal inversions for bottom geoacoustic properties at a site near Corpus Cristi, Texas," *J. Acoust. Soc. Am.* **89**, 648-665 (1991).
- ³⁴R. J. Cederberg, W. L. Siegman, M. J. Jacobson, and W. M. Carey, "Predictability of acoustic intensity in shallow water at low frequencies using the parabolic approximation," *J. Acoust. Soc. Am.* **89**, 9896(A) (1991).
- ³⁵A. K. Rogers and T. Yamamoto, "Measurement and modelling of acoustic waves in the 50-600 Hz range at the Hudson Canyon site," *J. Acoust. Soc. Am. Suppl. 1* **88**, S106 (1990).
- ³⁶A. K. Rogers, T. Yamamoto, F. Tappert, and W. Carey, "Remote sensing of seabed compressional wave attenuation from cw propagation experiments, combined with the bottom shear modulus profiler (BSMP) database," *J. Acoust. Soc. Am.* **89**, 1882(A) (1991).
- ³⁷M. Trevorrow, T. Yamamoto, A. Turgut, C. Abbott, M. Badiey, D. Goodman, T. Nye, and K. Ando, "Summary of ocean bottom seismic and pressure measurements taken in July, 1988 on the New Jersey shelf and Georges Bank," RSMAS TR-88-005, GAL Report No. 1007 (1988).
- ³⁸J. D. Milliman, Z. Jieza, L. Anchun, and J. Ewing, "Late quaternary sedimentation on the outer end middle New Jersey Continental shelf: Result of two local deglaciations?," *J. Geol.* **98**, 966-976 (1990).
- ³⁹K. Aki and P. G. Richards, *Quantitative Seismology: Theory and Methods* (Freeman, San Francisco, 1980), Vol. 1.
- ⁴⁰J. E. White, *Underground Sound, Application of Seismic Waves, Methods in geochemistry and geophysics* (Elsevier, New York, 1983).
- ⁴¹M. Schulkin and J. A. Mercer, "Low frequency shallow water acoustics (20-500 Hz)," Johns Hopkins University, Applied Physics Laboratory, Report No. 8606 (1986).
- ⁴²M. Schulkin, "Remote sensing of acoustic properties of shallow water sediments," Applied Physics Laboratory, Report No. 8711 (1987).
- ⁴³T. Yamamoto, A. Turgut, M. Schulkin, and R. Bennet, "Geoacoustic Properties of the Sediment Critical to Acoustic reverberation at 50 to 500 Hz: A Preliminary Data Set," RSMAS TR-91-001, GAL Report No. 1014 (1991).
- ⁴⁴S. Mitchell and K. Focke, "New measurements of compressional wave attenuation in deep ocean sediments," *J. Acoust. Soc. Am.* **67**, 1582-1589 (1980).

Reprinted from: *Journal of the Acoustical Society of America*, Vol. 93, No. 4, Pt. 1, April 1993

FIELD TEST OF BURIED OCEAN-WAVE DIRECTIONAL SPECTROMETER SYSTEM

By Tom Nye¹ and Tokuo Yamamoto²

ABSTRACT: This paper presents a new and unique method of measuring the directional spectra of ocean surface waves with a buried instrument containing horizontally oriented seismometers and a pressure sensor. Based upon the assumption that the seabed responds in an elastic, incompressible, and linear manner to ocean-wave-induced pressure fluctuations, the directional spectrum of the sediment motion has been found using the maximum entropy method. This motion is converted to a surface-wave directional spectrum using linear wave theory and the differential pressure gauge's frequency spectrum. This system was incorporated into the Office of Naval Research (ONR) sponsored Sources of Ambient Micro-Seismic Ocean Noise (SAMSON) experiment for three months off the Army Corps of Engineers' Field Research Facility (FRF) near Duck, North Carolina, in the fall of 1990. Four working sensors produced directional spectra results from nearly 22 gigabytes of recorded data that were collected 2 km offshore of the FRF under 12–13 m of water and approximately 1 m of sediment. Comparisons to the FRF's 12-point array of bottom-mounted pressure sensors, which was located 1 km inshore and in 8 m water depth, are made with favorable results.

INTRODUCTION

Nye et al. (1990) introduced the buried ocean-wave directional spectrometer (BOWDS) system to measure the directional spectra of ocean surface waves as part of an existing geoacoustical surveying package known as BSMP (Trevorow et al. 1988). This system consists of two horizontally oriented seismometers and a pressure sensor buried to depths of 1 m in the seabed. The preliminary results were encouraging, but were not verified with an accepted measurement system. As part of the Office of Naval Research (ONR) sponsored Sources of Ambient Micro-Seismic Ocean Noise (SAMSON) experiment near the Army Corps of Engineers' Field Research Facility (FRF) in Duck, North Carolina, the necessary comparisons were made in the fall of 1990 with the FRF's 12-point array of bottom-mounted pressure sensors. This array was located in an 8-m water depth approximately 1 km offshore of the FRF lab. The writers' instruments were located in a 13-m water depth approximately 2 km offshore of the lab.

Estimates of the energy density of ocean surface waves as a function of wave frequency and wave-propagation direction (directional spectra estimates) are essential to many aspects of ocean and coastal engineering. Directional spectra are used in the design and analysis of moorings, piles, and offshore towers; in the prediction of ship response; for wave forecasting and hindcasting; and in the study of sediment transport and pollution control. Therefore, there is interest in finding new methods of measuring the directional spectra of the wave field. Some considerations in choosing a

¹Post-Doc., Univ. of Miami, RSMAS-AMP, 4600 Rickenbacker Cswy., Miami, FL 33149.

²Prof. and Dir. of the Geoacoustic Laboratory, Univ. of Miami, RSMAS/AMP, 4600 Rickenbacker Cswy., Miami, FL.

Note. Discussion open until March 1, 1995. To extend the closing date one month, a written request must be filed with the ASCE Manager of Journals. The manuscript for this paper was submitted for review and possible publication on April 15, 1993. This paper is part of the *Journal of Waterway, Port, Coastal, and Ocean Engineering*, Vol. 120, No. 5, September/October, 1994. ©ASCE, ISSN 0733-950X/94/0005-0451/\$2.00 + \$.25 per page. Paper No. 6001.

system include cost (of equipment, deployment, and data analysis), ease of implementation, longevity, and maintenance. The University of Miami's Geo-Acoustic Laboratory (UM/GAL) has developed this unique system for longevity and low maintenance in shallow-water areas.

Many methods for measuring directional spectra have been utilized in the past. Remote sensing by light or radio waves is possible. For example, tall towers at the ends of an inlet can be used to measure directional spectra near the inlet using stereo photography. Also, satellite imaging can be used. More often, however, one of two types of direct measurements are used. First, measurements can be made from a horizontal array of instruments measuring one wave property; or, second, the spectra can be found from a single instrument package measuring three or more wave properties, as first proposed by Longuet-Higgins et al. (1963).

There are difficulties in providing a proper horizontal array of sensors that some researchers wish to avoid. For example, if the array spacing is larger than one-half the wavelength of the frequency being analyzed, spatial aliasing occurs. However, when the spacing is too small, the long-wave estimates tend to be smeared due to noise (Jeffreys et al. 1982). Therefore, there is a need for many instruments of variable spacing for good resolution without aliasing. Special configurations such as star arrays are used to minimize the number of instruments while maintaining acceptable resolution (Goda 1983). Also, convolution with data-adaptive windows, such as is the case with the maximum likelihood method (MLM) developed by Capon (1983), are used to improve resolution. Another array problem resides in the maintenance and longevity of a large number of sensors and underwater connectors, which are dependent upon one another in many cases.

Observation at a single point (a three-element wave record) is useful for ease of implementation and expense, as well as for measurement of non-uniform wave fields characterized by refraction and diffraction. Use of a single-point instrument package indicates that one is measuring at least three orthogonal components of wave motion within a distance that is very short compared to the shortest wavelength of interest. For example, a pitch-and-roll buoy could measure heave (η), as well as slope of the wave in the x - and y -directions (η_x , and η_y , respectively). Also, a current meter/pressure gauge system could measure fluid velocity in the x - and y -directions (u and v) and pressure at a point. For all methods that measure three orthogonal properties of wave motion, the cross spectra between properties can be shown to produce five Fourier harmonics of motion. A direct fast Fourier transform (FFT) could be used to find the directional spread, but negative sidelobes could develop.

Longuet-Higgins' method of analyzing the cross spectra uses a nonnegative smoothing function to weight the Fourier series of coefficients, which removes the negative sidelobes but produces poor resolution. One method to improve resolution is to fit an assumed directional spreading function to the measured one. These parametrical models are adjusted to minimize the difference between the model and observations (Long and Hasselmann, 1979; Long 1980). However, if the assumed function is independent of the data, the estimate may be biased if the true spectrum is different (Kobune and Hashimoto 1986). Data-adaptive models such as MLM and the maximum entropy method (MEM) have been suggested by Borgman (1982) to remove this bias. MEM has been used by many authors, including Borgman (1985), Briggs (1984), Lygre and Krogstad (1986), and Kobune and Hashimoto (1986), in wave spectral analysis. These do not have fixed window

functions associated with them and therefore can adjust to the true spectrum. Kobune, Hashimoto, Lygre, and Krogstad recognized that the directional spreading function had the same properties as a joint probability distribution function and that therefore information theory could be used to estimate the spreading function. They used cross-spectral values found by a direct Fourier transform, after which the maximum entropy principle is applied to find the spectra.

In this paper, MEM was used following Kobune and Hashimoto (1986) but with data collected from a buried ocean-bottom seismometer (OBS) and a pressure sensor in shallow water. UM/GAL OBSs are designed to contain three orthogonally mounted seismometers, of which only the two horizontals are needed for this analysis. Until now, single-point measurements have been taken using the pitch-roll buoy (measures water-surface elevation and two orthogonal components of surface slope), the clover-leaf buoy (measures the same as a pitch-roll buoy as well as three components of water-surface curvature), and by current meters with a pressure sensor to measure orbital velocities and water-surface elevation. The advantage of the new system developed by UM/GAL is that the entire package can be buried up to 1 m below the seabed, leaving it relatively undisturbed by storms, biological growth, or commercial fisherman. Also, it does not need to be fixed to offshore structures and can be installed under most sediment types at any investigation site in the coastal zone. This system is designed for shallow water (less than 50 m) directional spectra estimates and can be hardwired to a shore station or tethered to a ship or radiotelemetry buoy.

The horizontal seismometers buried in the seabed measure accelerations of the sediment due to disturbances called microseisms. Microseisms are defined as small-amplitude seismic waves that are not caused by discrete seismic events (i.e. earthquakes). The main contributors to the microseismic energy spectra are interface waves traveling on the seafloor. In the gravity-wave frequency band (approximately 0.05–0.33 Hz), the dominating interface wave energy is the seabed motion, which is coupled to the traveling surface gravity waves caused by pressure fluctuations. The model the writers use assumes that the seabed behaves in a massless, incompressible, elastic manner toward the passing surface gravity waves (Yamamoto et al. 1978, 1986). Because the surface waves create a footprint on the seafloor, the directional spreading function can be found for the sediment waves using horizontal seabed accelerations and then combined with the frequency spectra of the surface waves as measured from hydrodynamic pressure to form the directional spectra.

A detailed analysis of using buried horizontal seismometers and the maximum entropy method can be found in previous publications (Nye et al. 1990; Nye 1992).

SAMSON EXPERIMENT

The 1990 experiment offshore of the Corps of Engineers' Field Research Facility (FRF) at Duck, North Carolina (Fig. 1), was part of a multi-institutional Sources of Ambient Micro-Seismic Ocean Noise (SAMSON) experiment. UM/GAL's contribution to this experiment was a nearshore (2 km) seismometer array consisting of six ocean-bottom seismometers with pressure sensors (OBSs). The deployment of this array, which was tuned to find the directional spectra of double-frequency microseisms (the array spacing being too large to find directional spectra of gravity waves using array methods), began on September 6, 1990. Six hundred meters of ar-

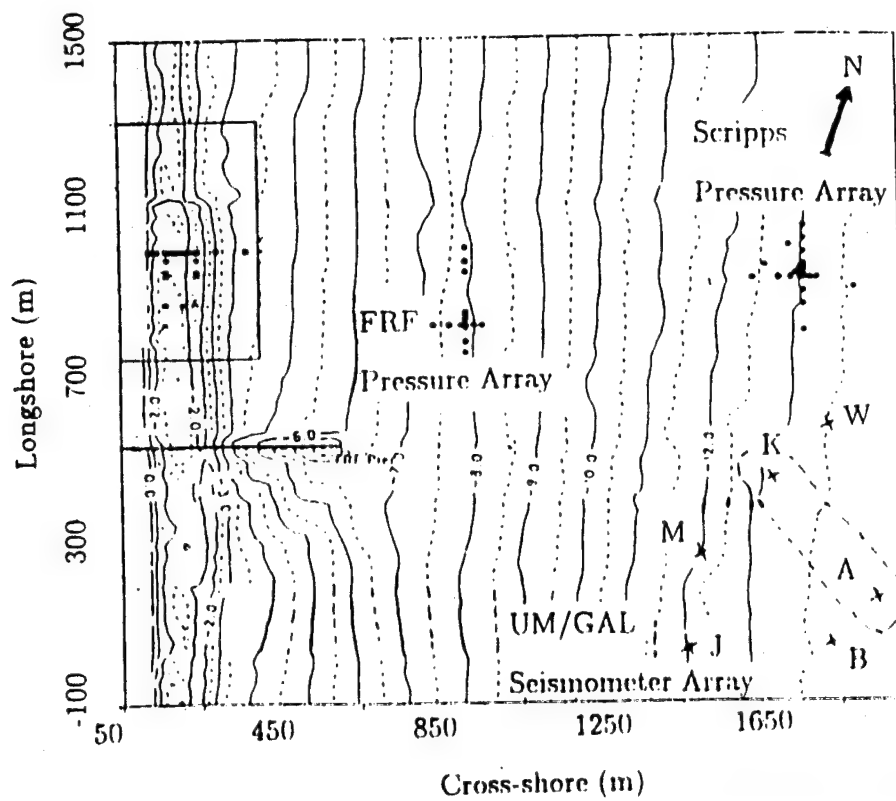


FIG. 1. Sources of Ambient Micro-Seismic Ocean Noise (SAMSON) Experimental Site (Contours Are in Meters)

TABLE 1. Instrument Positions

Instrument (1)	Cross shore (m) (2)	Longshore (m) (3)	Depth (m) (4)
Joanna	1,460	27	12.2
Miyuki	1,502	205	13.7
Ayshe	1,942	130	13.7
Beth	1,817	46	12.8
Karen	1,675	455	13.7
Wendy	1,810	571	13.4

TABLE 2. Instrument Bearings

Instrument (1)	Roll (degrees) (2)	Pitch (degrees) (3)	Heading (H2) (degrees azimuth) (4)
Joanna	0.0	2.0	112
Miyuki	3.5	2.0	82
Ayshe	4.2	3.0	135
Beth	7.5	3.0	107
Karen	5.5	0.4	285
Wendy	7.0	3.0	55

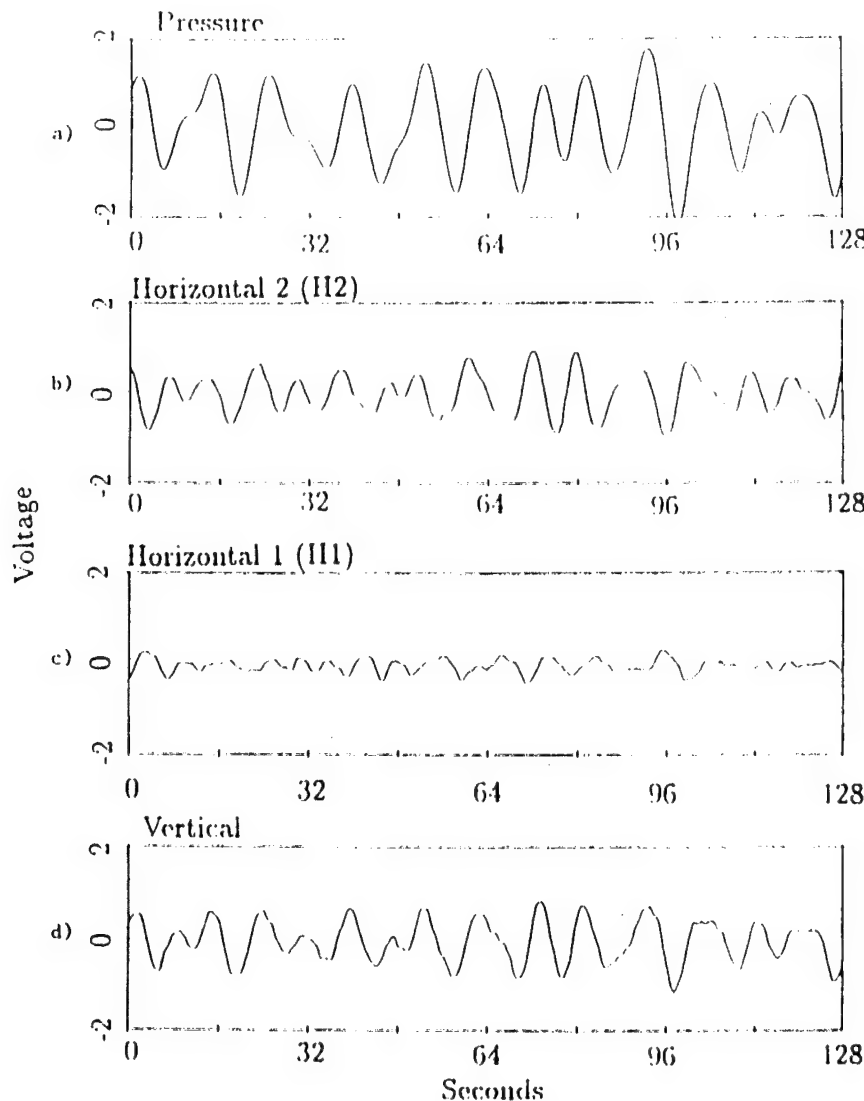


FIG. 2. Example Time Series of Pressure Signal (a), and Three Orthogonal Seismometers [Vertical (d), H1 (c), and H2 (b)]

mored, 1 in. diameter coaxial cable was laid along the FRF pier into the computer laboratory. The remaining 2.4 km of cable was deployed by the *RV Cape Henlopen* using a gasoline-powered reel stand. This cable contained three breakout points for instrument placement at the far end, 600 m in., and 1,200 m in. At these points, three secondary armored, 5/8 in. diameter, 200-m-long coaxial cables were also deployed by the *Cape Henlopen*. In Table 1, the six instrument positions are given in meters cross shore and longshore (*x* and *y*, respectively) from the origin of the FRF coordinate system (Lat. $36^{\circ}10'38.77''$ N and Lon. $75^{\circ}45'0.28''$ W). The six instrument packages were buried using divers and a hydraulic pump jet system that liquefied the sediment, allowing the instruments to settle to depths of 1 m. The accelerometers were leveled by hand. Instrument tilts and headings (direction of horizontal seismometer labeled "H2") are given in Table 2.

For this experiment, the instrument package consisted of three separate units. The first was an accelerometer unit containing three orthogonally mounted seismometers (Teledyne-Geotech models S-750 or S-510), a compass (Aanderaa model 1248), and two pendulum tiltmeters (Sperry model

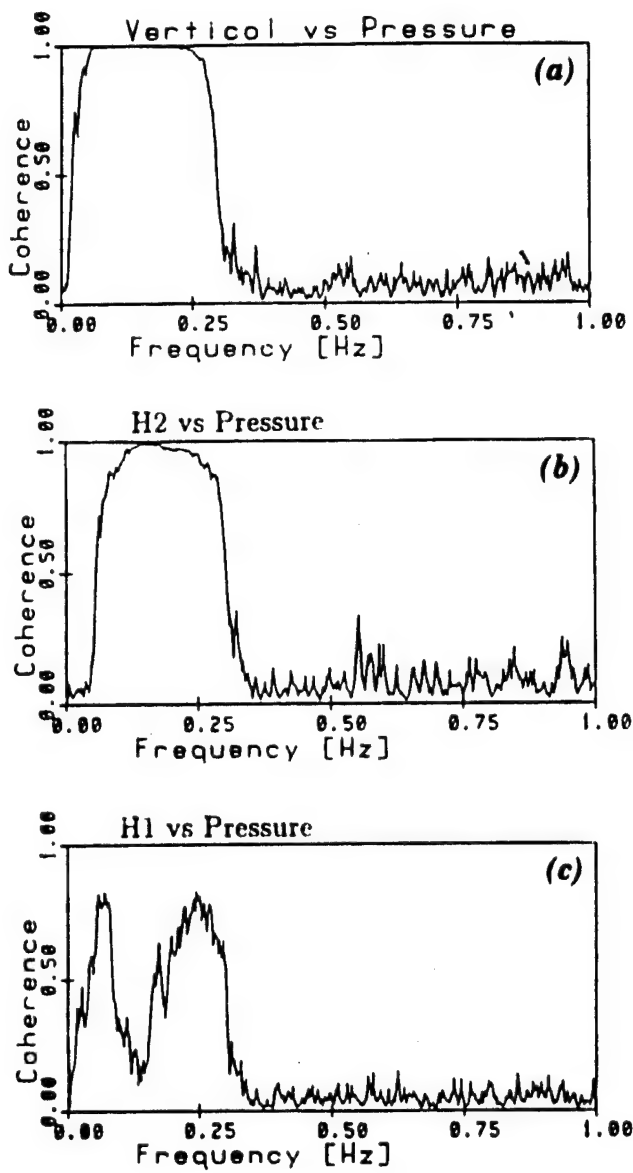


FIG. 3. Coherence between: (a) Pressure/Vertical; (b) Pressure/H2; and (c) Pressure/H1 Signals from Joanna Unit, 2-hr Time Period Ending at 2000 hrs on Oct. 18, 1990, during SAMSON Experiment

02383-01). The accelerometer unit was cased in an aluminum alloy cylinder (diameter 30.5 cm; height = 25.5 cm), which was of approximately neutral density in sediment to provide adequate coupling with the sea bottom, and it was buried with its axis oriented vertically to a depth of 1 m. The second unit in the instrument package was an electronics container that consisted of an aluminum alloy housing (diameter = 23 cm; height = 48 cm) containing instrumental amplifiers, filters, digitizers, and digital multiplexer electronics. This unit served as a junction between the seismometer unit, the pressure sensor, and the electromechanical cable to shore. The final piece of the package was the pressure sensor (Precision Measurements Engineering model 109). The electronics housing and the pressure sensor were buried to depths of approximately 0.5 m to protect them from fishery activity.

The shore unit included a Lambda Electronics (model LLS8120) regulated power supply, coaxial terminator boards, frequency demultiplexer electron-

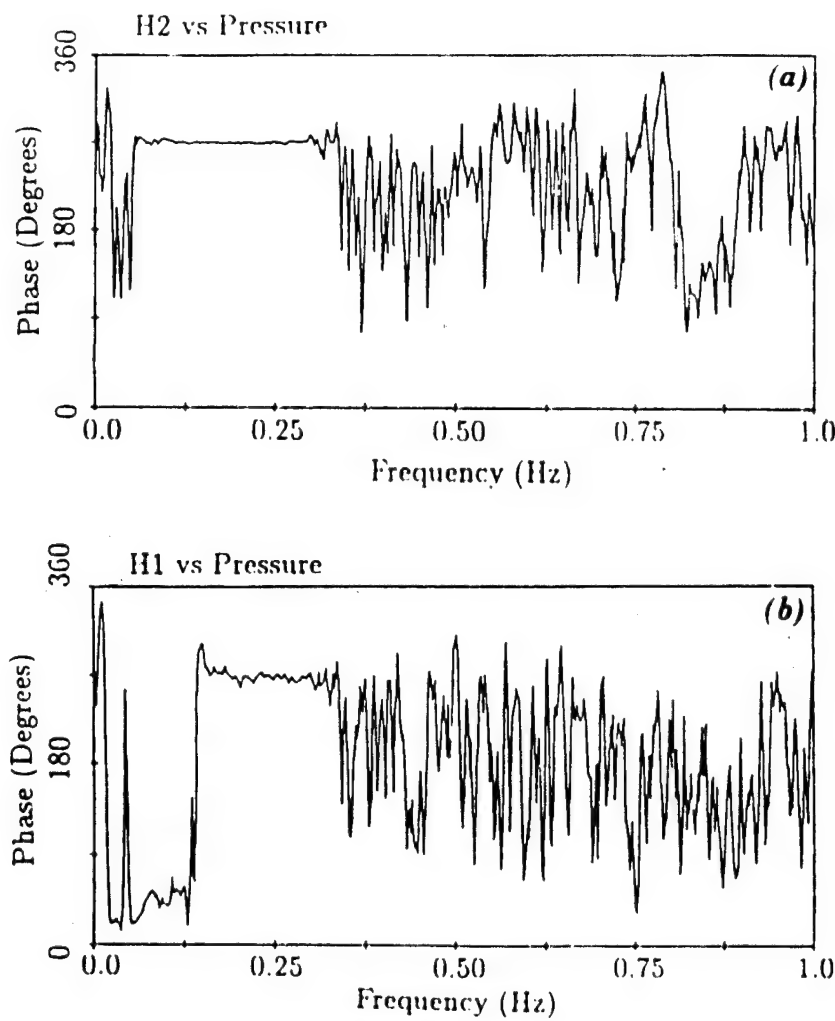


FIG. 4. Phase between: (a) Pressure/H2; and (b) Pressure/H1 Signals from Joanna Unit

ics, and a Digital Vaxstation (model 3200). Power was supplied through the main cable at 50 volts, and the system drew approximately 150 millamps. The seismometer signals, along with the compass, tiltmeter, and pressure signals were transmitted on different carrier frequencies for each of the six instruments. These frequencies range from 1,700 Hz to 13,500 Hz. Following the separation of these signals, 32 channels were recorded continuously by the Vax workstation onto an Exabyte 8-mm data storage system (model 8200).

Data acquisition occurred in 2-hr blocks and was backed up every 32 hrs. This backup took place in the background of the system, therefore recording should never have stopped. Data were originally recorded at 16 Hz. Each data set then had a moving average performed on it and was reduced to 4 Hz by sampling. Eleven 8-mm tapes were used for storage at 2 gigabytes per tape, accounting for 22 gigabytes of stored data.

The initial instrument deployment concluded on September 8. However, upon return to FRF on the September 9, only two units were up and running. Subsequent investigation uncovered a cut in the umbilical from the main cable to the instrument labeled Ayshe. This umbilical was initially repaired on September 10, but needed to be re-repaired by the cable manufacturer on October 6. During this period, the short to seawater apparently caused inductors in two instruments (Ayshe and Karen) to overheat. These induc-

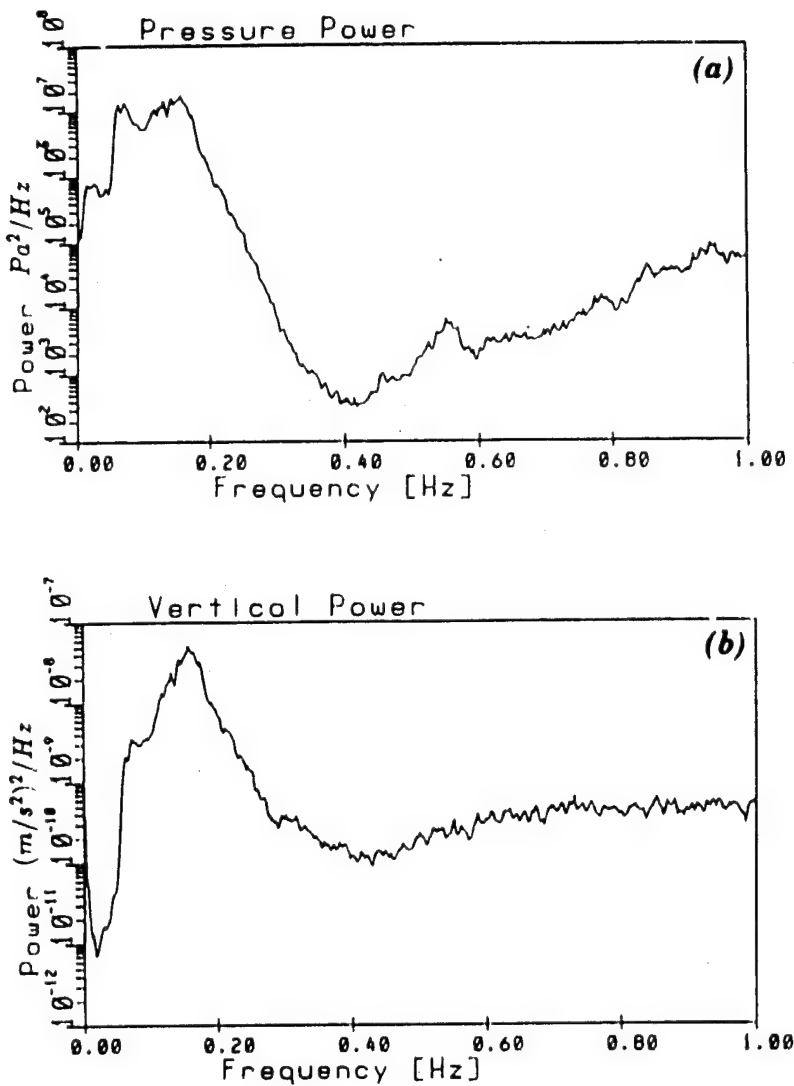


FIG. 5. Power Spectra of: (a) Pressure; and (b) Vertical Seismometer from Joanna Unit

tors were on the digital multiplexer boards built by Teledyne-Geotech and could not be replaced by the start date of the SAMSON project. Therefore these two units were out of commission and the experiment resumed with a four-point accelerometer array. Data acquisition began on October 9. The Joanna and Miyuki units contained the S-750 seismometers, while the Beth and Wendy units contained the older S-510 models. The Wendy unit did not have a pressure sensor. For the purpose of comparing the BOWDS system to the FRF pressure array, the three complete units (Joanna, Miyuki, and Beth) are used in this paper. The loss of instruments is indicative of problems with deploying an array of instruments. Deployments of the BOWDS system as a single unit, as it is designed, have had zero hardware problems.

Some gaps in the data do occur on account of the computer becoming "hung" on several occasions and having to be restarted by FRF personnel. Aside from these few periods, data were collected continuously from October 9 through January 3, 1991, accounting for nearly three months of recording. Continuous recording occurred through a hurricane (Lilly was far offshore but produced large swell), a strong northeaster (the Oregon Inlet bridge was knocked out during this storm), and many commercial

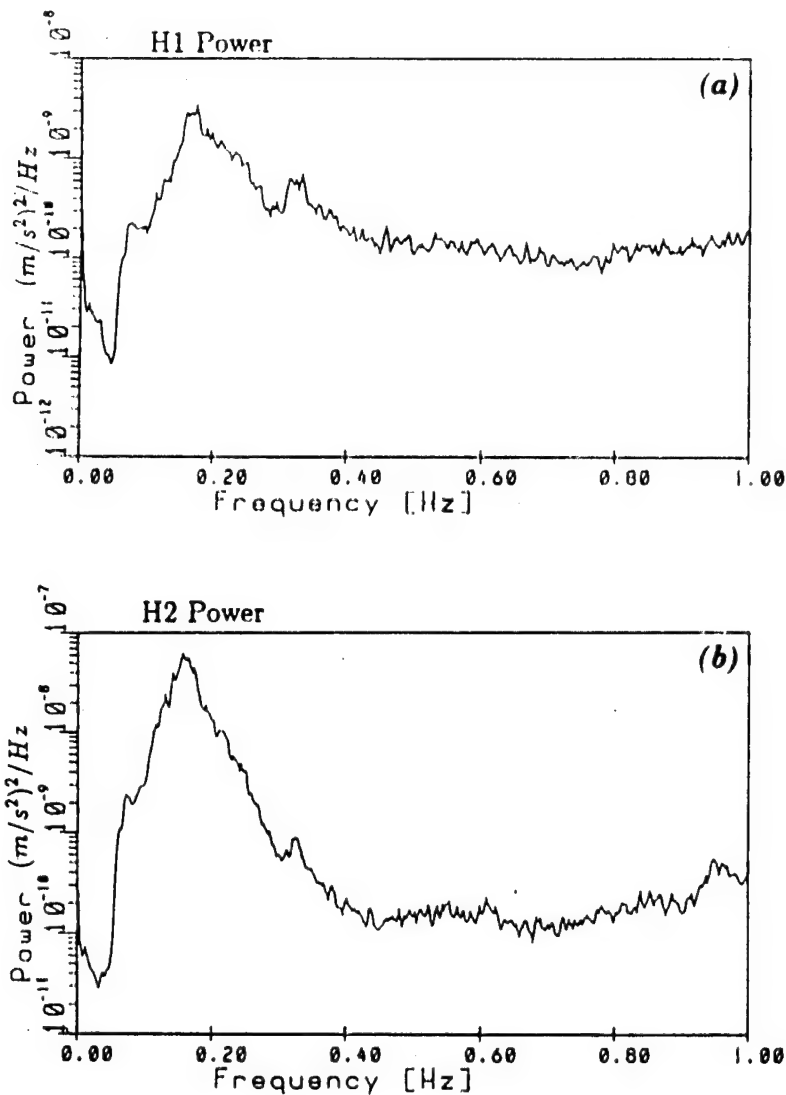


FIG. 6. Power spectra of: (a) H1; and (b) H2 Seismometers from Joanna Unit

fisherman searching for flounder (all of our instrument markers were pulled up, but the instruments remained safe, buried 1 m below the seafloor).

RESULTS

Fig. 2 shows an example of the raw data for the pressure sensor and three orthogonal [vertical and two horizontal directions, (H1 and H2)] seismometers (in this case S-750's) from the SAMSON experiment. One can see that the coherence between pressure, the vertical, and H2 seismometers is very high in the gravity-wave-frequency band. The high-frequency fluctuations carried by the seismometer signals are due to double-frequency microseismic activity (Nye 1992). Fig. 3 graphs coherence versus frequency for the Joanna instrument (for an averaged 2-hr duration ending at 2000 hrs on Oct. 18, 1990). This example of coherence shows a wide band of nearly perfect coupling between the pressure signal and the vertical seismometer in the gravity-wave band. In fact, the vertical seismometer could be used instead of pressure as the third component being measured. The algorithm would then use a different transfer function. The H2 seismometer versus pressure also shows very high coherence in the gravity-wave band. The notable difference between H2/pressure and vertical/pressure is in the

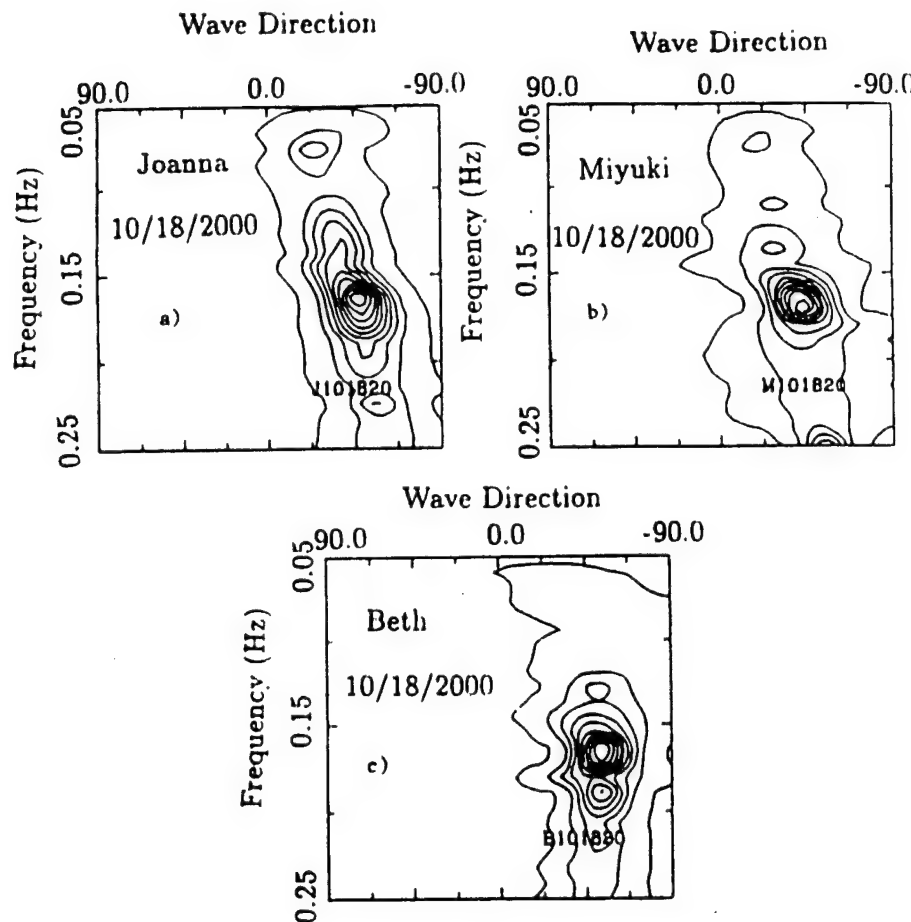


FIG. 7. Directional Spectra Results from 1990 SAMSON Experiment during 2-hr Time Period Ending at 2000 hrs on Oct. 18, 1990 for (a) Joanna; (b) Miyuki; and (c) Beth Instruments

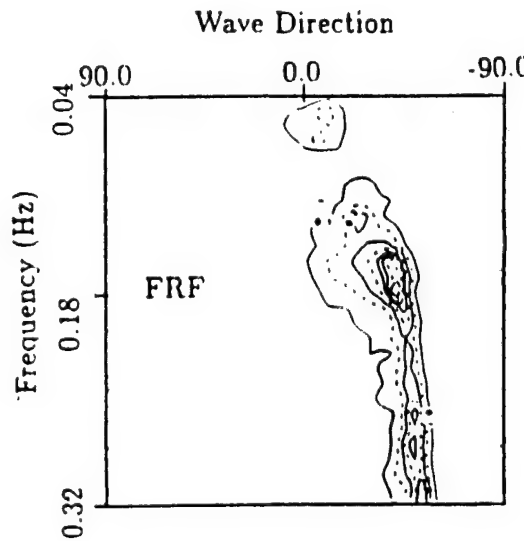


FIG. 8. FRF's Spectrum from 1990 SAMSON Experiment during 3-hr Time Period Ending at 1900 hrs on Oct. 18, 1990

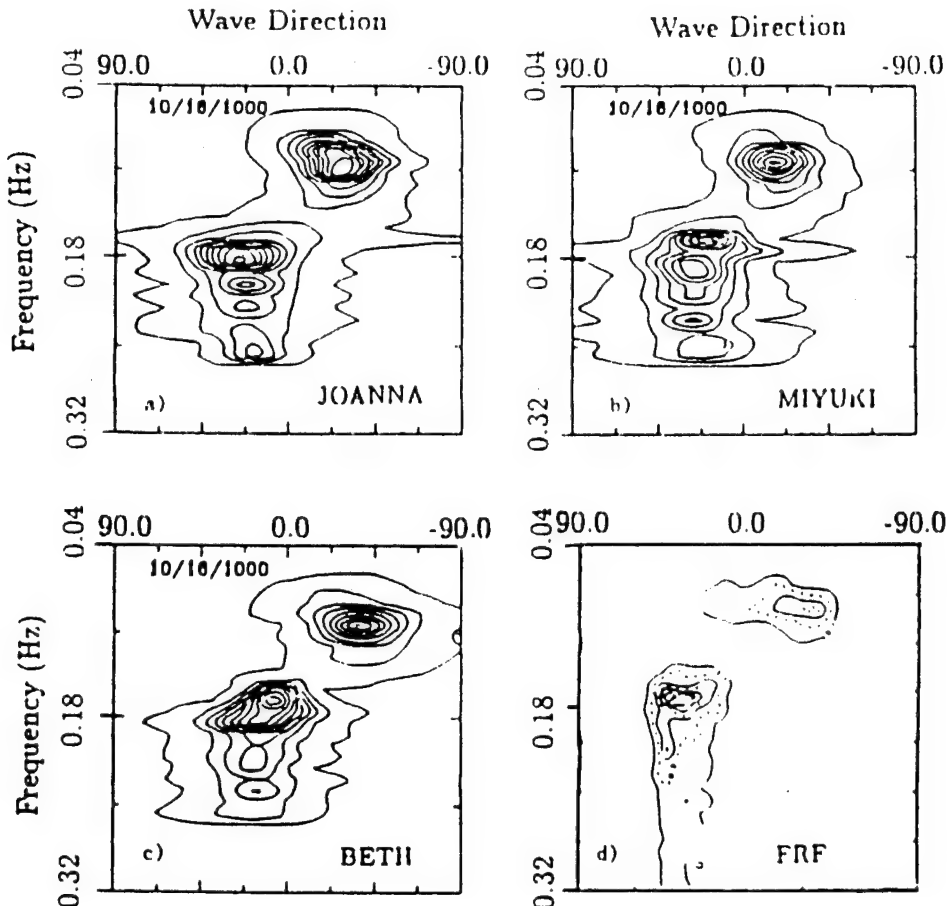


FIG. 9. Directional Spectra Results from 1990 SAMPSON Experiment during 2-hr Time Period Ending at 1000 hrs on Oct. 16, 1990 for (a) Joanna; (b) Miyuki; and (c) Beth Instruments, and for 3-hr Time Period Ending at 1000 hrs on Oct. 16, 1990 for (d) FRF Array

very low frequency range (0.03 Hz) for which H2/pressure shows no coherence. The H1 versus pressure coherence is not as high, especially near 0.14 Hz. This usually indicates that the spectrum is aligned close to the direction of the other seismometer. The very low frequency energy (0.03 Hz) is coherent between H1 and pressure, but the coherence is not very high (0.5). The phase versus frequency for the H2/pressure and H1/pressure cross spectra are given in Fig. 4 for the same data set (Joanna, Oct. 18, 1990; 2000 hrs). For the highly coherent H2/pressure cross spectra, the phase is the expected 270° in the gravity wave band. When the coherence is lower as in the case of the H1/pressure cross, the error in phase is large (away from $\pm 99^\circ$). At the frequency where the coherence was low (0.14 Hz), the phase changed from 90° to 270°. This occurs when the mean wave energy moves slightly from the positive H1 direction to the negative H1 direction. At this frequency, one would expect the spectral peak to be perpendicular to the H1 direction and therefore aligned with the H2 seismometer.

Fig. 5 depicts the power spectra for the pressure and vertical seismometer signals for the Joanna data set (average over 2 hr and terminating at 2000 hrs on Oct. 18, 1990). In general, because of the attenuation of wave energy with depth, waves do not begin to affect the bottom until they approach depths of less than one-half their wavelengths. The inverse $\cosh(kd)$ term from the linear theory transfer function is 8.6% of the surface value when $d/L = 0.5$; therefore, at greater depths, very little energy reaches the

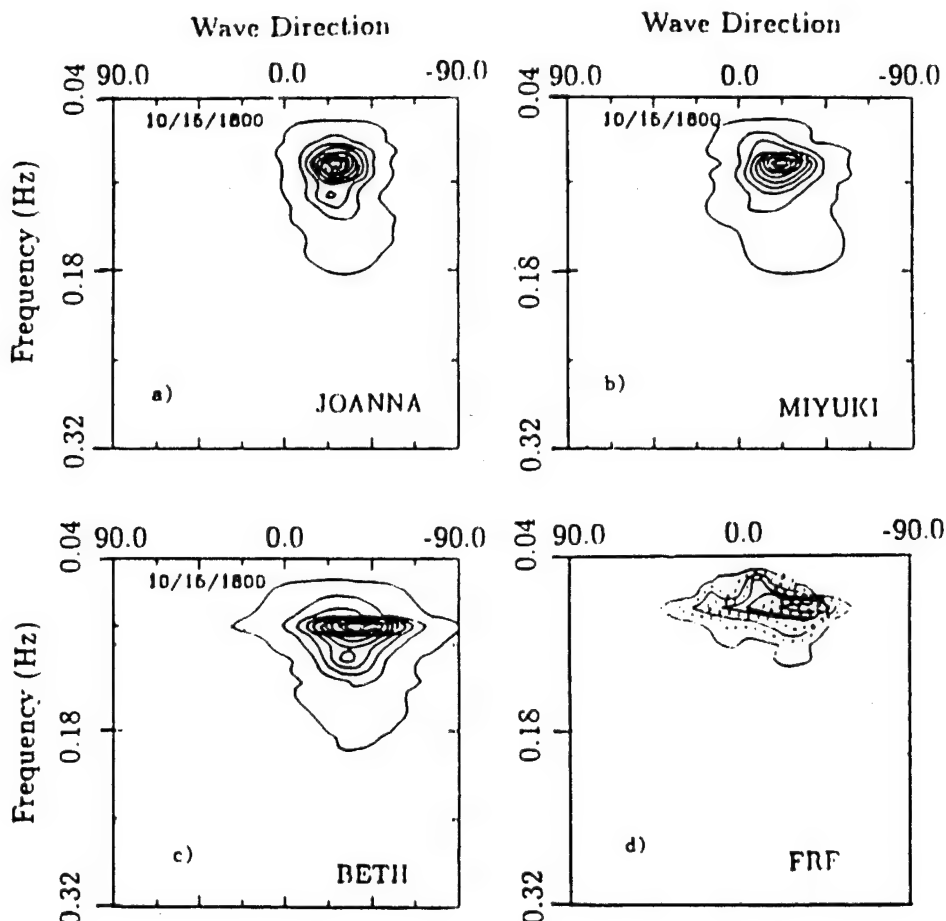


FIG. 10. Directional Spectra Results from 1990 SAMSON Experiment during 2-hr Time Period Ending at 1800 hrs on Oct. 15, 1990 for (a) Joanna; (b) Miyuki; and (c) Beth Instruments, and for 3-hr Time Period Ending at 1900 hrs on Oct. 15, 1990 for (d) FRF Array

seafloor. The instrument depths at the SAMSON site ranged from 12.2 to 13.7 m. Therefore, waves with frequencies less than 0.24–0.26 Hz begin to affect the study areas using this criterion. Therefore, the directional spectra plots of surface gravity waves should range from 0.05 to 0.25 Hz. However, to compare to the Army Corps of Engineer's Field Research Facility's (FRF's) plots, the range for some of the results will be from 0.04 Hz to 0.32 Hz. The pressure sensor does not accurately measure the energy level of waves with higher frequencies than 0.25 Hz. It should show higher-frequency energy due to double-frequency oscillations, which do not appreciably attenuate in these depths. However, the seismometers measure this energy much better than the pressure sensor.

In Fig. 5, a pressure power valley appears to be at 0.4 Hz. The increase in power at higher frequencies is due to instrument noise. However, the small energy peak near 0.3 Hz evident on the vertical and horizontal seismometers' power spectra (Figs. 5 and 6) should appear on the pressure spectra as well but does not. The very low frequency energy (0.03 Hz) is many orders of magnitude down on the vertical plot but remains highly coherent with the pressure signal. The peak H1 power (Fig. 6) is an order of magnitude lower than the H2 and vertical power, which is another indication that the spectrum is aligned with the H2 seismometer.

Directional spectra for the 10/18/90 SAMSON data terminating at 20:00

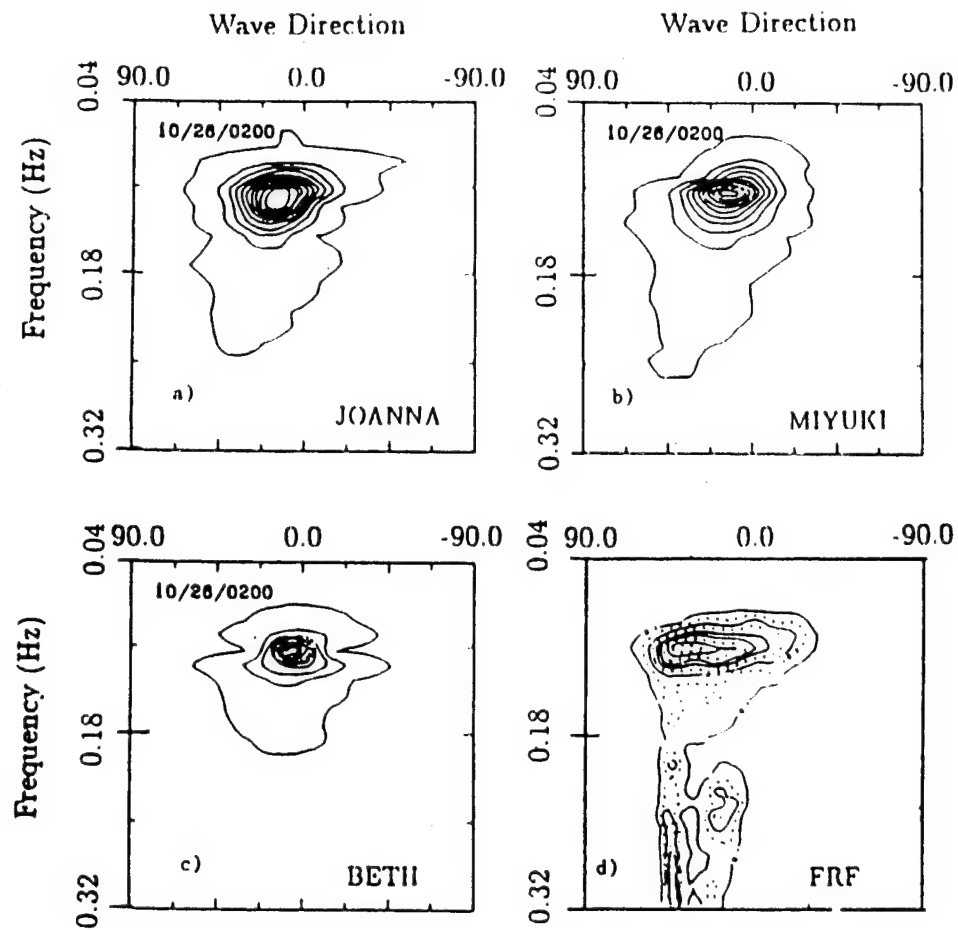


FIG. 11. Directional Spectra Results from 1990 SAMSON Experiment during 2-hr Time Period Ending at 0200 hrs on Oct. 26, 1990 for (a) Joanna; (b) Miyuki; and (c) Beth Instruments, and for 3-hr Time Period Ending at 0400 hrs on Oct. 26, 1990 for (d) FRF Array

hrs is given in Fig. 7 using a 2-hr average. The scale has been selected to facilitate the comparisons to the FRF's pressure array plots. This scale is unconventional, but it matches the output from the Corps of Engineers' reports. The *x*-axis represents wave direction relative to coastline normal (FRF's pier direction). Positive angles represent waves coming from north of the pier, negative angles represent from south of the pier. Because the North Carolina beach is not aligned north-south, the pier azimuthal direction is 70°. Therefore, waves traveling from due east are represented on these plots at -20°. The contours are wave energy in tenths of the maximum because the scale is normalized by the maximum of each spectrum. Therefore, the contour interval can vary from plot to plot, but this again coincides with the FRF graphs.

As expected, the peak of the spectra occurs in the direction coinciding with Joanna's H2 seismometer (heading 112°, -45° on this plot represents 115° azimuthal). At lower frequencies, the swell travels more from the east, and the high frequency wind-driven energy comes from the southeast. The three spectral plots are in general agreement. Unfortunately, the directional heading of Beth is not as precise as the other two. When the Ayshe/Karen instruments failed, the compass of Beth began to introduce spikes into the seismometer signals and had to be disconnected. The Ayshe-Beth and Karen-Wendy instrument pairs were each connected through electronic junction

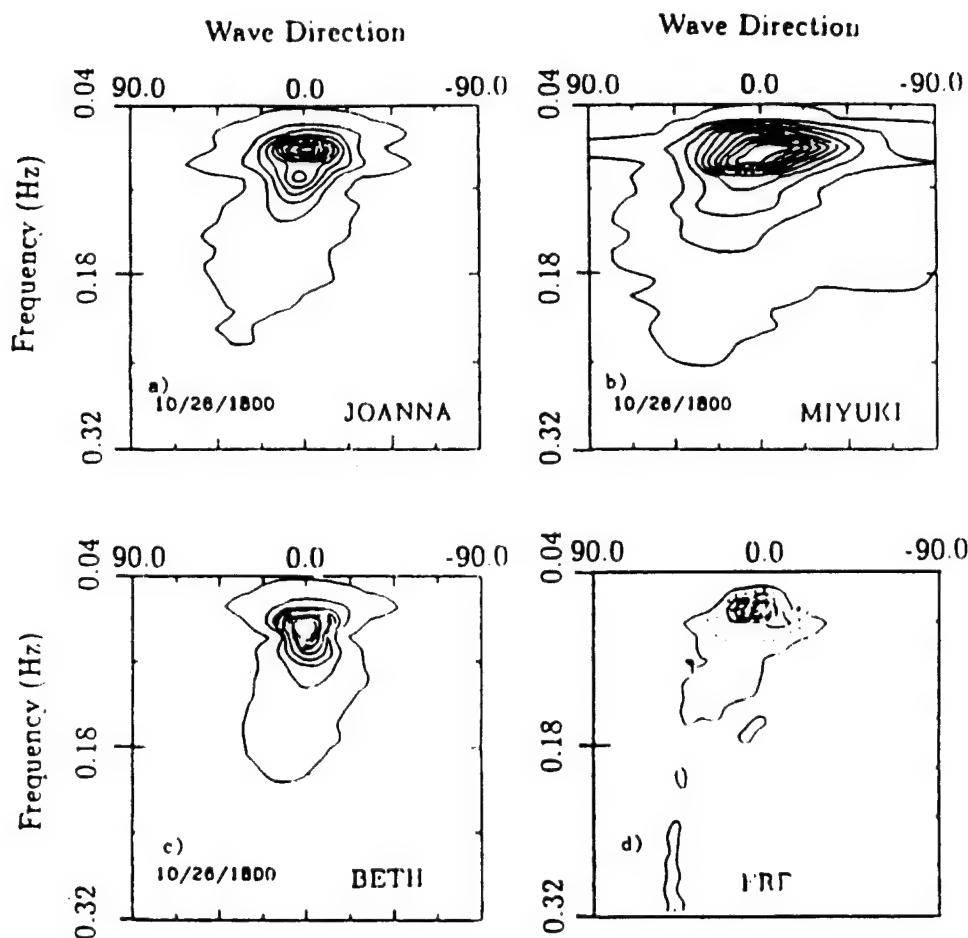


FIG. 12. Directional Spectra Results from 1990 SAMSON Experiment during 2-hr Time Period Ending at 1800 hrs on Oct. 26, 1990 for (a) Joanna; (b) Miyuki; and (c) Beth Instruments, and for 3-hr Time Period Ending on Oct. 26, 1990 for (d) FRF Array

boxes that contained the power supply to the compasses. It was in the junction boxes that the meltdown occurred. The heading of Beth was taken manually and one can see the slight offset. This offset remains constant throughout the experiment. The significant wave height measured by these instruments was approximately 1.1 m.

Fig. 8 shows the result that the FRF's pressure array obtained for nearly the same time period (reproduced from FRF staff personal communication). The FRF spectrum is averaged over 3 hr for the time period ending at 1900 hrs on October 18. The pressure array is in shallower water (8 m) and therefore can estimate spectra to higher frequencies. The spectral peak of this plot resides at 0.16 Hz, -45° , which closely matches the results from the UM/GAL seismometers. The swell (0.05 Hz) is shown closer to -10° than the -20° of the UM/GAL plots. However, the swell energy refracts as the waves shoal from the UM/GAL's 13 m water depth to the FRF's 8 m. From linear wave theory, approximately 4° of the difference can be attributed to refraction. The major difference between the plots is the half-power width of the spectra, which is approximately 25° for the Joanna, Beth, and Miyuki instruments; but only 10° for the result of the array. The spectra probably does tighten as the waves shoal, but one must assume that the array resolves the narrow spectra better. Perhaps a more interesting data set is shown in Fig. 9. These plots depict the gravity-wave directional spectra

for the Joanna, Miyuki, and Beth units for the 2-hr time period finishing 1000 hrs on October 16. The graph in Fig. 9(d) is from the FRF array of pressure sensors averaged over 3 hr, from 0700 to 1000 hrs on October 16. These graphs indicate two predominant sea types at -20° , 0.9 Hz and 30° , 0.16 Hz. The seas meet at approximately 0.13 Hz. Again, the three UM/GAL instruments show good agreement. They also agree well with the FRF's pressure-array spectral estimation for the same time period. For this data set, the half-power spectral width of the swell peak ranges from 30° to 45° for the UM/GAL plots, and is approximately 40° for the FRF plot. Again, the wind-driven peak is narrower on the pressure array plot. The significant wave height for this time period was approximately 0.9 m.

Fig. 10 displays the comparison of the UM/GAL's directional spectra versus FRF's spectra for the 2-hr time period ending at 1800 hrs on October 15. (FRF is again averaged over 3 hr and terminates at 1900 hrs on October 15). This data set is characterized by offshore swell at 0.08 Hz coming from 30° south of the FRF pier (100° azimuthal) with 0.5 m significant wave height. The three single-point sensors agree with the result from the array with Beth showing the closest resemblance. The half-power width of the spectra for both the FRF result and the Beth result is approximately 50° . The other two sensors indicate a narrower spectrum (about 30° half-power width). The Beth unit's result is again shifted to the southeast due to the compass problem that occurred during redeployment.

Beginning on the evening of Oct. 25, 1990 and lasting until early on October 27, a strong early-winter storm passed through the study area (referred to as a northeaster). This storm blew a ship into the Oregon Inlet bridge (about 60 mi south of Duck), which destroyed a section of it. Figs. 11 and 12 display the directional spectra results from during the storm. Although the storm did affect our instruments as we will see later, the event was able to be recorded by our instruments because they were buried beneath the seafloor. Fig. 11 shows the directional spectra estimate for the 2-hr time period terminating at 0200 hrs on October 26 for the Miyuki, Joanna, and Beth units and the FRF pressure array. The FRF graph is a 3-hr average ending at 0400 hrs on October 26. The significant wave height is 4 m and the wind speed is 22 m/s during this time period. The spectral peak is at 0.11 Hz, and the energy propagates from 20° northeast of the FRF pier. The high-frequency energy apparent in the FRF plot is not capable of being measured by the deeper-water UM/GAL instruments. At 1100 hrs on the morning of October 26 the sediment near the unit name Miyuki became temporarily liquefied by the storm and the instrument tilted. This is assumed because of the noise encountered during this time period, and the subsequent loss of spatial vertical-to-vertical coherence with the other instruments. This could occur when the instrument is no longer coupled to the seabed (either unearthened and moving with bottom currents or in liquefied sediment). Because this unit was found approximately 1 m below its burial depth, liquefaction is a more likely cause. The result of the horizontal seismometers being tilted out of the horizontal plane is a less-accurate spectrum, as seen in Fig. 12, which represents the 2-hr time period ending at 1800 hrs on October 26 for the Miyuki, Joanna, and Beth units, and the FRF pressure array. The significant wave height has diminished to 3.0 m and the wind has dropped to 12.4 m/s. The spectral peak of the directional spectra is 0.06 Hz coming from directly offshore of the FRF pier (70° azimuthal). Notice that the half-power width of the Miyuki spectrum is much wider (55°) than the Joanna plot (30°) or the Beth and FRF plots (20°). When the seis-

mometers tilt out of the horizontal plane, errors in the cross spectra cause the phase to move away from ($\pm 90^\circ$) and the directional accuracy to decrease. Comparisons later in the storm with the FRF pressure array cannot be made, because the array went down soon after this last time period for about 24 hr.

COMMENT AND CONCLUSION

This paper presented the results of a new and unique method of measuring the directional spectra of ocean surface waves with a buried instrument containing horizontally oriented seismometers and a pressure sensor. Based upon the assumption that the seabed responds in an elastic, incompressible, and linear manner to ocean-wave-induced pressure fluctuations, the directional spectra of the sediment motion was found using the maximum entropy method. This motion was converted to a surface-wave directional spectrum using linear wave theory and the differential pressure gauges' frequency spectrum.

Comparisons to the FRF's 12-point array of bottom-mounted pressure sensors, which was located 1 km inshore and in an 8-m water depth, were made with favorable results. Comparisons between the methods for unidirectional, bidirectional, and storm sea states were made, with each indicating that point measurements of directional spectra with a buried OBS are accurate. The major differences between the two methods were found at higher frequencies than the deepwater cutoff for the deeper UM/GAL experimental site. For frequencies below 0.25 Hz, the directional spectra of the array and the buried OBS were closely matched.

Because cross spectra between three signals yields only five independent Fourier harmonics, resolving seas that are narrowly bidirectional (less than 40°) becomes impossible with single-point systems. The primary drawback of any bottom-mounted system is the attenuation of wave motion with depth resulting in only low-frequency energy reaching the seafloor in deeper experimental sites. Most directional-spectra-measuring devices (bottom-mounted pressure arrays or pitch-and-roll buoys) encounter one or the other of these problems, and the buried OBS method has both. The advantages, on the other hand, lie in the burial of the unit. By having a system that is almost oblivious to storms, fisheries, etc., one can measure spectra during periods of time or in coastal areas that were previously unattainable. It has been shown that when the storm waves were large enough, the units could be affected; however, the units are much safer at 1 m below the seafloor than they are resting on it.

ACKNOWLEDGMENTS

This work was supported under several Office of Naval Research contracts between 1990 and 1993 in the sections of Ocean Acoustics and Geology and Geophysics. We would also like to thank the staff of the Field Research Facility of the Army Corps of Engineers in Duck, North Carolina headed by Bill Berkemeyer, and the crew of the *RV Cape Henlopen* out of the University of Delaware.

APPENDIX. REFERENCES

Borgman, L. E. (1982). "Maximum entropy and data-adaptive procedures in the investigation of ocean waves." *Proc., 2nd Workshop on Maximum Entropy and Bayesian Methods in Applied Statistics*, Laramie, Wyo.

Borgman, L. E. (1985). "Maximum-entropy and data-adaptive procedures in the investigations of ocean waves." *Maximum-entropy and Bayesian methods in inverse problems*, C. R. Smith and W. T. Grady, eds., D. Reidel Publ. Co., Amsterdam, The Netherlands, 429-442.

Briggs, M. (1984). "Chapter 33: calculation of direction wave spectra by the maximum entropy method of special analysis." *Rep.*, ICCE, Houston, Tex., 484-500.

Capon, J. (1983). "Chapter 5." *Topics in applied physics 34: nonlinear methods of spectral analysis*, 2nd Ed., S. Haykin, ed., Springer-Verlag, Berlin, Germany.

Goda, Y. (1983). *Random seas and design of maritime structures*. University of Tokyo Press, Tokyo, Japan.

Jeffreys, E. R., et al. (1982). "Measuring directional spectra with the MLM." *Directional wave spectra applications*. ASCE, New York, N.Y. 203-219.

Kobune, K., Hashimoto, N. (1986). "Estimation of directional spectra from the maximum entropy principle." *Proc., 5th Int. Offshore Mech. and Arctic Engrg., (OMAE) Symp.*, Port and Harbor Res. Inst., Tokyo, Japan, 80-85.

Long, R., and Hasselman, K. (1979). "A variational technique for extracting directional spectra from multi-component wave data." *J. Phys. Oceanography*, 9, 373-381.

Long R., (1980). "The statistical evaluation of directional spectrum estimates derived from pitch roll buoy data." *J. Phys. Oceanography*, 10, 944-952.

Longuet-Higgins, M. S., Cartwright, D. G., and Smith N. D. (1963). "Observations of the directional spectrum of sea waves using motions of a floating buoy." *Ocean wave spectra*. Prentice-Hall, Inc. Engelwood Cliffs, New Jersey, 111-136.

Lygre, A., and Krogstad, H. (1986). "Maximum entropy estimation of the directional distribution in ocean wave spectra." *J. Phys. Oceanography*, 16, 2052-2060.

Nye, T. (1992). "Measurements of the directional spectra of surface gravity waves and seafloor microseisms using a pressure sensor and two buried horizontal seismometers". PhD dissertation, University of Miami, Miami, Fla.

Nye, T., Yamamoto, T., and Trevorrow, M. (1990). "Measurement of the directional spectra of shallow water waves using the maximum entropy principle and a single bottom seismometer." *J. Atmos. and Oceanic Tech.*, 7(5).

Trevorrow, M., et al. (1988). "Experimental verification of sea-bed shear modulus profile inversions using surface gravity (water) wave-induced sea-bed motion." *Geophys. J. Royal Astr. Soc.*, 93, 419-496

Yamamoto, T. (1977). "Wave induced instabilities in seabed." *Proc., ASCE Symp., Coast. Sediment '77*, ASCE, New York, N.Y.

Yamamoto, T., and Torii, T. (1986). "Seabed shear modulus profile inversions using surface gravity (water) wave-induced bottom motion." *Geophys. J. Royal Astr. Soc.*, 85, 413-431.

Porosity, permeability, shear strength: Crosswell tomography below an iron foundry

Tokuu Yamamoto*, Tom Nye*, and Murat Kuru*

Porosity, permeability, shear strength: Crosswell tomography below an iron foundry

Tokua Yamamoto*, Tom Nye*, and Murat Kuru*

ABSTRACT

Crosswell tomography of a sedimentary foundation at an iron foundry was affected by very high background noise; nevertheless, high-resolution velocity images were obtained between wells separated by long distances (120 to 250 m). A piezoelectric source in a water-filled well used long sequences (4095 cycles) of pseudorandom binary codes at high carrier frequencies (1 to 10 kHz). A 24-channel hydrophone array in another well received the signal. Beamforming of common-source data selected the directions and arrival times of multiple raypaths and tube waves and further enhanced the signal-to-noise ratio. Inversion of first-arrival times by damped least squares imaged the compressional wave velocities. Assuming the normal consolidation condition, the porosity and shear strength images are predicted from the compressional wave velocity image. The direct measurements of porosity and shear strength conducted on the cores and boreholes were used to verify the tomographic predictions. The slight differences in the compressional wave velocity images obtained using different carrier frequencies can be used to determine the permeability image of sediments based on the Biot theory.

INTRODUCTION

The determination of the material properties of sediments, such as porosity, permeability, and shear strength, using acoustic waves is an important and challenging problem of geophysics with practical applications in civil engineering, groundwater geology, and petroleum geology. Modern seismic methods such as crosswell acoustic tomography and multichannel seismic reflection provide acoustic velocity images of the earth. On the other hand, various theories (Wood, 1941; Gassmann, 1951; Biot, 1956 a, b; Murphy et

al., 1986; Johnson et al., 1987; Yamamoto and Turgut, 1988; Dvorkin and Nur, 1993) of acoustic wave propagation through porous media and empirical relations (Hamilton, 1972; Han et al., 1986; Ohsaki and Iwasaki, 1973; Hara et al., 1974; Yamamoto et al., 1989) have been proposed to relate the acoustic velocity and attenuation in sediment to the physical properties of the material. Theoretical and empirical models are reviewed by White (1983), Johnson and Sen (1984), Ishihara (1976), Nur and Wang (1989), and Bourbié et al. (1987). However, very few attempts have been made to directly extract the material properties of sediments from the measured velocity images using these theories and empirical relationships.

In this paper, we show an example procedure of direct extraction of the porosity, permeability, and shear strength from the acoustic velocity images obtained from high-resolution crosswell tomography experiments conducted through alluvial sediments under an iron foundry near Tokyo. The geology of this site is characterized by very soft clay layers interbedded between several sand layers. The alluvial sediment is being consolidated continuously under its own weight and fill material. Continuous monitoring of the consolidation process within the sediment strata and location of supporting sand layers for the steel piles needed for the foundations of a future plant were the two immediate objectives of the crosswell experiments.

Crosswell tomography at the iron foundry was affected by very high background noise; nevertheless, the pulse compression and beamforming techniques enabled us to obtain high-resolution (approximately 1.5 m) velocity images of the earth between wells separated by long distances (up to 250 m). A broadband piezoelectric source in a water-filled well used long sequences (4095 cycles) of phase-modulated pseudorandom binary sequence codes at high carrier frequencies (1 to 10 kHz). A 24-channel hydrophone array at a 2-m interelement spacing in another well received and beamformed the signal for accurate picking of the arrival times of multiple raypaths. Inversions of first-arrival times by a damped least-squares traveltimes inversion code

Manuscript received by the Editor January 19, 1993; revised manuscript received May 4, 1994.

*Rosenstiel School of Marine/Atmospheric Science, University of Miami, 4600 Rickenbacker Causeway, Miami, FL 33149-1098.
© 1994 Society of Exploration Geophysicists. All rights reserved.

(Bregman et al., 1989) imaged the compressional wave velocities.

Because the Biot (1956 a, b) theory is known to adequately model acoustic wave propagation through water-saturated unconsolidated sediments (Stoll, 1980; Gibson and Toksöz, 1989; Yamamoto and Turgut, 1988; Turgut and Yamamoto, 1990), we used Biot's model in the analysis to extract the sediment properties from velocity images. In addition, we assumed that the sediments are consolidated in a normal fashion and satisfy empirical relations between the shear modulus and the porosity found by many investigators (Richart et al., 1970; Ishihara, 1976; Bryan and Stoll, 1988; Yamamoto et al., 1989). The porosity and shear strength estimates extracted from the velocity images were compared to direct measurements of porosity and shear strength performed on cores, standard penetration tests, and stratigraphic data. The slight differences in the compressional-wave velocity obtained using different carrier frequencies enabled us to determine the permeability image of sediments based on the Biot theory.

SEISMIC EXPERIMENTS

The crosswell acoustic tomography experiments were conducted in November 1991 at the Kawasaki Steel Chiba iron foundry, a 5 km \times 5 km man-made island in the middle of Tokyo Bay. The geology below 10 m from the ground surface is the original alluvial sediment bed and is characterized by sand layers and sand lenses floating in a body of soft, unconsolidated clay. The top 10 m or so is landfill made of slags (porous gravel-like exhaust material from the iron foundry) which strongly attenuates acoustic waves. The island is subsiding because the soft clay is still consolidating under the load of the landfill. This is a common and serious problem of man-made islands built on alluvial sediments such as the Kansai International Airport recently built in Osaka Bay. However, the subground process of the island subsidence has not been well monitored or documented. Crosswell acoustic tomography may offer a means to investigate the problem. Permanent structures are built on long steel piles that penetrate down to a firm sediment layer. The objectives of the experiments were to monitor the state of consolidation of the alluvial sediment layers and to locate a firm sand layer for the pile foundations. In addition, we attempted to measure the permeability of the sand layers using acoustic crosswell tomography in Florida beach sands. The permeability measurement can be added to future extractions of material properties from acoustic tomography experiments.

The locations of the five boreholes (labeled 9, 11, 12, 15, 20) used for the experiments and the crosswell distances are shown in Figure 1. Each borehole was 60-m deep and cased with a 6-inch plastic pipe. A piezoelectric source (International Transducer Corporation model No. 6121) placed in one of the wells sent long sequences (4095 cycles) of phase-modulated pseudorandom binary codes continuously by repeating the sequence. The source strength at 1 kHz was 180 dB (relative to 1 μ Pa at 1 m) and was 200 dB between 3 and 10 kHz. A 24-channel hydrophone array in a second well received the signal. Each hydrophone channel had two Teledyne T-2 phones and a preamplifier and was

separated by 2 m. The depth of the source was varied to create an array of source-to-receiver raypaths. A damped least-squares inversion technique was used to convert the matrix of traveltimes for each raypath into a grid of compressional velocities. Ray-tracing techniques were used for the forward theory.

The high background noise generated by the iron foundry and the construction equipment affected the crosswell acoustic tomography experiments. The pulse compression of the pseudorandom sequence was used to enhance the signal-to-noise ratio of data.

When applying wave theory to measured velocity data for interpretation, it must be known whether the velocity data is a phase velocity or a group velocity. In our experiments, we propagated a continuous wave of phase-modulated pseudorandom binary sequences from the source to the receivers. Crosscorrelation of the source signal and a received signal (pulse compression) determines the phase difference between the two as an arrival time; therefore, we measure phase velocities from our crosswell experiments. Phase velocities are used in the equations in this paper. If arrival times are measured directly from the time record of disturbances generated by an explosive source, the measured velocities would be group velocities. The difference between the two velocities are on the order of the intrinsic attenuation of the sediments, usually a few percent at most (Biot, 1956b). Therefore, the errors as a result of assuming measured velocities as phase velocities are relatively small in a practical sense.

An advantage of the present pulse compression technique over an explosive source is that one can measure the velocity images at desired wave frequencies by simply changing the carrier frequency of the pseudorandom binary sequence code. This is essential for creating a permeability image because permeability estimation requires velocity

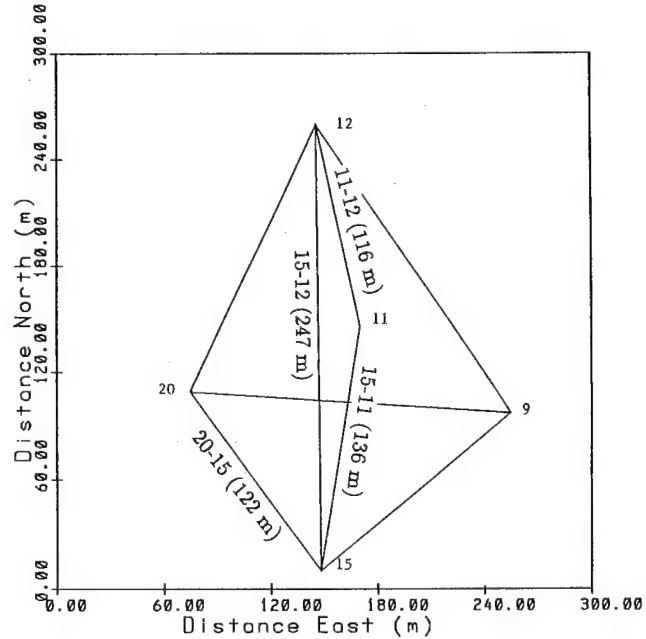


FIG. 1. Tokyo Bay boreholes—plan view.

images at many frequencies. An explosive source does not provide this flexibility.

THEORETICAL BACKGROUND OF ROCK PHYSICS TRANSFORMATION

In this section we give a brief review of rock physics relative to the transformation procedure we used to convert seismic velocity images into material property images.

Justification of the Biot theory as a sediment model

Biot (1956a, b) was the first to formulate acoustic wave propagation through fluid-filled porous media. The fluid-solid viscous interaction is expressed in terms of the permeability and a viscous correction factor, which in turn is a function of frequency and pore size. Yamamoto and Turgut (1988) obtained the mathematical expression for the viscous correction factor for an arbitrary distribution of pore sizes. A more rigorous mathematical treatment of the hydrodynamic interaction for general pore geometry is given by Johnson et al. (1987). These theories provide more realistic modeling of wave dispersion and attenuation in the high-frequency range where the acoustic wave frequency is much higher than the relaxation frequency. In the low- and medium-frequency range, however, these theories coincide with the Biot (1956a) theory. The frequency range (up to a few kHz) encountered in most seismic field experiments is well within the low- and medium-frequency range, thus, the simple Biot (1956a) theory should be sufficient to model the wave propagation encountered in these seismic experiments. Furthermore, the weak frame approximation of the Biot theory by Geerstma and Smit (1961) applies to all unlithified sediments and some sedimentary rocks (Turgut and Yamamoto, 1988; 1990).

Mavko and Nur (1975), Stoll (1980), Murphy et al. (1986), and White (1983) examined another type of hydrodynamic interaction, called squirt flow, resulting from a microscopic local flow near the contact points between grains. This type of hydrodynamic interaction can cause velocity dispersion and frequency-dependence attenuation in some rocks (Mavko and Nur, 1975; Murphy et al., 1986) but is of secondary importance in saturated sediments in the frequency range (up to 30 kHz) of interest in this paper (White, 1983; Stoll, 1980). Dvorkin and Nur (1993) proposed a unified theory that combines the Biot effect and the squirt flow effect. Although we do not include squirt flow effects in this paper, this unified theory may be useful when this transformation is extended to sedimentary rocks.

The validity of the Biot theory for acoustic wave propagation in saturated sediments has been shown by many authors from comparisons with experimental data. Using Hamilton's (1972) collection of acoustic velocity and attenuation in marine sediments in the frequency range 1 to 100 kHz, Stoll (1977), and Yamamoto and Turgut (1988) showed that the Biot theory predicts the acoustic attenuation in this frequency range. Gibson and Toksöz (1989) showed that the Biot theory predicts the ultrasonic (0.1 to 10 MHz) wave attenuation data in clays published by Hampton (1967). Turgut and Yamamoto (1990) showed that the velocity dispersion and attenuation of acoustic waves (1 to 30 kHz)

measured in a beach sand followed the prediction of Biot's theory.

Based on the above background, we consider that the Biot low-frequency theory should adequately model the type of sediments (alluvial clays and sands) in the frequency range (1 to 10 kHz) encountered in our experiments; thus, we selected the theory as our sediment model. The Biot's formula and the useful approximation given by Geerstma and Smit (1961) are summarized in Appendix A.

Shear modulus and porosity of sediments

The shear modulus is one of the most important descriptive parameters of a sediment. It is a particularly sensitive indicator of the skeletal structure and the shear strength. However, the shear modulus cannot be determined directly from compressional wave velocity measurements. For unlithified sediments there is an unique empirical relation between the shear modulus and the porosity. This empirical relationship combined with the compressional-wave velocity measurements will enable us to estimate the shear modulus and the porosity.

A wealth of experimental data on the relations between the shear modulus and the depositional state of unlithified sediments has been accumulated. For a summary of these works, readers are referred to Richart et al. (1970), Ishihara (1976), Bryan and Stoll (1988), Yamamoto et al. (1989). The data indicate that the shear modulus μ is a unique function of porosity β and the confining effective stress σ given by an empirical relation of the form (Yamamoto et al., 1989)

$$\mu = A \left(\frac{1 - \beta}{\beta} \right)^{1.12} \sigma^{0.5}, \quad (1)$$

where $A = 1.835 \times 10^5 (P_a)^{0.5}$. This relationship holds for unlithified sediments regardless of the sediment type. This empirical relation is based on both laboratory and field seismic data from unlithified sandy, silty, or mixed-clayey sediments (β ranges from 0.25 to 0.70). The alluvial sediments in Tokyo Bay considered in this paper have porosity in the 0.35–0.75 range; thus, the sediments are compatible with this relation.

It is interesting to note that the elastic theory of face-centered spheres predicts μ is proportional to the cubic root of σ (White, 1983). The confining effective stress σ is the average of the vertical effective stress, or the effective overburden pressure σ_z , and the horizontal effective stresses σ_x and σ_y . The confining effective stress at a given depth of burial z in the sediment strata under normal consolidation conditions is given as,

$$\begin{aligned} \sigma &= 1/3(\sigma_x + \sigma_y + \sigma_z) \\ &= \int_0^z \frac{1 + 2K_0}{3} (\rho_r - \rho_f) g(1 - \beta) dz, \end{aligned} \quad (2)$$

where g is the acceleration of gravity, ρ_r is the density of the grain, ρ_f is the density of water, and K_0 is the coefficient of earth pressure at rest and is related to the internal friction angle ϕ_0 of the sediment strata (Ishihara, 1976), as $K_0 = 1 - \sin \phi_0$. Since ϕ_0 in a natural sediment is about 30 degrees, K_0 is about 0.5. Hathaway et al. (1979) reported

that the average value of ϕ_0 from several hundred sediment cores collected from the continental shelf of the eastern USA is also about 30 degrees. Therefore, we use $K_0 = 0.5$ in the calculation.

For cohesive sediments (clays and silts), an empirical relationship has been found between the shear modulus μ and the shear strength u by Hara et al. (1974) as,

$$u = \mu/516. \quad (3)$$

This equation may underestimate the shear strength of cohesionless sediments (sands).

Empirical relationships found for lithified sediments (Han et al., 1986) may be incorporated with the Biot model to transform velocity images into porosity and shear modulus images; however, such exercises will be left for future studies.

Transformation of velocity images into material property images

To facilitate the transformation procedure described in this section, we compare the Biot theory prediction with the phase velocity and attenuation data measured by Turgut and Yamamoto (1990) in a marine sand in Figure 2a and 2b. Figure 2a shows phase velocity versus log frequency for three curves. The solid line represents Biot theory as described in Appendix A [equation (A-1)]. In the calculation, we assumed $\beta = 0.45$, $\mu = 2.0 \times 10^8$ Pa, $\alpha = 0.25$, and $k_s = 17.5$ darcy. The β , μ , and k_s values are measured directly by laboratory tests. This sediment is classified as a medium grain (0.25 mm) carbonate sand commonly found on Florida beaches. The line marked by asterisks (*) represents direct

measurements of compressional velocity in the experiment. The line marked by circles (○) indicates phase velocity calculated from measured attenuation using the Kramers-Kroning relationship (Bourbié et al., 1987). This relation is given as,

$$Q^{-1} = \frac{f}{V} \frac{dV}{df}, \quad (4)$$

where Q^{-1} = intrinsic attenuation, V = phase velocity, and f = frequency.

The measured velocity shows a higher slope than the Biot theory prediction; however, the point of maximum slope, which indicates the relaxation frequency needed for the permeability calculation in a following section, is at approximately the same frequency of 3.8 kHz and is marked by the dashed line. Also, the low-frequency and high-frequency ends match the theory well. The Kramers-Kroning estimate of velocity does better at lower frequencies. The asymptotes, V_0 and V_∞ , are needed in the following section.

Figure 2b shows intrinsic attenuation Q^{-1} versus log frequency for three curves. The solid line is Biot theory calculated from equation (A-10) and the previously mentioned constants. The circles (○) are direct measurements of attenuation, and the asterisks (*) represent attenuation as calculated from the velocity data using the Kramers-Kroning relationship. The peak of the attenuation curve also represents the relaxation frequency, which again is at 3.8 kHz.

Porosity and shear property images.—Porosity estimates can be obtained from the measured compressional wave velocity V_p at low frequencies if one assumes the low-

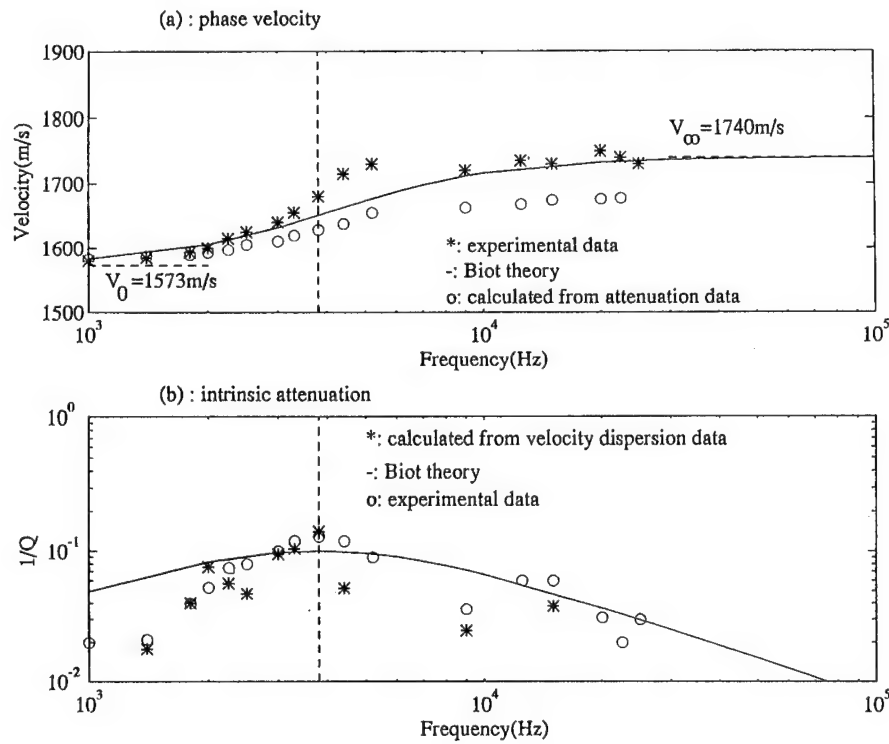


FIG. 2. (a) Phase velocity versus log frequency in Florida beach sands. (b) Intrinsic attenuation versus log frequency in Florida beach sands.

frequency velocity V_0 in equation (A-8) may be replaced with V_p . The velocity V_0 represents the Geertsma and Smit (1961) limiting case as f approaches zero. Figure 2a indicates V_0 is very near $V(1 \text{ kHz})$ in marine sands; therefore, the velocity images measured at 1 kHz were used for the porosity transformation.

Using the measured low-frequency velocity V_p , one can estimate the porosity β from equation (A-7) as,

$$\beta = \frac{K_f(K_r - K)}{(K_r - K_f)(K - K_s)}, \quad (5)$$

where

$$K = H - \frac{3}{4}\mu = \rho(V_0^2 - V_s^2), \quad (6)$$

and

$$V_s = (\mu/\rho)^{0.5}. \quad (7)$$

Here, K_f is the bulk modulus of water, K_r is the bulk modulus of the sediment grains, K_s is the bulk modulus of the sediment framework, H is the Biot's elastic modulus given in Appendix A [equation (A-4)], ρ = bulk density of the sediment, and V_s is the shear-wave velocity. This equation assumes K_r is more than an order of magnitude larger than K_s . Numerically, the porosity β and the shear modulus μ were determined iteratively from the velocity V_p using Equations (1), (2), (3), (5), (6), and (7). Only a few iterations were needed.

The approximation of V_0 by the measured velocity V_p at 1 kHz in equation (6) may introduce an error in the porosity calculation. For the medium sand in Figure 2a, the theoretical phase velocity at 1 kHz is 1580 m/s; whereas, V_0 from equation (A-8) is 1573 m/s, which is less than a one percent error. The porosity estimate by equation (5) using the two velocity values are 0.445 and 0.450, respectively, which is a 0.5 percent error. Therefore, the assumption $V_0 = V_p$ at 1 kHz may be reasonable for most sediments (clays, silts, and fine and medium sands). For coarser and more permeable sediments (coarse sands, pebbles, and gravel), this approximation may overestimate the porosity value.

The relaxation frequency should be less for more permeable sediments, so the slope of the velocity curve increases at lower frequencies. The difference between V_0 and $V(1 \text{ kHz})$ should become large for more permeable sediments, introducing some error in such cases.

Permeability image.—The permeability k_s may be determined from the value of the relaxation frequency f_r , where the intrinsic attenuation is maximum and the slope of the V versus log frequency curve is maximum. By setting the derivative of equation (A-10) equal to zero, we find f_r as,

$$f_r = \frac{\rho\eta}{2\pi(\rho m - \rho_f^2)k_s} \frac{V_0}{V_\infty}, \quad (8)$$

where ρ is the bulk density of the sediment, η is the viscosity of the pore fluid, m is the inertia density of the rock grain given in Appendix A [equation (A-2)], and V_∞ is the high-frequency limit of the velocity given by equation (A-9).

For the Florida beach sand in Figure 2, the relaxation frequency measured from the experimental attenuation data

is the same as that from the velocity data and equal to 3.8 kHz. The high-frequency velocities (measured at 30 kHz) are 1725 m/s from the direct velocity data and 1700 m/s as converted from the attenuation data. The estimated permeability values using equation (8) are 16.7 darcys from the velocity data and 16.9 darcys from the attenuation data. The direct measurement of permeability from laboratory testing was 17.5 darcys; therefore, the approximate error between measured permeability and estimated permeability is about 4 percent.

The measured attenuation data show a main peak at 3.8 kHz and a second peak at 15 kHz. The second peak may be a result of a possible bimodal pore size distribution in the sediment that can be modeled using arbitrary pore size distribution models (Yamamoto and Turgut, 1988; Johnson et al., 1987). However, the effect of higher modes in pore size distribution on the permeability is negligible (Yamamoto and Turgut, 1988). We think that the second peak in the attenuation data is a result of experimental errors. Attenuation is much more difficult to measure compared to velocity because the effect of scattering as a result of volume fluctuation in the sediment is usually significant in the 1–30 kHz frequency range (Rogers et al., 1993). Therefore, we use velocity instead of attenuation to extract material properties.

RESULTS

Beamforming of common source data

The digital data from each hydrophone are averaged (over multiple sequence lengths) and cross-correlated with the source signal to compute the waveform. Figure 3 shows a typical common source gather. The source is located 22 m below the ground surface in well 20, and the hydrophone array is located in well 15. The wells are separated by 122 m. The total wavefield is complicated by multiple ray arrivals and tube waves. Although the pulse compression using a long sequence (4095 cycles) of a pseudorandom binary code effectively reduces much of the very strong background noise, some noise energy is still visible in the common source data. To identify the multiple ray arrivals and tube waves, we performed a beamforming transformation.

Beamforming stacks adjacent waveforms at varying angles to separate the arrivals. The procedure is described briefly in Appendix B. Beamforming results, using the five hydrophones located between 17- and 21-m below surface, are shown in Figure 4. This figure is a color contour image of the combined waveforms given in angle of incidence versus traveltimes. Negative angles represent ray incidence at the receiver array from below horizontal. Wave amplitudes are shown in a linear scale with red being the maximum and blue being zero. The large hydrophone spacing of 1 m, as compared to the wavelength of approximately 1.5 m, causes spatial aliasing for angles beyond ± 60 degrees and marginal directional resolution. Nonetheless, each of the multiple ray arrivals are separated and some interpretation may be possible. The direct (D) arrival at 80 ms from 0 degrees, the surface-reflected (SR) arrival at 84 ms from 10–20 degrees, the surface-reflected-bottom-reflected (SRBR) arrival at 98 ms from -50 degrees, the surface-reflected-bottom-reflected-surface-reflected (SRBRSR) arrival at 100 ms from $+40$ degrees, and a possible tube wave

(T) at 86 ms can be identified in Figure 4. Many other arrivals are shown in the beamforming diagram, but their origins are not clear.

Seismic velocity images

A damped least-squares-inversion algorithm developed by Bregman et al. (1989) was used to image the compressional-wave velocities. Typically, 48×48 or 24×24 combinations of source-receiver locations were used in the crosswell experiments. Accordingly, the velocity image is represented by a grid of 48×48 or 24×24 unknown grid points to be determined by inversion. Iterative inversions continued until the differences in first-arrival times between the data and the model became less than a fraction of a millisecond for all rays.

Well 11 is located approximately half way between wells 12 and 15. Comparisons among velocity images for cross-sections 15-12, 15-11, and 11-12 provide an opportunity to check the tomographic results. Various geotechnical tests performed on cores and boreholes are used to further verify the tomographic images. Sediment stratigraphs obtained from boring of wells are also used to verify the tomographic images.

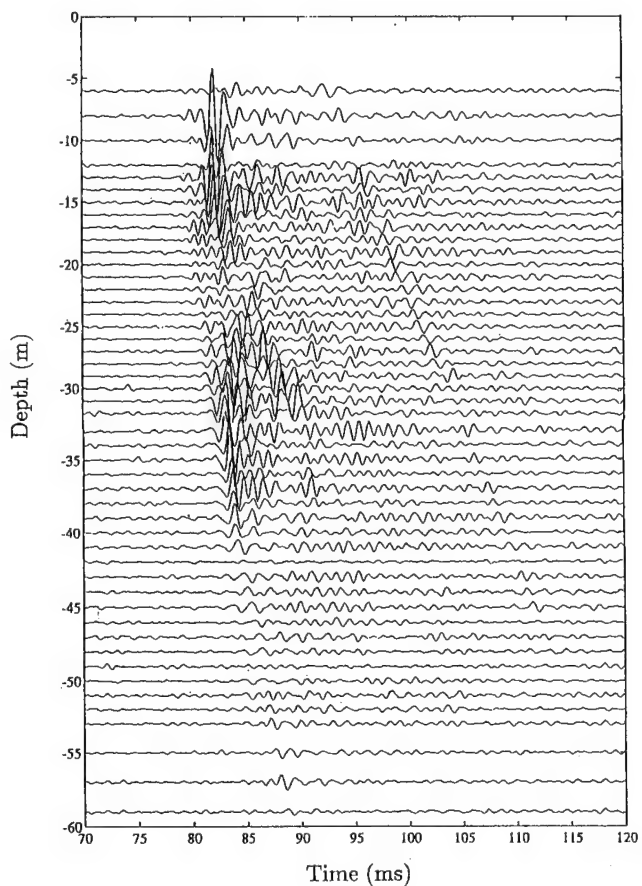


FIG. 3. Common source gather, Tokyo Bay experiment 20-15. The source is 22 m deep in hole 20; the receivers are 122 m away in hole 15.

The compressional-wave velocity images of cross-sections 15-11 and 11-12 are shown side-by-side in Figure 5 so that the continuity of the total cross-section 15-11-12 may be examined. This figure shows color contour images of compressional wave velocity in depth (m) versus cross-sectional width (m). A 2:1 vertical exaggeration has been added to enhance the stratigraphy. Cross-sectional widths are 136 m for 15-11 and 116 m for 11-12. Both sections are 60 m deep. The color intensity scale shown at the bottom ranges from 1450 (m/s) to 1650 (m/s). Also shown on both sides of each velocity image are tick marks indicating the source and receiver locations used for traveltime measurements and the sediment stratigraphs. The legend for the stratigraphs is given at the bottom of the figure. The two velocity images are continuous at well-11, which adds to the credibility of the images. The geology revealed from the velocity images is characterized roughly by a shallow 5-m acoustically attenuating slag layer and a thick, fast (1620 m/s) sand layer below 40 m. Between these two units are thin layers and lenses of medium velocity (1560 m/s) sandy clays floating in a thick body of low velocity (1480 m/s) clay. The seismic images are spatially averaged over the dominant seismic wavelength; however, they generally agree with the stratigraphs. A spatial resolution of 1.5 m is expected in these velocity images because a carrier frequency of 1 kHz was used in the experiments. Sediment cores show that the upper and lower clay layers contain much more sand (up to 50 percent by weight) and have higher densities than does the middle clay layer (a few percent by weight of sand). This tendency agrees with the velocity images, which show a 10- to 20-m thick low velocity layer at mid-depth. The consolidation process causes density to first increase near the free surface. This effect may be seen from the velocity images as higher density sediments tend to have higher compressional velocities.

The velocity image made at 1 kHz for cross-section 15-12, which spans across a distance of 247 m is shown in Figure 6. This was by far the longest crosswell distance and was the measurable limit at 1 kHz since the data quality was poor because of a low signal-to-noise ratio. Nevertheless, a fair quality image was obtained. This image is a color contour of compressional wave velocity in cross-sectional width versus depth. Again, there is a 2:1 vertical exaggeration in the figure. The color intensity scale is the same as for Figure 5. The stratigraphic sections for wells 15 and 12 are shown on the border as are the tick marks for the source and receiver positions. More source and receiver positions were attempted than are shown in Figure 5, but many of the time series had to be discarded because of noise. Comparisons to the stratigraphic sections indicate that this inversion shows a sand layer between 30 and 40 m depth at well 15 and a fast sand layer below 45 m. The inversion shows a sand layer from 35-40 m at hole 12, and again, a faster layer near 50 m depth. The slag layer is assumed to be above the last receiver where the signal can be distinguished from noise; however, in this case the signal loss from 5-10 m at hole 12 is more likely to be a very attenuating sand layer. Figure 6 is similar to Figure 5 in overall geologic structure, especially near hole 12.

Material property images

In this section, we show the results of transforming the compressional wave images into estimates of the material properties, porosity, and shear strength through the procedures presented in the preceding section. The results were compared with the stratigraphs and the standard penetration tests (SPT) performed at the wells and with the porosity and shear strength measurements made from cores.

Porosity images.—The porosity images transformed from the compressional wave velocities for cross-sections 15-11-12 are shown in Figure 7. Again, the hatch marks for the source and receiver locations and the stratigraphs taken from the wells are shown at both ends of the images. The tomographically measured images are spatially averaged versions of the real porosity images; however, comparisons with the stratigraphs indicate that much of the essential structure is revealed. The core tests at well 11 gave the range of porosity of clays as 0.50 to 0.75, with the average being 0.67. The porosity of sands could not be measured because undisturbed cores of sands could not be recovered. Nonetheless, the sand in the bottom layer is packed and has an N -value over 50 from the standard penetration test (SPT); thus, the porosity is estimated to be between 0.30 and 0.40 (e.g., Terzaghi and Peck, 1960).

Shear-strength images.—The shear-strength images of cross-sections 15-11-12 transformed from the compressional-

wave velocities using the procedure described in the preceding section are shown in Figure 8. The shear-strength stratigraphs measured by the SPT tests are shown at the edges of the shear-strength images for comparisons.

The SPT is defined as the number (N) of blows from a 140 lb hammer dropped through a height of 30 inches that are required to drive a 2-inch-diameter sampling pipe into the sediments a distance of 1 ft (Terzaghi and Peck, 1960). An empirical relation (Ohsaki and Iwasaki, 1973) gives the relation between the shear modulus μ and the blow count N as,

$$\mu = 11.9N^{0.8}(\text{MPa}). \quad (9)$$

The shear moduli are converted into the shear strength through the empirical equation (3). The SPT is a crude estimate of shear strength but is useful as an indicator of the relative shear strength between layers.

The shear-strength images basically show a two-layer structure; a weak (60–120 kPa) layer overlaying a strong (180–300 kPa) bottom layer. The SPT stratigraphs basically agree with the tomographically measured images. The tomographic images predict slightly higher shear strengths for the clay layers and slightly lower values for the sand layers. In the shear-strength transformation, we assumed that the consolidation of the clay layers has been completed, or the normal consolidation condition has been achieved. However, the consolidation is still going on as evidenced by subsidence of the island; therefore, the tomographic images show a slightly higher shear strength than the SPT shear

Cross-section 20-15

Beamforming

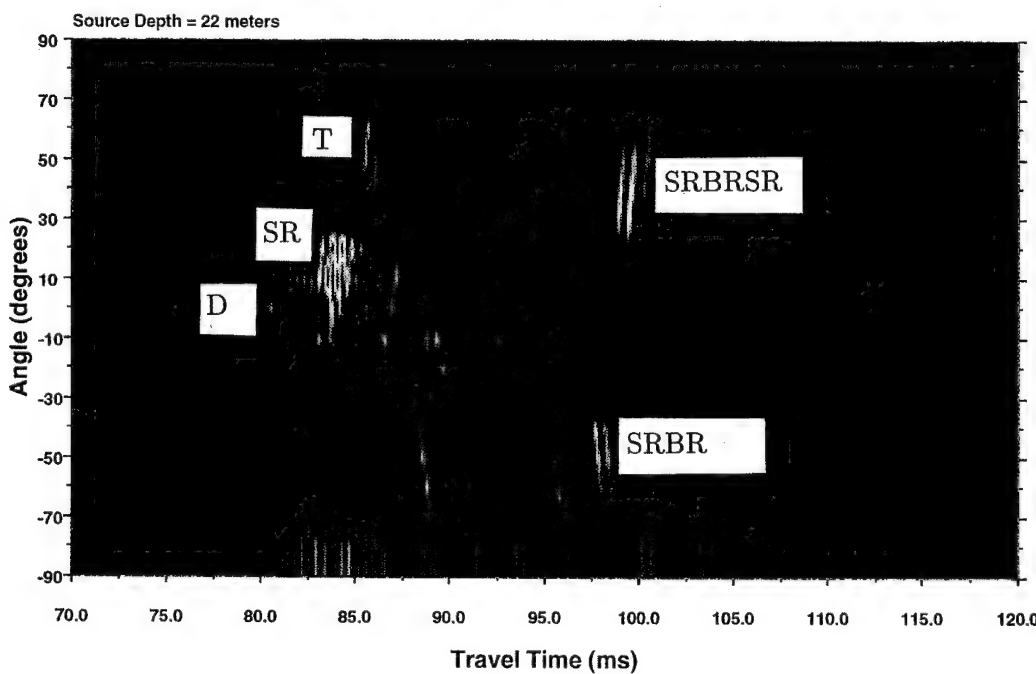


FIG. 4. Beamforming results from Tokyo Bay experiment 20-15. Source depth is 22 m, and receiver depths vary from 17 to 21 m.

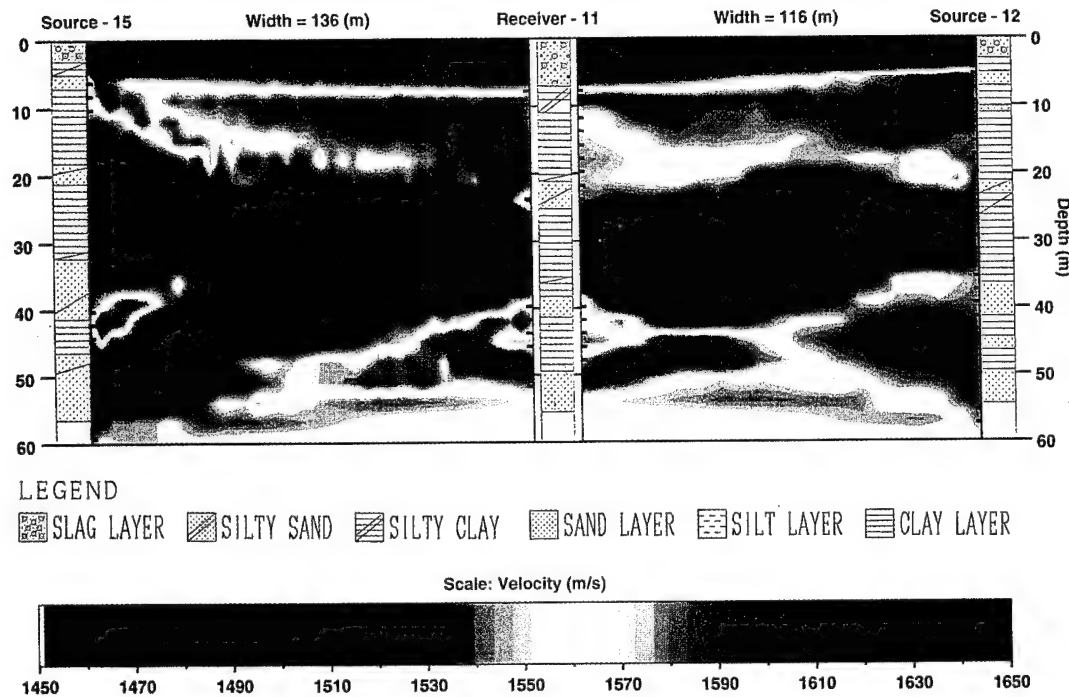


FIG. 5. Compressional-wave velocity results for cross-sections 15-11 and 11-12 (cross-sectional widths of 136 m and 116 m, respectively) and borehole stratigraphy. There is a 2:1 vertical exaggeration.

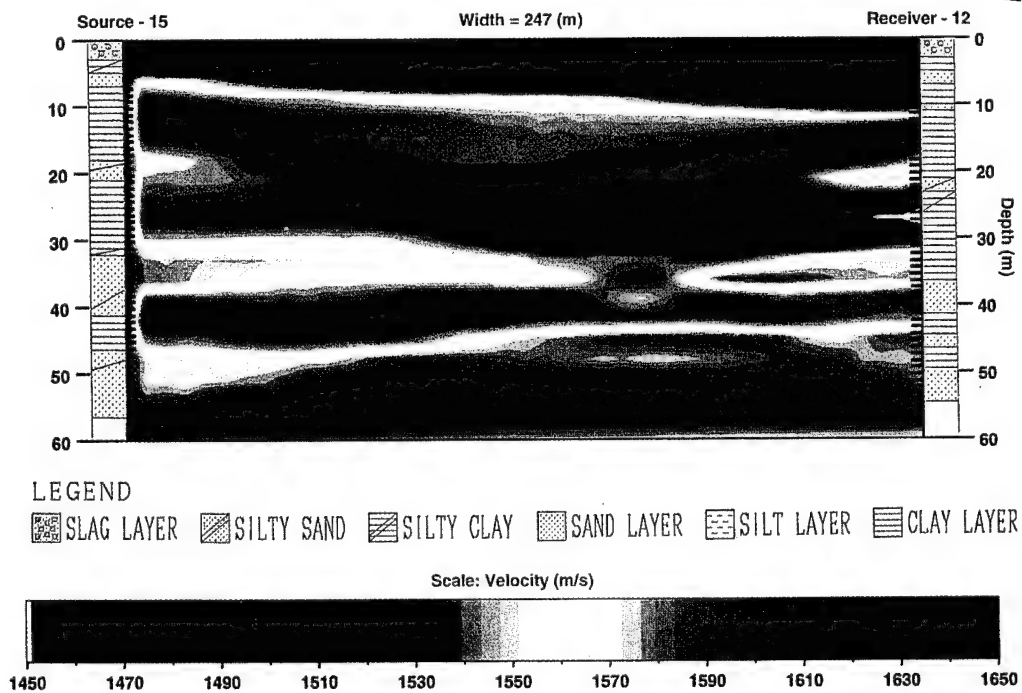


FIG. 6. Compressional-wave velocity result for cross-section 15-12 (247-m cross-sectional width) and borehole stratigraphy. There is a 2:1 vertical exaggeration.

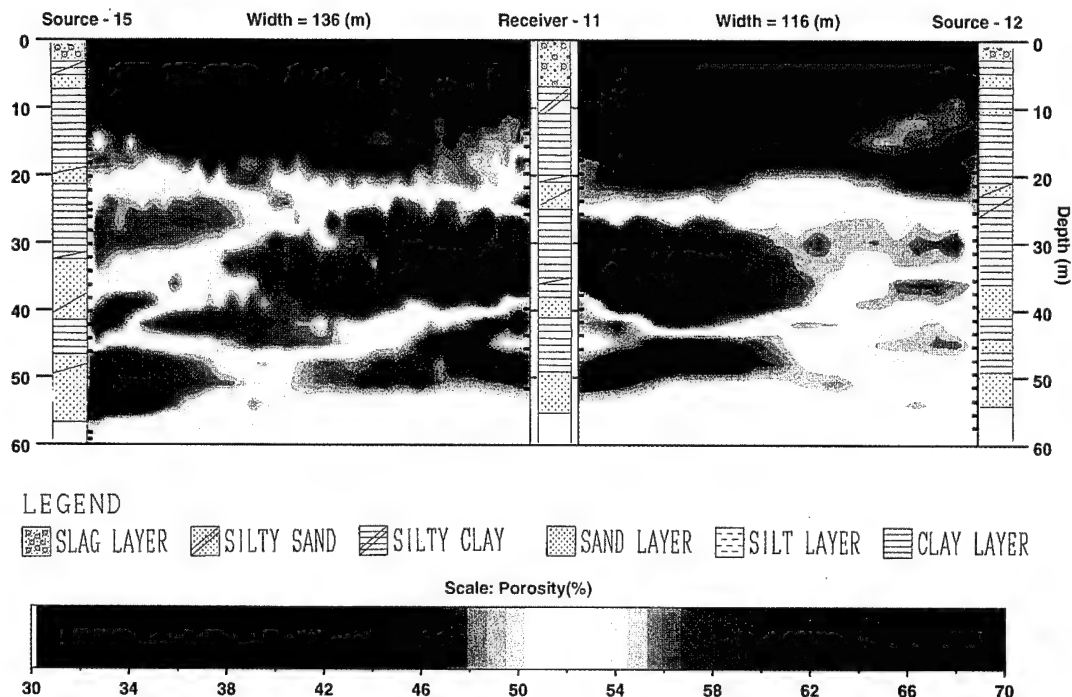


FIG. 7. Porosity results for cross-sections 15-11 and 11-12 (cross-sectional widths of 136 m and 116 m, respectively) and borehole stratigraphy with a 2:1 vertical exaggeration.

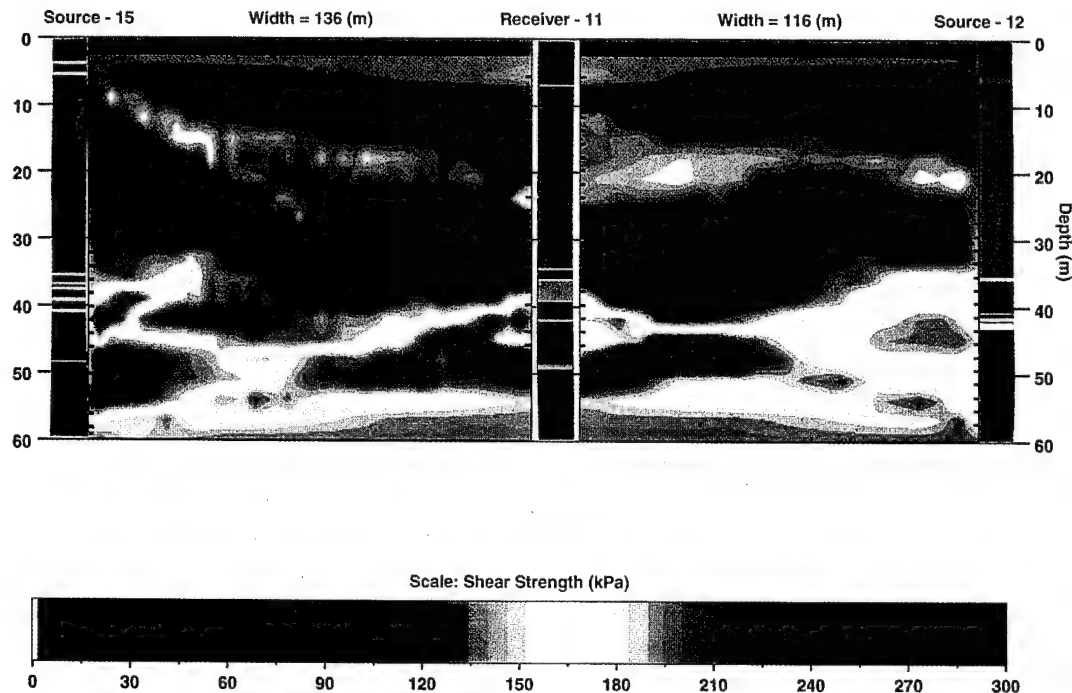


FIG. 8. Shear strength results for cross-sections 15-11 and 11-12 (cross-sectional widths of 136 m and 116 m, respectively) with a 2:1 vertical exaggeration. Borehole shear strength as transformed from measured N values are also shown.

strength for clays. Actually this difference is a good indicator of the degree of consolidation and may be used to predict the future subsidence of the island. The empirical equation (3) obtained from clayey sediments (Hara et al., 1974) probably underestimates the shear strength of sandy sediments. Nonetheless, the shear-strength images from compressional wave images agreed quantitatively with the SPT shear-strength stratigraphs.

Permeability images.—Permeability values are the most difficult information to obtain from velocity images because the velocities must be measured at many different frequencies. Consequently, we conducted tomographic experiments across the wells at 1, 3, 6, and 10 kHz. The differences in the velocities were not large enough to obtain consistent permeability values at this site. We plan to present a more definitive case of permeability tomography in a future paper (Yamamoto, et al., 1993).

DISCUSSION

In this section, we discuss the problems encountered in this study and possible future improvements.

Using a long sequence (4095 cycles) of pseudorandom code as a source signal helped increase the signal-to-noise ratio at high carrier frequencies (1–10 kHz); however, it took a long time (a few days by an IBM PC) to calculate arrival times by cross-correlation for a cross-section typically having 2500 source-receiver pairs. A multi-channel correlator would eliminate this problem and reduce the required amount of data to be recorded. The correlator would also provide a real-time display of arrival times for on-site interpretation of data.

To image the permeability, we need to have accurate velocity images for a wide range of frequencies. Obtaining a velocity image at a high frequency (say 10 kHz) across a long crosswell distance (120 m) is difficult. Development of a more powerful source, longer PRBS sequences, and a high-speed correlator may be needed to solve this problem.

We showed that the arrival times and approach angles of multiple rays can be determined using a beamforming technique; however, only the first-arrival times are used for inversion. Lack of sharp angle rays between wells separated by a long distance compared to the well depth severely limits the spatial resolution of images, as shown for cross-section 15-12 (247 m) in Figure 6. Development of a traveltime inversion capable of using multiple ray arrival times should improve the spatial resolution.

We used the Gassman (low-frequency Biot) model given in equation (A-8) and the normal consolidation condition for transforming a measured compressional-wave velocity image into a porosity image and a shear-strength image. The porosity images agreed with cores fairly well, but overestimated shear strength of alluvial clays in the shear-strength images were found as compared to the Standard Penetration Tests (SPT). This indicates that the consolidation of the clays is still in progress; i.e., not all of the grains of the clays are in contact. Periodic imaging of porosity should be made to monitor the consolidation process. The underconsolidated condition should be incorporated in the transformation process to improve the shear strength estimation.

Porosity, shear modulus, and permeability should be determined simultaneously from the Biot equation (A-1) instead of from the approximation equation (A-8), using velocity values measured at many different frequencies.

CONCLUSIONS

Large span (up to 250 m) crosswell acoustic tomography experiments were performed through an alluvial sediment strata under a very noisy iron foundry. Pulse compression of long sequences (4095 cycles) of pseudorandom binary codes at high carrier frequencies (1 to 10 kHz) as source signals produced high quality traveltime data. Beamforming of common source data identified the arrival times and approach angles of multiple rays and tube waves and further enhanced the signal-to-noise ratio. Inversion of first-arrival data using a damped least-squares method imaged the compressional-wave velocities at high spatial resolutions.

A procedure to transform velocity images into material property images of porosity, permeability, and shear strength was developed based on the Biot theory, the normal consolidation assumption, and an empirical relationship between porosity and shear modulus of sediments. This transformation algorithm was applied to the velocity images measured from the crosswell experiments.

The transformed porosity images agreed with the core data and stratigraphs. The shear-strength images of the alluvial clays were slightly higher than the shear strength data measured by the standard penetration test bores, indicating that the clay layers are still consolidating. The periodic measurements of porosity and shear-strength images could provide a means to accurately document the consolidation process and the subsidence of reclamations and man-made islands built on alluvial sediment strata.

The transformation of compressional-wave velocity to permeability was successful for a small source-receiver distance (1.7 m), but more experimental improvements are needed for long crosswell distances.

ACKNOWLEDGMENTS

This work was sponsored by Kawasaki Steel Corporation. The time for preparing this manuscript was supported by the Office of Naval Research Ocean Acoustic Program (Dr. M. Badiey). The authors are grateful for the associate editor, W. S. Harlan, and the reviewers for constructive comments and their encouragement to revise the paper.

REFERENCES

- Biot, M. A., 1956a, Theory of propagation of elastic waves in fluid-saturated porous solid. I. Low-frequency range: *J. Acoust. Soc. Am.*, **28**, 168–178.
- , 1956b, Theory of propagation of elastic waves in a fluid-saturated porous solid. II. Higher frequency range: *J. Acoust. Soc. Am.*, **28**, 179–191.
- Bourbié, T., Coussy, O., and Zinszner, B., 1987, *Acoustics of porous media*: Gulf Publishing Co.
- Bregman, N. D., Bailey, R. C., and Chapman, C. H., 1989, Crosshole seismic tomography: *Geophysics*, **54**, 200–215.
- Bryan, G. M., and Stoll, R. D., 1988, The dynamic shear modulus of marine sediments: *J. Acoust. Soc. Am.*, **83**, 2159–2164.
- Dvorkin, J., and Nur, A., 1993, Dynamic poroelasticity: A unified model with the squirt and the Biot mechanism: *Geophysics*, **58**, 524–532.
- Gassmann, F., 1951, Über die Elastizität poröser Medien: *Vierteljahrsschrift der Naturforschenden Gesellschaft in Zürich*, **96**, 1–23.

Geerstma, J., and Smit, D. C., 1961, Some aspects of elastic wave propagation in fluid-saturated porous solids: *Geophysics*, **26**, 169–181.

Gibson, R. L., and Toksöz, M. N., 1989, Viscous attenuation of acoustic waves in suspensions: *J. Acoust. Soc. Am.*, **85**, 1925–1934.

Hamilton, E. L., 1972, Compressional-wave attenuation in marine sediments: *Geophysics*, **37**, 620–646.

— L. D., 1967, Acoustic properties of sediments: *J. Acoust. Soc. Am.*, **42**, 880–890.

Han, D., Nur, A., and Morgan, D., 1986, Effects of porosity and clay content on wave velocities in sandstones: *Geophysics*, **51**, 2093–2107.

Hara, A., Ohata, T., Niwa, M., Tanaka, S., and Banno, T., 1974, Shear modulus and shear strength of cohesive soils: *Soils and foundations*, **11**, 113–119.

Hathaway, J. C., Poag, C. W., Valentine, P. C., Miller, R. E., Schultz, D. M., Manheim, F. T., Kohout, F. A., Bothner, M. H., and Sangrey, D. A., 1979, U.S. Geological Survey core drilling on the Atlantic Shelf: *Science*, **206**, 515–524.

Ishihara, K., 1976, Foundation of soil dynamics (in Japanese): Kajima Press.

Johnson, D. L., Koplic, J., and Dashen, R., 1987, Theory of dynamic permeability and tortuosity in fluid-saturated porous media: *J. Fluid Mech.*, **176**, 379–402.

Johnson, D. L., and Sen, P. N., (edited), 1984, Physics and chemistry of porous media: American Institute of Physics.

Mavko, G., and Nur, A., 1975, Melt squirt in asthenosphere: *J. Geophys. Res.*, **80**, 1444–1448.

Murphy, W. F., Winkler, K. W., and Kleinberg, R. L., 1986, Acoustic relaxation in sedimentary rocks: Dependence on grain contacts and fluid saturation: *Geophysics*, **51**, 757–766.

Nur, A., and Wang, Z., (edited) 1989, Seismic and acoustic velocities in reservoir rocks: Vol. 1, Experimental Studies: *Geophysics Reprint Series No. 10*, Soc. Expl. Geophys.

Ohsaki, Y., and Iwasaki, R., 1973, On dynamic shear moduli and Poisson's ratios of soil deposits: *Soils and foundations*, **13**, 61–73.

Richart, F. E., Hall, J. R., and Wood, R. D., 1970, Vibrations of soils and foundations: Prentice-Hall, Inc.

Rogers, A. K., Yamamoto, T., and Carey, W., 1993, Experimental investigation of sediment effect on acoustic wave propagation in the shallow ocean: *J. Acous. Soc. Am.*, **93**, 1747–1761.

Stoll, R. D., 1977, Acoustic waves in ocean sediments: *Geophysics*, **42**, 715–725.

— 1980, Theoretical aspects of sound transmission in marine sediments: *J. Acoust. Soc. Am.*, **68**, 1341–1350.

Terzaghi, K., and Peck, R. B., 1960, Soil mechanics in engineering practice: John Wiley & Sons, Inc.

Turgut, A., and Yamamoto, T., 1988, Synthetic seismograms for marine sediments and determination of porosity and permeability: *Geophysics*, **53**, 1056–1067.

— 1990, Measurements of acoustic wave velocities and attenuation in marine sediments: *J. Acoust. Soc. Am.*, **87**, 2376–2383.

White, J. E., 1983, Underground sound: Application of seismic waves: Elsevier Science Publ.

Wood, A. B., 1941, A textbook of sound: Bell Publisher.

Yamamoto, T., Nye, T., Kuru, M., Sakaki, T., Ishihara, K., and Okumura, J., 1993, Measurements of porosity and permeability of the Florida limestone aquifer using a crosswell acoustic tomography: 63rd Ann. Internat. Mtg., Soc. Expl. Geophys., Expanded Abstracts, 378–381.

Yamamoto, T., Trevor, M., Badiey, M., and Turgut, A., 1989, Seabed porosity and shear modulus inversion using surface gravity (water) wave-induced seabed motion: *Geophys. J. Int.*, **98**, 173–182.

Yamamoto, T., and Turgut, A., 1988, Acoustic wave propagation through porous media with arbitrary pore size distributions: *J. Acoust. Soc. Am.*, **83**, 1744–1751.

APPENDIX A

BIOT THEORY

For unlithified saturated sediments, the compressional-wave velocity of sediment is given, based on the Biot (1956a) theory following Yamamoto and Turgut (1988) and Turgut and Yamamoto (1990), as

$$V^2 = Re \left[\frac{Hm' + Mp - 2C\rho_f}{\rho m' - \rho_f^2} \right], \quad (A-1)$$

where

$$m' = m - i \frac{\eta}{k_s \omega}; \quad m = \frac{(1 + \alpha)\rho_f}{\beta}, \quad (A-2)$$

$$\rho = \rho_r(1 - \beta) + \rho_f\beta, \quad (A-3)$$

where β = porosity, ρ = bulk density of sediment, ρ_r = density of grain mineral, ρ_f = density of pore fluid, α = added mass coefficient of grain, η = viscosity of pore fluid, k_s = intrinsic permeability of sediment, and ω = angular frequency.

H , C , and M are the Biot's elastic moduli of sediment and are given as,

$$H = (K_r - K_s)^2 / (D_r - K_s) + K_s + 4/3\mu \quad (A-4)$$

$$C = K_r(K_r - K_s) / (D_r - K_s) \quad (A-5)$$

$$M = K_r^2 / (D_r - K_s) \quad (A-6)$$

$$D_r = K_r[1 + \beta(K_r/K_f - 1)], \quad (A-7)$$

where K_f = bulk modulus of water ($= 2.3 \times 10^9$ Pa is used in calculation), K_r = bulk modulus of grain ($= 3.6 \times 10^9$ Pa is used in calculation); μ = dynamic shear modulus of frame, K_s = bulk modulus of frame $= [2n/(1 - 2n) + \frac{2}{3}]\mu$; n = Poisson's ratio of frame ($= 0.3$ is used in calculation).

The limiting cases of equation (A-1) are given by Geerstma and Smit (1961) as,

$$V_0^2 = H/\rho \quad (A-8)$$

for $\omega \rightarrow 0$ and

$$V_\infty^2 = (Hm + Mp - 2C\rho_f) / (\rho m - \rho_f^2). \quad (A-9)$$

for $\omega \rightarrow \infty$

Equation (A-8) is equivalent to Gassmann's (1951) equation. The intrinsic attenuation is given by Geerstma and Smit (1961) as,

$$Q^{-1} = \frac{V_\infty^2/V_0^2 - 1}{m_i/B + (B/m_i)(V_\infty^2/V_0^2)}, \quad (A-10)$$

where m_i is the imaginary part of m' and

$$B = (\rho m - \rho_f^2)/\rho. \quad (A-11)$$

APPENDIX B

BEAMFORMING

In the process of beamforming, adjacent receiver signals are summed with a given offset to find a preferred direction of incoming signal. The beamform is the sum

$$BF(t) = \sum_{j=1}^N Z(t + \Delta t_j), \quad (B-1)$$

where N is the number of signals to be combined. Each $Z(t)$ is the hydrophone signal amplitude, and $BF(t)$ is the beamformed signal. One of the signals is datum ($j = 1$), and the others are summed with various offsets Δt . Δt is equal to:

$$\Delta t = \frac{(d_j - d_1) \sin \theta}{c} \quad (B-2)$$

for a given angle θ . The depths of the receivers are given by d_j , and c is the average sound speed in the medium. The numerator of the above equation represents the extra distance the signal needs to travel to reach the various hydrophones. The distance changes as θ is varied from -90 degrees to $+90$ degrees. When $\theta = 0^\circ$ there is no offset at all. The beamform will show the strongest return when θ approaches the incidence angle of the signal. Multipath arrivals are easier to find and identify using this process.

Imaging the permeability structure of a limestone aquifer by crosswell acoustic tomography

Tokuo Yamamoto*, Thomas Nye*, and Murat Kuru*

GEOPHYSICS, VOL. 60, NO. 6 (NOVEMBER-DECEMBER 1995); P. 1634-1645, 12 FIGS., 1 TABLE.

Imaging the permeability structure of a limestone aquifer by crosswell acoustic tomography

Tokuo Yamamoto*, Thomas Nye*, and Murat Kuru*

ABSTRACT

A narrow-band pseudorandom binary sequence (PRBS) code was used to generate an acoustic pulse that approximates a single laser-like frequency. Measurements of crosswell tomography under a Florida limestone aquifer were made using four different PRBS frequencies: 250, 1 000, 2 000, and 3 000 Hz. Velocity images created by different PRBS frequencies showed different velocity values in the permeable layers but no velocity difference in the impermeable layers. For selected source-receiver pairs across these layers, crosswell experiments were conducted with more PRBS frequencies ranging from 200 to 5 000 Hz. Pulse propagation calculations using a layered elastic model indicate that the velocity-frequency dispersion is not a result of geometrical dispersion. The original procedure to extract porosity, permeability, and shear strength from seismic velocity images has been extended to the more general case of mixed lithified and unlithified sediments. The velocity-frequency dispersion data for the limestone layer were compared with the Biot theory and the Biot-squirt flow (BISQ) theory. The permeability value of the cavity-filled limestone layer inferred from BISQ theory is 200 darcies, whereas the average permeability measured from pumping tests was 331 darcies.

INTRODUCTION

This paper is a sequel to previous work (Yamamoto et al., 1994) where the authors introduce a procedure to extract the material properties of sediments such as porosity, permeability, and shear strength directly from the velocity images obtained from crosswell acoustic tomography experiments. High-resolution compressional wave velocity images within the alluvial sediment strata in Tokyo Bay were obtained

through a pulse compression technique using long (4095 bits) pseudorandom binary sequence (PRBS) codes with a carrier frequency ranging from 200 Hz to 10 kHz as the source signal. The Biot (1956) theory and an empirical relation (Yamamoto et al., 1989) between porosity and shear modulus were used to extract the porosity images and the shear strength images from the velocity images. Comparisons with cores and standard penetration tests supported the acoustically extracted images of porosity and shear strength. Evaluation of the acoustical extraction of the permeability image was not conclusive because of the lack of direct permeability measurement, and because no clear velocity-frequency dispersion was observed in the experimental frequency range in the alluvial sediments at this site.

This paper reports an example of the acoustic extraction of a permeability image of the Florida limestone aquifer as compared with direct permeability data from a pumping test. We have also extended the extraction procedures of porosity, permeability, and shear strength to the more general cases of mixed lithified and unlithified sediments in this paper. Extraction of material properties from measured seismic velocities of rocks necessarily relies on rock physical models that are still under active research. We adapt the unified Biot-squirt flow (BISQ) theory in Dvorkin et al. (1994) for extraction of permeability and the empirical model in Han et al. (1986) for extraction of porosity and shear strength. These models may or may not best represent the rock types and frequency range (200 to 5 000 Hz) encountered in our experiments. These theories and empirical models may change in time, but our proposed methodology can be adapted to new improvements in these models.

The determination of sediment permeability using acoustical methods is one of the most challenging geophysical problems and has important applications in the fields of petroleum and groundwater geology. Consequently, a large amount of theoretical and experimental research has been conducted on this subject. For reviews of these works, readers are referred to many textbooks and monographs;

Manuscript received by the Editor May 23, 1994; revised manuscript received January 20, 1995.

*Geo-Acoustic Laboratory, Rosenstiel School of Marine and Atmospheric Science, University of Miami, 4600 Rickenbacker Causeway, Miami, FL 33149.

© 1995 Society of Exploration Geophysicists. All rights reserved.

e.g., Toksöz and Johnston (1981), White (1983), Bourbié et al. (1987), Johnson and Sen (1983), Nur and Wang (1989), and Paillet and Cheng (1991).

As we will briefly review later, the acoustic determination of sediment permeability, however, has been limited to laboratory tests using rock specimens and downhole acoustic logging. No report has been made on the direct extraction of sediment permeability from the velocity images obtained from crosswell acoustic tomography methods or from multichannel seismic reflection methods. We present the results of a permeability determination from the crosswell acoustic tomography experiments performed at a Florida limestone aquifer as an example of such procedures in this paper.

Analogous to laser optics, an acoustic pulse with its energy concentrated near a certain frequency can be produced using a narrow-band (NB) pseudorandom binary sequence (PRBS) code as a source signal. Crosswell measurements through the same cross-section were repeated many times using different PRBS frequencies ranging from 200 to 5 000 Hz. The velocity-frequency dispersion data for various layers were compared with the Biot (1956) theory and the unified Biot-squirt flow (BISQ) theory in Dvorkin et al. (1994). The acoustically extracted permeability values were then compared with directly measured permeability data from pumping tests (Missimer and Assoc., 1992, Internal Report). The velocity images of the same cross-section were inverted from the first-arrival data of four different PRBS frequencies: 250 Hz, and 1, 2, and 3 kHz. The velocity within the permeable limestone formation varies with frequency, whereas the velocity within the impermeable formation remains unchanged with frequency. The velocity difference image between two different PRBS frequencies indicates the inhomogeneous structure of the permeability within the entire aquifer formation.

The effects of geometrical dispersion as a result of the geometry and the inhomogeneity of the sediment elasticity and attenuation were examined using the seismo-acoustic fast field algorithm for range independent environments (SAFARI) in Schmidt (1987).

ROCK PHYSICS TRANSFORMATION

The authors presented a brief review of rock physics and the transformation procedure from seismic velocity images to material property images for unlithified sediments in a recent paper (Yamamoto et al., 1994). The attempt to extend this transformation procedure to a more general case of mixed lithified and unlithified sediments is made in this paper.

Poroelastic theories

Biot (1956) introduced a theory of acoustic wave propagation through a fluid-saturated porous elastic medium. The viscous interaction between fluid and solid is governed by Darcy's law through fluid viscosity and the permeability of the porous medium. The inertia interaction between the fluid and the solid is treated by the potential flow theory through the added mass coefficient, which he calls the tortuosity in his original paper. According to the Biot theory, the velocity-frequency dispersion of the acoustic wave depends on the permeability. At the relaxation frequency, the slope of

the velocity versus log frequency curve, as well as the intrinsic attenuation, become maximum. The permeability is uniquely related to the relaxation frequency in this theory. Therefore, according to the Biot theory, one can determine the sediment permeability acoustically by measuring the velocity-frequency dispersion of the acoustic wave through the sediment. The Biot theory has been applied to determine the permeability of the unlithified sediments using the velocity-frequency dispersion. Gibson and Toksöz (1989) measured the permeability of kaolinite suspensions from the attenuation versus frequency data obtained from a high frequency (100–500 kHz) laboratory test in Hampton (1967). Turgut and Yamamoto (1990) measured the permeability of Florida beach sand from the velocity-frequency dispersion data obtained from a medium frequency (1–25 kHz) transmission test between a source and receiver separated a short distance of 1.7 m. These acoustic extractions of sediment permeability based on the Biot theory agreed reasonably well with the direct permeability measurements.

The Biot theory was incorporated in the computation of microseismograms generated in the borehole in Rosenbaum (1974). Using Rosenbaum's (1974) theory, Burns (1988) showed that the formation permeability can be measured from the acoustic logging waveform data taken in Williams et al. (1984). Active theoretical and experimental research activities continue in this subject [see Paillet and Cheng (1991) for a review of these works].

In Biot's model, pore fluid is forced to move with the oscillatory motion of the solid, and in the same direction as the solid, through viscous and inertia coupling. A different mechanism of fluid flow that is induced by the propagation of a seismic wave is associated with the squirting of pore fluid out of cracks as they are deformed by passing seismic waves. Mavko and Nur (1979) have shown that the squirt-flow mechanism results in much higher and realistic attenuation values in partially saturated rocks than those predicted by the Biot mechanism. Murphy et al. (1986) presented a micromechanical model of squirt-flow for acoustic attenuation and modulus dispersion in sedimentary materials. More theoretical and experimental works on the squirt-flow by many authors exist, and readers are referred to Johnson and Sen (1983) for a review of these works. This mechanism has been shown to be responsible for the measured seismic energy losses and velocity dispersion in sedimentary materials for both compressional wave and shear waves obtained from various mechanical tests performed on rock specimens in the laboratory (Tittmann, et al., 1984; Murphy et al., 1986; Wang and Nur, 1990). Dvorkin and Nur (1993) presented a unified model of the squirt and Biot mechanisms called the BISQ model which requires only one additional material property, called the squirt-flow length, in addition to the material properties needed for the Biot model. The BISQ model breaks down in the high frequency range. This problem was fixed in the latest version of the BISQ model presented in Dvorkin et al. (1994). They have shown that the Biot model alone cannot explain the velocity-frequency dispersion and attenuation of numerous sandstone specimens measured from the laboratory ultrasonic pulse transmission tests of Han et al. (1986) and Klimentos and McCann (1990), but the BISQ model can adequately model the data.

In this paper, we compare our velocity dispersion data with the Biot (1956) theory and BISQ theory in Dvorkin et al. (1994). It will be shown that the two theories coincide for unlithified sediments, whereas the BISQ theory better predicts the measured velocity dispersion of Florida limestones. The Biot model and BISQ model are summarized in Appendix B.

Partition criterion

First, we must distinguish whether the sediment is lithified or unlithified. The porosity of unlithified sediments ranges from 20% to over 90%. However, we know that the minimum porosity of unlithified sediment of natural origins is approximately 20%, which is found in glacial till (Terzaghi and Peck, 1960). On the other hand, the porosity of lithified sediments ranges from nearly zero to as high as over 40% (Gregory, 1976). In the porosity range from approximately 20 to 40%, sediments can be unlithified or lithified. For a given value of porosity and confining effective stress, however, a lithified sediment has higher values of shear and bulk moduli of the frame, and therefore higher values of seismic velocities, than an unlithified sediment. Furthermore, a lithified sediment with a porosity of 40% would have a higher seismic velocity than a unlithified sediment with a porosity of 20% under a relatively small overburden pressure (equivalent to less than a few hundred meters of burial depth which is our depth interest in this paper), according to the empirical relations in Han et al. (1986) and our unlithified sediment model (Yamamoto et al., 1994). Under larger confining stress, the effects of cementation on the seismic velocities decreases; thus either empirical equation gives approximately the same porosity estimates.

Therefore, our criterion of partition between lithified and unlithified sediments is: if we assume that the entire sediment formation is unlithified, and if we find a section of the formation having a porosity smaller than a transition porosity (20% or a reasonable estimate depending on the situation), then this section of the sediment is considered lithified.

Unlithified sediments

The porosity, permeability, and shear strength transformation procedures for unlithified sediments presented in Yamamoto et al. (1994) remain unchanged. The sediment is modeled by the Biot soft frame mode, the normal consolidation equation, and the empirical relationship between porosity, confining stress, and shear modulus. The key equations used in the transformation are given in Appendix A.

Lithified sediments

Efforts to derive empirical relationships between seismic velocities and material properties are also under active research. Han et al. (1986) measured the compressional wave velocity (V_P) and the shear wave velocity (V_S) of 75 sandstone samples having porosities varying from .02 to .32 and clay content varying between 0 and .50 using the ultrasonic frequency (.6–1 MHz) pulse transmission technique. The confining stress varied between 5 and 50 bars. We adopt their empirical relations as our lithified sediment model.

$$V_P = 4.80 - 7.20\beta - 1.80C \text{ (km/s)} \quad (1)$$

$$V_S = 2.80 - 4.60\beta - 1.45C \text{ (km/s)}, \quad (2)$$

where β is the porosity and C is the clay content. The numerical values of the model equations were obtained by extrapolation to shallow depths of burial of the order of 20 m (2 bars in confining pressure). To extract the porosity using equation (1) or (2), one needs an estimate of clay content. Since we have no information about the clay content of Florida limestone, we assumed a median value of Han's data, i.e., $C = .10$ in our transformation.

Our application of the Han et al. (1986) sandstone data to measured seismic velocities in Florida limestones introduces errors in our extraction results because the rock physics of limestones is different from that of sandstones. High quality limestone data were not found in open literature; however, we hope that these data will improve with time so that gaps in our assumptions can be filled. These new data can be adapted easily into the proposed extraction procedure. Nevertheless, we are encouraged by the plausibility of our extraction results.

Porosity.—The estimate of porosity is obtained from a measured compressional velocity V_P through equation (1) using $C = .10$. Since the empirical equation was obtained from laboratory tests using ultrasonic frequencies between .6 and 1 MHz, the velocity data are undoubtedly the high-frequency velocity in the velocity-frequency dispersion curve. Therefore, we should use V_P values at sufficiently high frequencies on the velocity-frequency dispersion. If low-frequency velocity data are used, the porosity estimate would overestimate the porosity, depending on the total velocity dispersion.

Shear strength.—Once the porosity has been determined from equation (1), the shear wave velocity V_S may be estimated using equation (2), assuming $C = .10$. The shear modulus will be given as

$$\mu = \rho(V_S)^2, \quad (3)$$

where ρ is the bulk density of the sediment given by

$$\rho = \rho_r(1 - \beta) + \rho_f\beta, \quad (4)$$

where ρ_r is the density of grain and ρ_f is the density of pore fluid. The shear strength may be estimated from the empirical equation in Ishihara (1976),

$$u = \mu/516. \quad (5)$$

Permeability.—The permeability estimate is obtained by fitting the velocity-frequency dispersion data by the Biot (1956) model or the BISQ model (Dvorkin et al., 1994). Because the Biot model can be given as a special case of the BISQ model, in Appendix B we give only a brief summary of the BISQ model. The spatial distribution of permeability requires a spatial distribution of the velocity-frequency dispersion. This will be attempted by creating a velocity difference image from two adjacent frequency velocity images.

EXPERIMENTS

The crosswell experiments were conducted in July, 1993 at the Westinghouse Florida limestone aquifer test site at Fort Myers, Florida. Some geology and hydraulic characteristics of this aquifer have been investigated by Missimer and Associates, Inc. (1992, Internal Report). The test site is covered with nine wells with various diameters (4 and 8 inches) and penetration depths (from 6 m to 72 m). These wells were used for pumping tests to measure the permeability of the aquifers. Figure 1 shows the stratigraphy of well LM-2061 and the values of the compressional and shear wave velocities of the layers used in the calculations for the pulse propagation. As shown in this figure, the geology of this site consists of four layers; from top to bottom, 6 m of medium permeability sand, 15 m of low permeability very soft dolosilt, 14 m of high permeability hard limestone, and 26 m of medium permeability partially lithified sandstone. Missimer and Associates, Inc. found the permeability of this

aquifer to be 331 darcies using the pump test. This very high permeability is assumed to be caused by cavities in the limestone layer that are of the order of 10 cm.

The crosswell tomography experimental system has been described in Yamamoto et al. (1994). We used well LM-2260 (8 inches in diameter, 32 m deep, and plastic casing to 22 m) as the source well and well LM-2061 (4 inches in diameter, 62 m deep, and plastic casing) as the receiver well. The distance between the two wells is 50.8 m. The water levels in the two wells were both approximately 3 m below ground level. The 24-channel hydrophone array with a 2 m interelement spacing was placed in well LM-2061. The 180 dB piezoelectric source is located in well LM-2260. The elevation of the source is varied by intervals of 1 m from the water level to the bottom of the well. To create a dense hydrophone spacing of 0.5 m, the elevation of the hydrophone array was changed four times.

The phase modulated pseudorandom binary sequence codes of a long (4095 bits) sequence are used for the source signal to propagate a narrow bandwidth (as narrow as 10% of carrier frequency) of acoustic pulse so that the velocity image is obtained approximately at a single frequency. If a single cycle of sine (or negative sine) is used for a bit of 1 (or 0), as commonly used in seismic data processing (Cunningham, 1978), the 3-dB bandwidth is 70% of the carrier frequency. In comparison, if four cycles of sine (or negative sine) is used for a bit of 1 (0), the bandwidth is reduced to 10% of the carrier frequency. One can further increase the number of cycles/bit to reduce the bandwidth. We used four-cycle PRBS as well as one-cycle PRBS to ensure the accuracy of the velocity-frequency dispersion measurements. Crosswell tomography measurements are made at carrier frequencies of 250 Hz, and 1, 2 and 3 kHz. For several source-receiver pairs, more carrier frequencies are used to measure the velocity-frequency dispersion. The signals received were sampled at four to 16 times the carrier frequencies, digitized, and stored at 12 bits of precision. Four ensembles of the data are averaged before cross-correlation with the input PRBS signals.

VELOCITY-FREQUENCY DISPERSION DATA AND MODEL PREDICTIONS

Velocity dispersion data

Examples of arriving waveforms, after cross-correlation, through the mud layer and the very permeable limestone layer at varying frequencies are shown in Figures 2 and 3, respectively. The source and receiver depths in the mud layer are 10 and 12.5 m; whereas in the limestone layer they are 27 m and 28.5 m. The mud layer and the limestone layer are shown in the stratigraphic column in Figure 1 and are also identifiable in the velocity images obtained from the traveltime inversion shown later in this paper (Figure 9). In Figures 2 and 3, the thin marks represent the onset of arrival, while the shorter thick mark represents the actual arrival time, which is $1/f_0$ after the onset of arrival, where f_0 is the carrier frequency of the PRBS code. This difference occurs because cross-correlation of perfectly coherent codes creates an arrival packet that is $2/f_0$ wide, with the precise arrival of its peak at $1/f_0$. The time data shown in Figures 2 and 3 were obtained using one cycle PRBS codes. Although

Depth	Unit	Description
0 - 6 m		Sand: compressional wave velocity $V_p=2000$ m/s shear wave velocity $V_s=667$ m/s
6 - 21 m		Dolosilt (very soft mud): compressional wave velocity $V_p=1600$ m/s shear wave velocity $V_s=533$ m/s
21 - 35 m		Limestone (average permeability = 331 darcies): compressional wave velocity $V_p=2300$ m/s shear wave velocity $V_s=767$ m/s
35 - 61 m		Sandstone (partially cemented): compressional wave velocity $V_p=2000$ m/s shear wave velocity $V_s=667$ m/s

FIG. 1. Stratigraphy of Westinghouse experimental site in Fort Myers, Fl used as input for the SAFARI model.

not shown here, essentially the same arrival times were obtained using four-cycle PRBS codes, indicating that the difference in the bandwidths of PRBS codes may be negligible in arrival time measurements in this experiment. The time data in Figure 3 for the permeable limestone layer show a strong velocity dispersion, whereas the time data in Figure 2 for the impermeable mud layer show no velocity dispersion. The time data shown in Figures 2 and 3 represent only two of the source-receiver pairs out of nearly 3 000 source-receiver pairs used in the tomographic inversion. The existence of velocity dispersion only in permeable layers will be shown more clearly when we show the velocity tomograms obtained from different PRBS carrier frequencies (Figure 9).

Geometrical dispersion

The velocity-frequency dispersion of acoustic waves can be caused by geometrical dispersion created by the layered structure of the earth or by intrinsic dispersion caused by the frequency-dependent velocity and attenuation of the material.

To check if the velocity dispersion observed in the permeable limestone layer shown in Figure 3 is or is not a result of geometrical dispersion, we conducted a numerical simulation of the pulse propagation using the "seismo-acoustic fast-field algorithm for range independent environment" (SAFARI) code in Schmidt (1987). The earth is modeled by the four layers of constant compressional and shear velocities given in Figure 1. The compressional-wave velocities in Figure 1 are the average values for the four layers obtained from the velocity tomogram obtained from crosswell measurements using 1 kHz PRBS, which is shown later (Figure 9b). The shear-wave velocity values are assumed to be equal to one-third of the measured compressional-wave velocities as often assumed in SAFARI modeling. Although these shear-wave velocity values are slightly different from the values obtained from the extracted shear moduli and porosities given in Table 1, the effect of shear-wave velocity on compressional velocity dispersion is negligible. Since no attenuation was measured during the experiments, some reasonable values of compressional-wave and shear-wave attenuation for the four layers are assumed. The effects of these attenuations on compressional-wave dispersion are also small. Intrinsic attenuation is 0.25 dB/m/kHz for compressional waves and 0.75 dB/m/kHz for shear waves for all layers.

The waveforms arriving at the receiver depth of 28.5 m, generated by a source at depth 27 m, are shown for a 1 kHz pulse and a 200 Hz pulse in Figure 4a and 4b. The first-arrival times are the same (22 ms) for the two frequencies. The source signal used in the calculation is a tapered two-cycle sine wave shown in the insets of Figure 4. The frequency content of the source signal is comparable to a two-cycle PRBS having a 3-dB bandwidth of approximately 30%. Based on these numerical simulations, we may conclude that no geometrical dispersion is found in the acoustic pulse

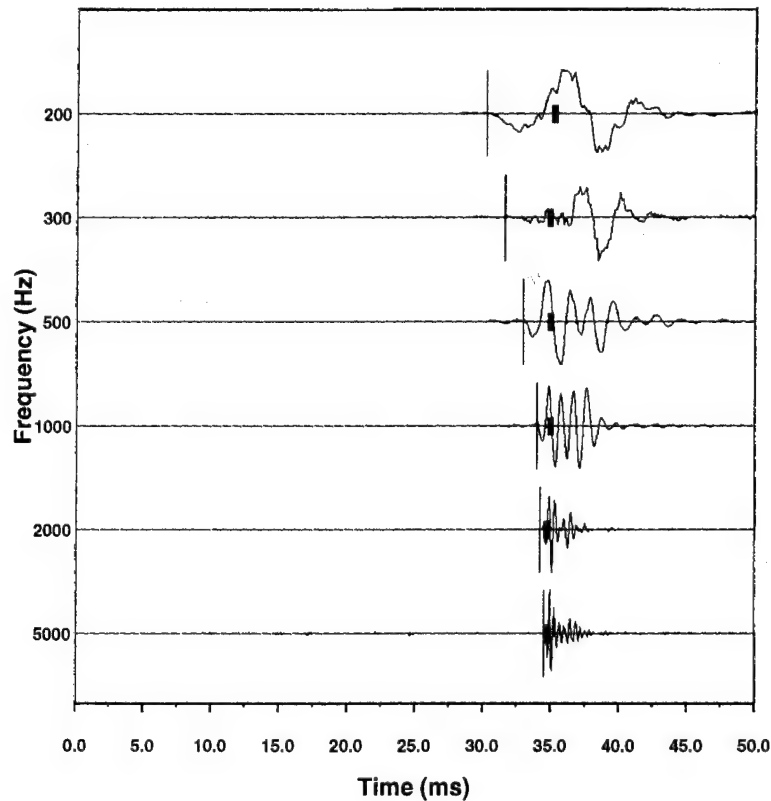


FIG. 2. Arrival waveforms at varying frequencies from 200–500 Hz between a source at 10 m depth and a receiver at 12.5 m depth.

propagating through the limestone layer used in our experiments.

Intrinsic dispersion

Limestone.—The velocity-frequency dispersion data of the permeable limestone obtained from the waveform arrival data shown in Figure 3 are plotted and compared with the Biot model and the BISQ model in Figure 5a. The model parameters used in the calculation are listed in Table 1. The values of porosity and shear modulus are extracted from the seismic velocity image shown later in this paper. The average permeability of the 15-m thick limestone layer measured from the pumping test is 331 darcies. The layer is known to contain fist-sized cavities (Missimer and Associates, Inc. 1992, Internal Report). No other physical properties were

measured. The squirt flow length can be varied from 0.01 mm to 10 mm in the frequency range shown (1–10⁵ Hz) at this high permeability (200 darcies) with no discernable effect on the BISQ curve. Because velocity dispersion is insensitive to other model parameters for the BISQ and Biot models, we used nominal values given in Yamamoto and Turgut (1988) as these model parameters. Given these other model parameters, the BISQ model gives the best-fit values of the permeability at approximately 200 darcies. The Biot theory fits the relaxation frequency but fails to model the large measured velocity dispersion. The input shear modulus value would have to be lowered to better fit the data. The BISQ model fits the relaxation frequency and the velocity dispersion of the data well, except for the 200 Hz point which is less reliable as can be seen in Figure 3. The question of how one measures the squirt-flow length remains to be

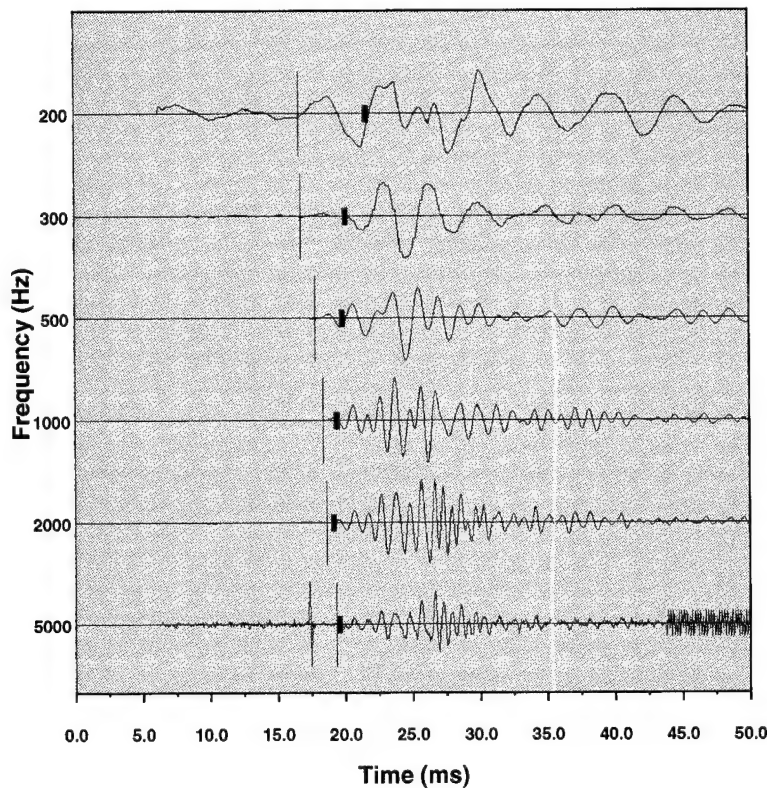


FIG. 3. Arrival waveforms at varying frequencies from 200–5000 Hz between a source at 27 m depth and a receiver at 28.5 m depth.

Table 1. Physical properties.

Property	Symbol (units)	Limestone	Sand	Mud
Permeability	k (darcies)	200	125	0.01
Porosity	β	0.33	0.40	0.60
Bulk modulus (frame)	K_S (Pa)	7.6×10^9	5.1×10^9	2.0×10^9
Shear modulus	μ (Pa)	3.5×10^9	2.35×10^9	1.2×10^9
Squirt length	R (m)	0.01 – 1.e-5	0.01 – 1.e-5	1.e-5

answered; nonetheless, the model-experiment comparisons are favorable.

Sandstone.—The model-experiment comparisons of the velocity-frequency dispersion and attenuation for the partially cemented sandstone aquifer are shown in Figure 6a and 6b. The data were obtained from the pulse transmission between the source at depth 31 m and the receiver at a depth of 38.5 m. The values of the model parameters used in the calculations are listed in Table 1. The values of porosity and shear modulus are extracted from the seismic velocity. The squirt-flow length can vary again from 0.01 mm to 10 mm in this frequency range. No permeability values of this layer

have been measured by pumping test. The BISQ model predicts the average permeability of this layer to be approximately 125 darcies. Again, the Biot theory grossly underestimates the velocity dispersion while the BISQ model agrees with the data.

Mud.—The velocity-frequency dispersion of the mud layer is negligibly small for the frequency range 200–5 000 Hz used in this experiment (Figure 2). This behavior can be modeled by both the Biot and BISQ models when a small value of permeability of the order of 0.01 darcies is assumed. The values of the model parameters used in the calculations are listed in Table 1. The values of porosity and shear modulus are extracted from the seismic velocity. The model-experiment comparisons of the velocity-frequency dispersion and attenuation are shown in Figure 7a and 7b. Squirt-flow length is .01 mm in this example and cannot be varied more than half an order of magnitude in this frequency range because of the much lower permeability. Very small values of attenuation are noticeable in the frequency range covered in the experiments in this layer.

PERMEABILITY IMAGE

A typical common-source gather at 1 kHz, source depth 7 m, is shown in Figure 8. Signals are normalized by the maximum value of each trace in this display. Signals are amplified from 20 m to 30 m to clearly show the first arrival. The total wavefield is complicated by reflected waves and scattered waves. We use only the first-arrival data in our tomography inversion. A travelttime inversion has been performed for the 35×96 first-arrival data set using the damped least-square inversion algorithm in Bregman et al. (1989). The velocity images inverted from 2 kHz, 1 kHz, and 250 kHz data are shown in Figures 9a, 9b, and 9c, respectively. The source well is located at the left side and the

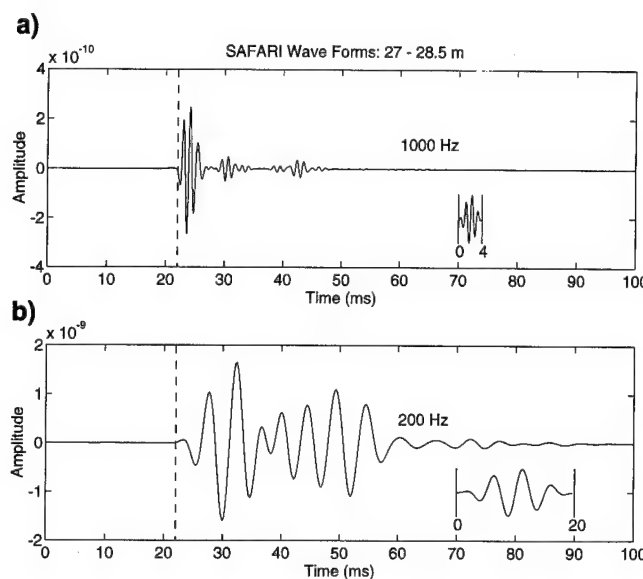


FIG. 4. SAFARI model waveforms for (a) 1000 Hz and (b) 200 Hz test cases between a source at 27 m depth and a receiver at 28.5 m depth.

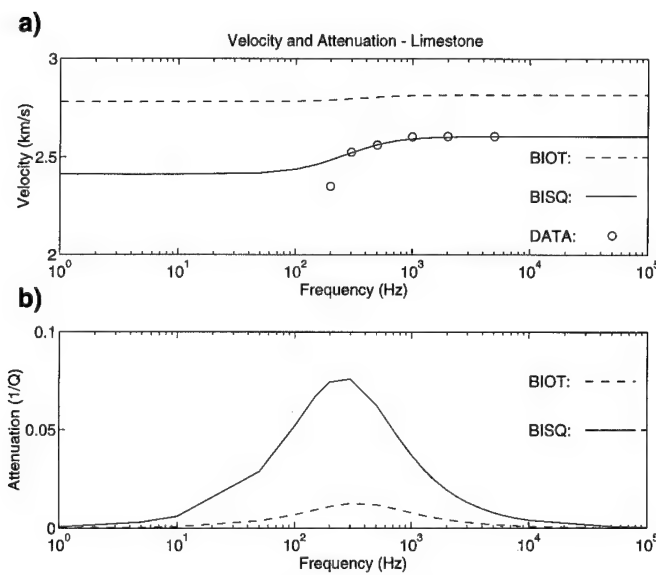


FIG. 5. Biot theory and Biot-squirt flow (BISQ) theory data (limestone) for (a) velocity dispersion vs frequency and (b) attenuation dispersion versus frequency (theory only).

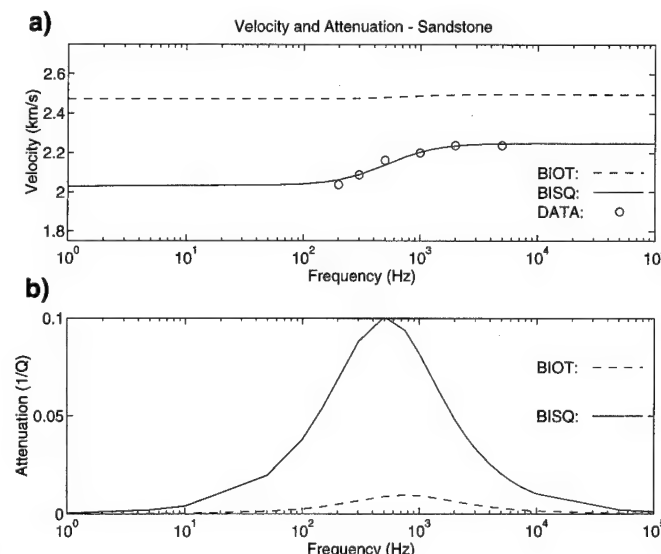


FIG. 6. Biot theory and Biot-squirt flow (BISQ) theory versus data (partially cemented sandstone) for (a) velocity dispersion versus frequency and (b) attenuation dispersion versus frequency (theory only).

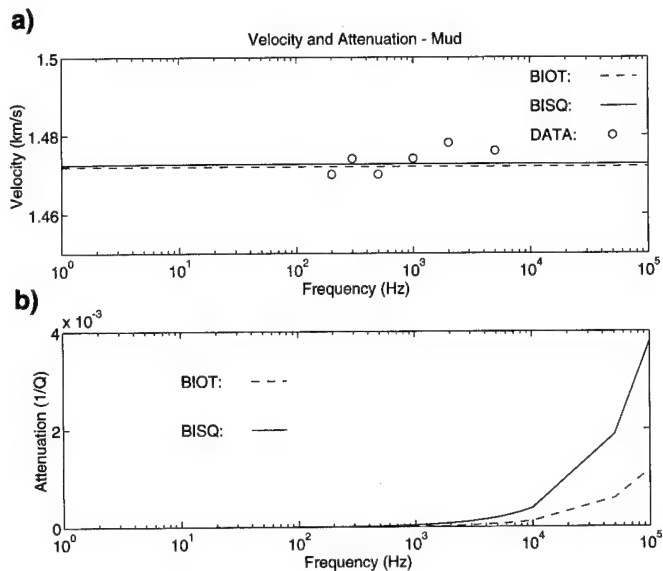


FIG. 7. Biot theory and Biot-squirt flow (BISQ) theory data (mud) for (a) velocity dispersion versus frequency and (b) attenuation dispersion versus frequency (theory only).

receiver well at the right side of each image. The source and receiver positions used in the crosswell measurements are shown by the hatch marks at both sides of each velocity image. All three images show essentially the same geological structure and are well correlated with the stratigraphy measured in receiver well LM-2061 (Figure 1). The 5-m thick sand layer at the top, the 15-m thick mud layer, the 15-m thick limestone layer, and the thick sand layer at the bottom are all identifiable from each image. The geometry of the experiment does not allow accurate traveltime measurements to be made in the sand layer below 30 m near the source well. A close examination reveals that these layers are not homogenous and exhibit horizontal and vertical variations. This type of heterogeneity is characteristic of the geology of shallow ocean sediments (Shepard, 1973).

The 2 kHz velocity image and the 1 kHz velocity image are practically identical, which indicates there is a small velocity dispersion in the cross-section in this frequency range. The 250 Hz velocity image shows a lower velocity in the limestone layer when compared with the 2 kHz or 1 kHz velocity image. The velocity of the mud layer does not change much among the three frequencies, indicating the impermeable nature of this layer. This overall tendency agrees with the

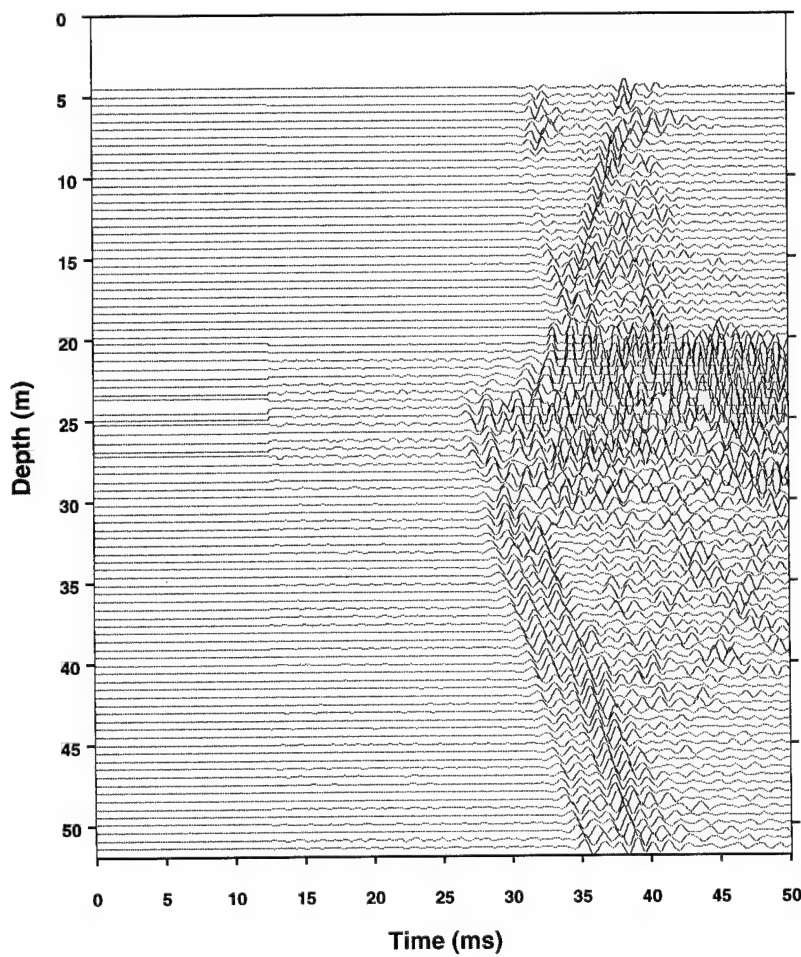


FIG. 8. Common source gather for source position at 7 m depth and 96 receiver positions from 4.5 m to 52.5 m depth (normalized). Source frequency is 1 kHz.

velocity-frequency dispersion data for the three sublayers examined earlier in this paper.

The velocity dispersion image, and therefore the permeability image, may be obtained by taking the velocity difference image between two frequencies. Figure 10 is the velocity difference image created by subtracting the 250 Hz velocity image of Figure 9c from the 1 kHz velocity image of Figure 9b. The limestone layer in the middle shows large, positive velocity differences as high as 500 m/s, indicating the high permeability of this layer of the order of 200 darcies. The velocity difference within the limestone layer is not homogeneous, however, indicating the variability of permeability within the layer. The bottom layer, partially lithified sandstone, shows a smaller velocity difference between the two frequencies, indicating less permeability.

The average permeability of the limestone layer measured from pumping tests is 331 darcies, assuming a homogeneous 15-m thick permeable layer (Missimer and Associates, Inc., 1992, Internal Report). The velocity difference image in Figure 10 reveals that the permeability structure of the entire aquifer formation varies in both the horizontal and vertical directions. This information cannot be obtained from pumping tests, which provide only an average permeability value for the entire aquifer.

POROSITY AND SHEAR STRENGTH IMAGES

We have presented a procedure to extract the porosity and the shear strength from a velocity image for water-saturated unlithified sediments in a recent paper (Yamamoto, et al., 1994). To extend the extraction procedure to lithified sediments, we used the procedure outlined in the earlier section on rock physics transformation. A porosity value of 0.27 was the cutoff criteria used for the switch from unlithified to lithified sediment (no glacial tills exist in the test site). Figure 11 displays the porosity image transformed from the compressional-wave velocity (1 kHz) image of Figure 9b. The porosity scale ranges from 0.20 (blue) to 0.60 (red). The upper 5 m (where the experiment did not penetrate because of the depth of the water level) should be ignored. The soft mud layer has porosities ranging from 0.4 to 0.6. The lithified condition takes over near 20 m depth and remains in effect to the bottom of the section. Porosity of the limestone and partially cemented sandstone can be found near 0.33 and 0.40, respectively, which are the values used in the Biot and BISQ curves of Figures 5 and 6 (see also Table 1).

Figure 12 shows the shear strength image for the combined lithified/unlithified transformation obtained from the compressional velocity. Again, the upper 5 m contains no useful information. The distinction between the limestone layer at 20 m and the soft mud above that layer is clear. The shear strength increases by an order of magnitude at the boundary

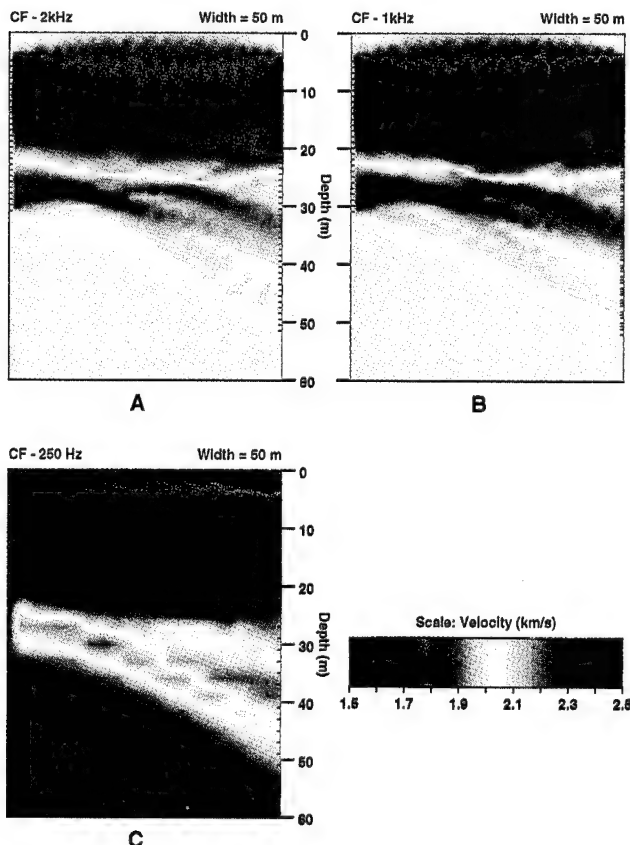


FIG. 9. Velocity tomograms for test cases (a) 2 kHz, (b) 1 kHz, and (c) 250 Hz at Westinghouse test site near Fort Myers, Fl.

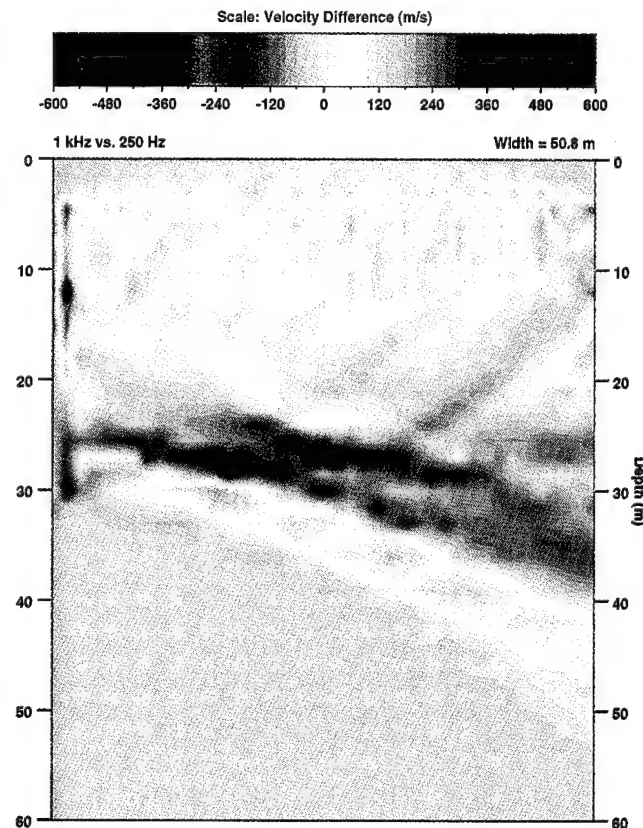


FIG. 10. Cross-section of the velocity difference between the 1 kHz test case and the 250 Hz test case at the Westinghouse test site.

between lithified and unlithified calculations. A shear strength of 6800 kPa corresponds to a shear modulus of 3.5 GPa which is the input for the Biot and BISQ theory prediction of limestone dispersion (Figure 5, Table 1).

A shear strength of 4500 kPa corresponds to a shear modulus of 2.35 GPa, which is the value used as the input to the Biot and BISQ theory predictions of sandstone dispersion (Figure 6, Table 1). These calculated values of porosity and shear strength from the lithified transformation from compressional-wave velocity work well as inputs to the BISQ model, as is demonstrated by the accurate match with the velocity-frequency dispersion data.

DISCUSSION

In this section, we discuss the problems encountered during this study and possible future improvements. In the attempt to image the permeability structure through velocity-frequency dispersion, we repeat the crosswell measurements many times using different carrier frequencies ranging between 200 and 5 000 Hz of PRBS codes. Since a PRBS signal at a high carrier frequency (say, 5 kHz) contains seismic energy having a broad frequency band (say, 50 Hz to 20 kHz), the high frequency PRBS data should contain information about velocity-frequency dispersion in a frequency band broad enough to resolve permeability structure. We can then apply band-pass filters to the high-

frequency PRBS data to isolate narrow-band energy at many incremental frequencies to obtain the velocity-frequency dispersion. If this can be done, it saves time and effort in the crosswell measurements and data analysis, and it also provides the continuous velocity-frequency dispersion structure of the sedimentary formation that is needed to determine the permeability structure.

The empirical seismic velocity model of Han et al. (1986) in the form of equations (1) and (2) provides the values of the model coefficients for sandstones only at discrete values of confining pressure ranging between 50 and 400 bars, thus our adopted model of equations (1) and (2) for the near-surface sediments (confining pressure ranging between 0 and 2 bars) may not be very accurate. The ultrasonic pulse transmission tests in Han et al. (1986) should be made at much smaller confining pressures for both sandstones and limestones to increase the accuracy of the model for near-surface applications.

It will be desirable, if it is ever possible, to perform different acoustic methods of permeability measurement on the same sediment, including crosswell acoustic tomography (this study), acoustic logging (Burns, 1988), and ultrasonic pulse transmission tests performed on core specimens (Han et al., 1986). These experiments should be compared with the BISQ model to improve our understanding of the effect of the sediment permeability on the seismic wave propagation. In particular, better understanding of the squirt-flow

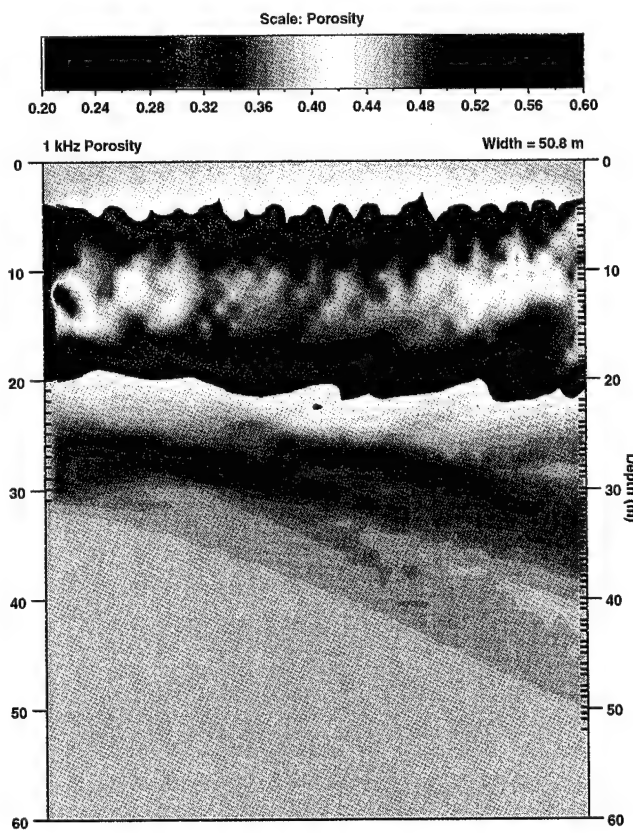


FIG. 11. Cross-section of the porosity at the Westinghouse test site as transformed from the 1 kHz velocity tomograph (Figure 9b).

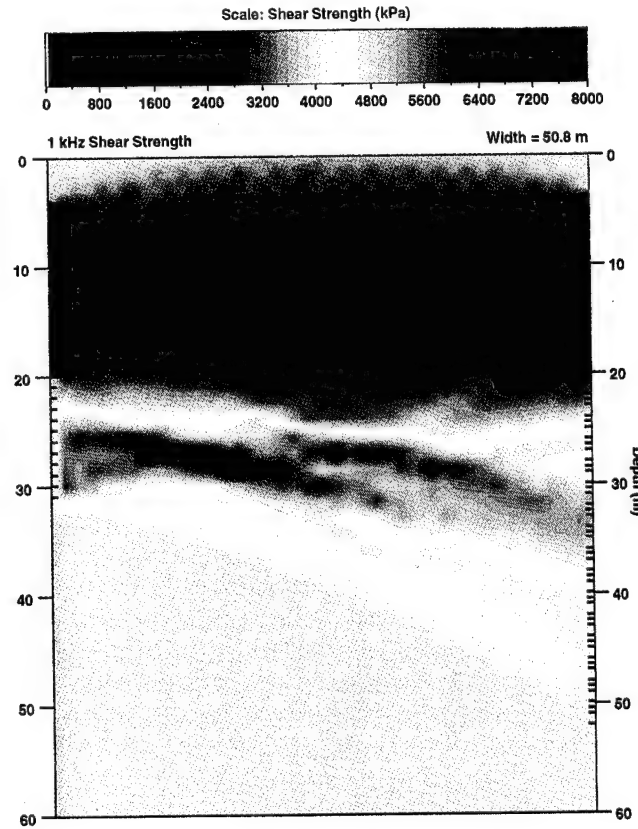


FIG. 12. Cross-section of the shear strength at the Westinghouse test site as transformed from the 1 kHz velocity tomograph (Figure 9b).

distance for various sediments is needed to extract the permeabilities of various sediments when using crosswell acoustic tomography.

CONCLUSIONS

The procedure to extract the permeability, porosity, and shear strength from measured acoustic velocity images has been extended to the general case of mixed lithified and unlithified sediments. The empirical relations between porosity and seismic velocities in Han et al. (1986) and the unified Biot-squirt flow (BISQ) theory in Dvorkin et al. (1994) have been incorporated in the original extraction procedure in Yamamoto et al. (1994).

Crosswell tomography experiments across a Florida limestone aquifer were repeated using the pseudorandom binary sequences of various carrier frequencies between 200 Hz and 5 kHz. The measured velocity-frequency dispersion of various sediment layers agreed with the prediction by the BISQ model. The acoustically measured permeability of the limestone layer agreed reasonably well with the permeability measured from pumping tests.

The velocity difference images constructed from subtracting velocity images of different frequencies reveal the permeability structure of the entire aquifer. The generalized transformation procedure also reasonably extracted the porosity and shear strength structures.

ACKNOWLEDGMENTS

This research was sponsored by Kawasaki Steel Corporation. The time for the preparation of this manuscript was sponsored by the Office of Naval Research, Ocean Acoustics Program (Mohsen Badiey and Jeff Simmen). We thank Andy Rogers who conducted the numerical analysis of pulse propagation using the SAFARI program. We also thank W. S. Harlan, J. Dvorkin, and D. Han for their review comments and suggestions for improving the revised manuscript.

REFERENCES

Biot, M. A., 1956, Theory of propagation of elastic waves in fluid-saturated porous solid. I. Low-frequency range: *J. Acoust. Soc. Am.*, **28**, 168–178.

Bourbié, T., Coussy, O., and Zinszner, B., 1987, *Acoustics of porous media*: Gulf Publishing Co.

Bregman, N. D., Bailey, R. C., and Chapman, C. H., 1989, Crosshole seismic tomography: *Geophysics*, **54**, 200–215.

Burns, D. R., 1988, Viscous fluid effects on guided wave propagation in a borehole: *J. Acoust. Soc. Am.*, **83**, 463.

Cunningham, A. B., 1978, Some alternate vibrator signals: *Geophysics*, **44**, 1901.

Dvorkin, J., Nolen-Hoeksema, R., Nur, A., 1994, The squirt-flow mechanism: Macroscopic description: *Geophysics*, **59**, 428–438.

Dvorkin, J., and Nur, A., 1993, Dynamic poroelasticity: A unified model with the squirt and the Biot mechanism: *Geophysics*, **58**, 524–532.

Gregory, A. R., 1976, Fluid saturation effects on dynamic elastic properties of sedimentary rocks: *Soc. Expl. Geophys. Seismic and acoustic velocities in reservoir rocks*, Vol. 1: Experimental studies, 237–258.

Gibson, R. L., and Toksöz, M. N., 1989, Viscous attenuation of acoustic waves in suspensions: *J. Acoust. Soc. Am.*, **85**, 1925–1934.

Hampton, L. D., 1967, Acoustic properties of sediments: *J. Acoust. Soc. Am.*, **42**, 880–890.

Han, D., Nur, A., and Morgan, D., 1986, Effects of porosity and clay content on wave velocities in sandstones: *Geophysics*, **51**, 2093–2107.

Ishihara, K., 1976, *Foundation of soil dynamics* (in Japanese): Kajima Press.

Johnson, D. L., and Sen, P. N., (edited), 1983, *Physics and chemistry of porous media*: Am. Institute of Physics.

Klimentos, T., and McCann, C., 1990, Relationships among compressional wave attenuation, clay content, and permeability in sandstones: *Geophysics*, **55**, 998–1014.

Mavko, G., and Nur, A., 1979, Wave attenuation in partially saturated rocks: *Geophysics*, **44**, 161–178.

Murphy, W. F., Winkler, K. W., and Kleinberg, R. L., 1986, Acoustic relaxation in sedimentary rocks: Dependence on grain contacts and fluid saturation: *Geophysics*, **51**, 757–766.

Nur, A., and Wang, Z., 1989, *Seismic and acoustic velocities in reservoir rocks: Volume 1, Experimental Studies*: Geophysics reprint series No. 10: Soc. Expl. Geophys.

Paillet, F. L., and Cheng, C. H., 1991, *Acoustic waves in boreholes*: CRC Press.

Rosenbaum, J. H., 1974, Synthetic microseismograms: Logging in porous formations: *Geophysics*, **39**, 14.

Schmidt, H., 1987, SAFARI—Seismo-acoustic fast field algorithm for range independent environments users guide: SACLANTCEN SR-113.

Shepard, F. P., 1973, *Submarine geology* (3rd edition), Harper and Row.

Terzaghi, K., and Peck, R. B., 1960, *Soil mechanics in engineering practice*: John Wiley & Sons, Inc.

Tittmann, B. R., Bulan, J. R., and Abde-Gawad, M., 1984, AIP Conference proc #107 physics and chemistry of porous media, 131–143.

Toksöz, M. N., and Johnston, D. H., 1981, Seismic wave attenuation, *Geophysics* reprint series, 2: Soc. Expl. Geophys.

Turgut, A., and Yamamoto, T., 1990, Measurements of acoustic wave velocities and attenuation in marine sediments: *J. Acoust. Soc. Am.*, **87**, 2376–2383.

Wang, Z., and Nur, A., 1990, Dispersion analysis of acoustic velocities in rocks: *J. Acoust. Soc. Am.*, **87**, No. 6 2384–2395.

Williams, D. M., Zemanok, J., Angona, F. A., Dennis, C. L., and Caldwell, R. L., 1984, The long space acoustic logging tool: Trans. 25th Soc. of Prof. Well Log Anal. Ann. Logging Symp., Paper T.

White, J. E., 1983, *Underground sound: Application of seismic waves*: Elsevier Science Publications.

Yamamoto, T., Nye, T., and Kuru, M., 1994, Porosity permeability, shear strength: Crosswell tomography below an iron boundary: *Geophysics*, **59**, 1530–1541.

Yamamoto, T., Trevorrow, M., Badiey, M., and Turgut, A., 1989, Seabed porosity and shear modulus inversion using surface gravity (water) wave-induced seabed motion: *Geophys. J. Int.*, **98**, 173–182.

Yamamoto, T., and Turgut, A., 1988, Acoustic wave propagation through porous media with arbitrary pore size distributions: *J. Acoust. Soc. Am.*, **83**, 1744–1751.

APPENDIX A

POROSITY AND SHEAR STRENGTH TRANSFORMATION PROCEDURES FOR UNLITHIFIED SEDIMENTS

In a group of unlithified sediments, the shear modulus μ is a unique function of porosity β and the confining effective stress σ as given by the empirical relation (Yamamoto et al., 1989):

$$\mu = A \left(\frac{1 - B}{\beta} \right)^{1.12} \sigma^{0.5}, \quad (\text{A-1})$$

where $A = 1.835 \times 10^5$ (Pa)^{0.5}. This relationship is based both on laboratory tests and on field seismic data from sandy, silty, and mixed-clayey sediments.

The confining stress σ at a given depth of burial z can be found as

$$\begin{aligned} \sigma &= \frac{1}{3} (\sigma_x + \sigma_y + \sigma_z) \\ &= \int_0^z \frac{1 + 2K_0}{3} (\rho_r - \rho_f) g (1 - \beta) dz, \end{aligned} \quad (\text{A-2})$$

where g = acceleration of gravity, ρ_r = density of the grain, ρ_f = density of the fluid, and $K_0 = 1 - \sin \phi_0$ ($\phi_0 \approx 30^\circ$ in natural sediment).

Using the measured low-frequency velocity V_0 , one can estimate the porosity β as

$$\beta = \frac{K_f (K_r - K)}{(K_r - K_f) (K - K_S)}, \quad (\text{A-3})$$

where

$$K = \rho (V_0^2 - V_S^2) \quad (\text{A-4})$$

and

$$V_S = (\mu / \rho)^{0.5}. \quad (\text{A-5})$$

Here, K_f = bulk modulus of water, K_r = bulk modulus of the sediment grains, K_S = is the bulk modulus of the sediment framework, ρ = bulk density of the sediment, and V_S = shear wave velocity.

Numerically, porosity β and shear modulus μ are determined iteratively from equations (A-1) to (A-5).

APPENDIX B

THE BIOT-SQUIRT FLOW (BISQ) MODEL

The assumption is that the solid skeleton of a rock deforms in the uniaxial mode parallel to the direction of wave propagation. The fluid flows parallel to this direction (Biot's flow) and perpendicular to it (squirt flow) (from Dvorkin and Nur, 1993; Dvorkin et al., 1994).

In Biot theory, there is a proportionality coefficient F that relates the derivatives of pressure to the derivatives of the fluid and solid displacements.

$$F = \left(\frac{1}{\rho_f c_0^2} + \frac{1}{\beta H} \right)^{-1}, \quad (\text{B-1})$$

where ρ_f is the fluid density, c_0 is the acoustic velocity in the fluid, β = porosity, and H is defined as

$$\frac{1}{H} = \frac{1}{K_r} \left(1 - \beta - \frac{K_S}{K_r} \right). \quad (\text{B-2})$$

K_S is the bulk modulus of the sediment frame, and K_r is the bulk modulus of the sediment grains. (Note the change in symbols from Dvorkin and Nur to match Appendix A, Table 1 convention.)

The combined Biot-squirt flow (BISQ) model is calculated similar to Biot theory (Biot, 1956; Dvorkin and Nur, 1993; or Yamamoto and Turgut, 1988) by changing coefficient F to coefficient F_{sq} as

$$F_{sq} = F \left[1 - \frac{2J_1(\lambda R)}{\lambda R J_0(\lambda R)} \right], \quad (\text{B-3})$$

where J_0 and J_1 are Bessel functions of zero order and first order, respectively.

$$\lambda R = \left[\frac{R^2 \rho_f \omega^2}{F} \left(\frac{\beta + \frac{\rho_a}{\rho_f}}{\beta} + i \frac{\omega_c}{\omega} \right) \right]^{1/2}, \quad (\text{B-4})$$

where λ is the wavenumber, R is the characteristic squirt-flow length, ω is the angular frequency ($2\pi f$), ρ_a is the additional coupling density, and

$$\omega_c = \frac{\nu \beta}{k}. \quad (\text{B-5})$$

Here, the kinematic viscosity ν is 10^{-6} m²/s and k is permeability in m²/s. The term:

$$\frac{\beta + \frac{\rho_a}{\rho_f}}{\beta} \quad (\text{B-6})$$

may be ignored to make the model more stable (Dvorkin et al., 1994). The F_{sq} term is substituted for F in the Biot theory to create the BISQ model.

Concurrent measurements of the directional spectra of microseismic energy and surface gravity waves

T. Nye and T. Yamamoto

Division of Applied Marine Physics, Rosenstiel School of Marine and Atmospheric Sciences, University of Miami, Florida

Abstract. This paper presents concurrent measurements of surface wave directional spectra and double-frequency, long-wave microseisms. Long-wave energy rapidly develops during periods of shifting winds which create bidirectional sea states. Theoretically, nonlinear sum interactions of opposing wavenumber vectors of approximately the same frequency create long-wave energy at twice the frequency, which is only slightly attenuated in shallow water. Bidirectional sea states have been found using a buried ocean bottom seismometer measuring system from which the long wave energy has been measured at double frequencies. This system was incorporated into the Office of Naval Research sponsored Sources of Ambient Microseismic Ocean Noise (SAMSON) experiment for 3 months off the Army Corps of Engineers' Field Research Facility near Duck, North Carolina in the fall of 1990. Four working sensors produced directional spectra results from nearly 22 gigabytes of recorded data, which was collected 2 km offshore of the FRF under 12-13 m of water and approximately 1 m of sediment. Because of the insignificant attenuation the measured energy levels of the double frequency microseisms at the seafloor are of the same order of magnitude as the single-frequency, surface wave energy induced seafloor motion. Various data sets were analyzed that confirmed Longuet-Higgins' theory, which proposes that the propagation direction of double-frequency microseisms occurs in the direction of the vector sum of the opposing single-frequency seas.

Introduction

In September 1990, an Office of Naval Research (ONR) sponsored multiinstitutional project named Sources of Ambient Microseismic Ocean Noise (SAMSON) began. The University of Miami's Geoacoustic Laboratory's (UM/GAL) contribution to this experiment was a six-point ocean bottom seismometer (OBS)/pressure array located 2 km offshore of the Army Corps of Engineers Field Research Facility (FRF) at Duck, North Carolina. The individual OBS/pressure units measured the directional spectra of the surface gravity waves as single-point measuring devices, as the array was not tuned to the gravity wave frequency band. An array of bottom-mounted pressure sensors (FRF units in 8 m water depth) is used as a comparison device to confirm the surface spectra [Nye and Yamamoto, 1993].

The UM/GAL array was tuned to measure energy in the 'double-frequency' microseism band. Longuet-Higgins [1950] proposed that microseisms may develop as a result of bidirectional seas with similar frequencies and opposing directions, creating a standing wave and causing pressure fluctuations, which in turn excite the seafloor at twice the frequency of the opposing wave trains. These 'double-frequency' oscillations can be propagated to great depths. This paper finds bidirectional sea states where the opposing vectors of the seas created the double-frequency microseismic energy. It will be shown that this energy is created when wind shifts cause the seas to bifurcate. The high-frequency

gravity waves are the first to move to the direction of the new wind, creating double-frequency microseism energy above 0.6 Hz. As the gravity wave energy that transfers to the new wind direction moves to lower-frequency bands, the double-frequency energy also moves to lower-frequency bands following the 2:1 ratio. After the sea state has stabilized to a unidirectional field, the double-frequency energy may remain for hours before diminishing altogether. Herbers and Guza [1992] have shown that the microseismic energy is also pronounced during unidirectional, high-energy sea states. The double-frequency microseisms are interface waves, allowing for measurements of power, point coherence/phase between vertical and horizontal seismometers, and spatial coherence/phase between units in the array.

Double-frequency microseisms are generated on the seafloor because of pressure fluctuations caused by nonlinear interactions between opposing wave trains of approximately the same frequency. Sum interactions and difference interactions occur between wave trains with $f_1 \approx f_2$ and $\mathbf{k}_1 \approx -\mathbf{k}_2$. The difference interaction produces energy at double frequency and double wavenumber (Stoke's second harmonic), which, because of the depth of the study area, do not reach the seafloor in the frequency band of interest (0.3-1.0 Hz). The sum interaction produces double-frequency oscillations with the wavenumber approximately equal to zero (Miche [1944] from Herbers and Guza [1991]). This very long wavelength energy endures almost no attenuation in 12-13 m water depths and thus produces pressure fluctuations on the seafloor at twice the frequency of the opposing surface waves. Herbers and Guza [1991] show that the interaction coefficient (C) between the opposing seas decreases if the separation of the bidirectionality becomes less than 180° or if

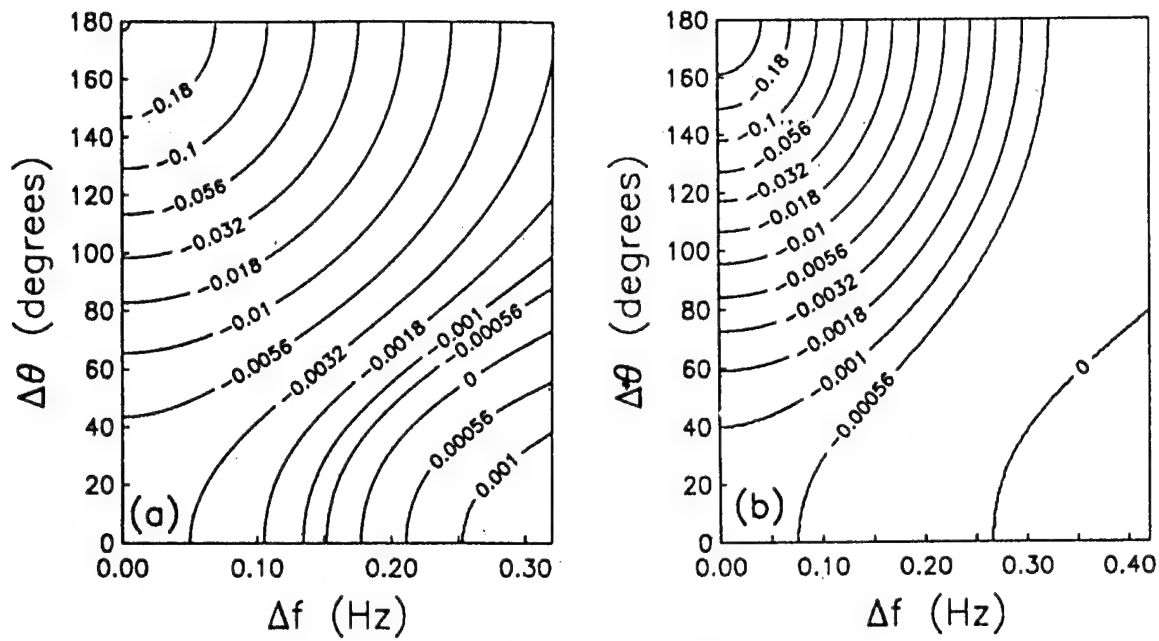


Figure 1. Nonlinear interaction coefficient (C) in 13 m depth as a function of $\Delta\theta$ and Δf for (a) f_0 equal to 0.4 Hz where $C = -0.32 \text{ m}^{-1}$ at $\Delta\theta = 180^\circ$ and $\Delta f = 0.0$ and (b) f_0 equal to 0.5 Hz where $C = -0.50 \text{ m}^{-1}$ at $\Delta\theta = 180^\circ$ and $\Delta f = 0.0$. [Herbers and Guza, 1991].

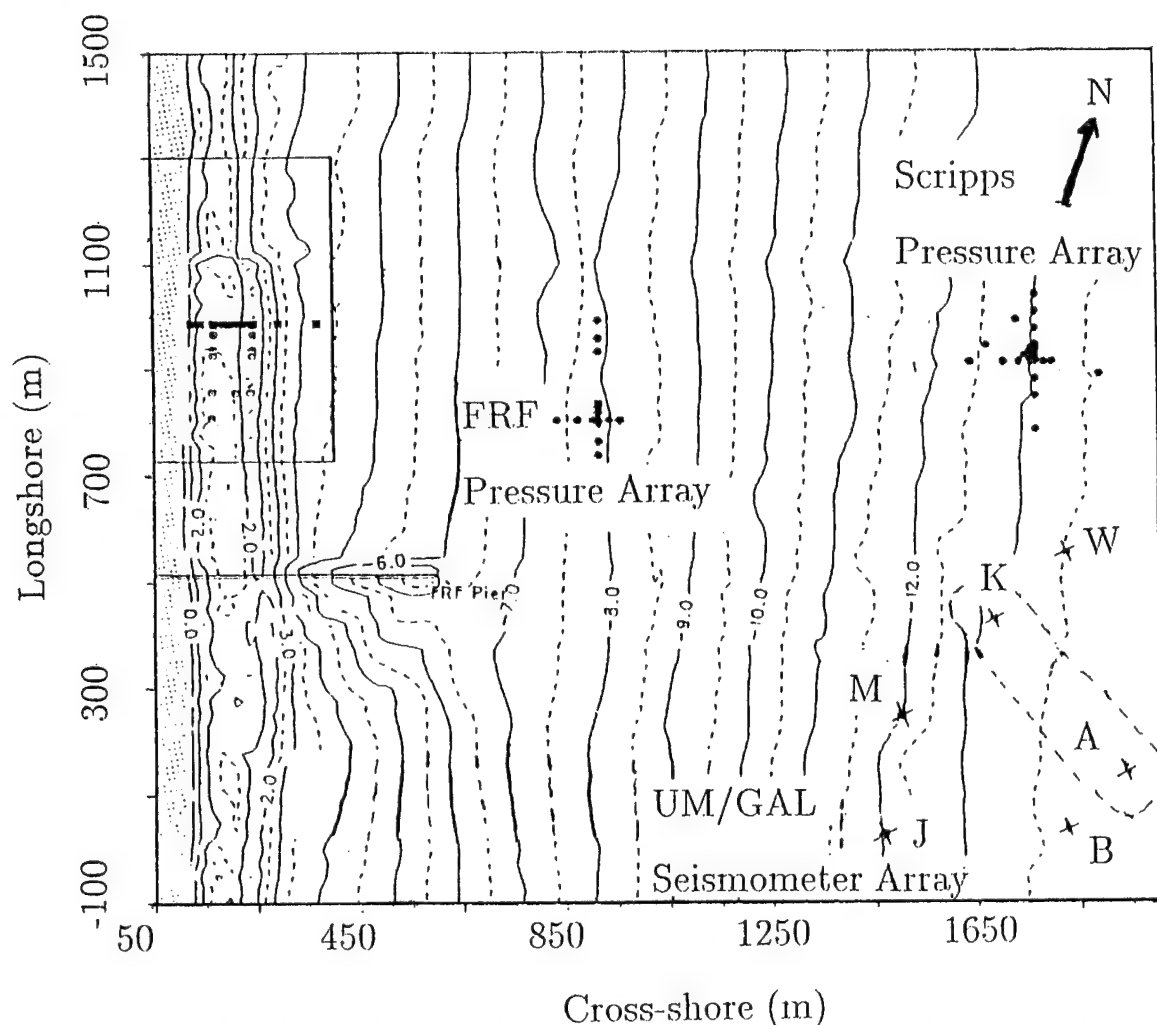


Figure 2. Map of the Sources of Ambient Micro-seismic Ocean Noise (SAMSON) experimental site.

Table 1. Instrument Positions

Instrument	Cross-Shore, m	Longshore, m	Depth, m
Joanna	1460	27	12.2
Miyuki	1502	205	13.7
Ayshe	1942	130	13.7
Beth	1817	46	12.8
Karen	1675	455	13.7
Wendy	1810	571	13.4

the frequency varies between the seas (see Figure 1). They calculated that C becomes a tenth of its maximum value if $\Delta\theta$ decreases to 90° in 13 m of water at $f_0 = 0.4$ Hz (this depth is similar to the SAMSON site and 0.4 Hz double-frequency fluctuations are common). The coefficient also decreases to a tenth of its maximum if $\Delta f = 0.2$ Hz when $f_0 = 0.4$ Hz. The frequency which is approximately double the frequency of the opposing seas is f_0 . The difference in frequency between the opposing seas is Δf and is centered at f_0 . With $f_0 = 0.5$ Hz, the calculated values reduced to 1% of the maximum for $\Delta\theta = 90^\circ$ or $\Delta f = 0.25$ Hz. Double-frequency energy often will be produced from opposing seas which are not 180° apart or of exactly the same frequency; however, for energy to develop in the higher-frequency bands, the seas must truly oppose and be of the same frequency.

The nonlinear interactions cause pressure fluctuations on the bottom which propagate away from the generation area at speeds much greater than the speed of the gravity waves. *Longuet-Higgins* [1950] proposed that if the two arms of the opposing seas were not 180° apart, the long-wave, double-frequency oscillation would propagate away from the generation area in the direction of the vector sum of the two seas.

SAMSON Experiment

The 1990 experiment offshore of the Corps of Engineers FRF at Duck, North Carolina (Figure 2) was part of the multiinstitutional Sources of Ambient Microseismic Ocean Noise (SAMSON) experiment. UM/GAL's contribution to this experiment was a near-shore (2 km) seismometer array consisting of six ocean bottom seismometers with pressure sensors (OBSs). Some other components of SAMSON are shown in Figure 2, including the FRF's 12-point, bottom-mounted pressure array, which was used to find the directional spectra of the surface waves. Located offshore of this array and to the north of the UM/GAL array, was Scripps Institute of Oceanography's 32-sensor, bottom-mounted pressure array. This array has a small aperture to measure surface wave directional spectra and a larger aperture to also find double-frequency microseism wavenumber vectors. The other instruments shown but not labeled are surf zone current meters. Duck, North Carolina, lies midway between Cape Hatteras and Virginia Beach on North Carolina's outer bank. This group of instruments represented SAMSON's near shore components. There were also offshore microseismic measurements and a large-aperture, land-based seismometer array.

The deployment of the UM/GAL array, which was tuned to find the directional spectra of double-frequency microseisms (array spacing being too large to find the directional spectra of gravity waves using array methods) began on September 6, 1990. Three kilometers of armored, 1-inch-

Table 2. Instrument Bearings

Instrument	Roll, deg	Pitch, deg	Heading, deg Azimuth
Joanna	0.0	2.0	112
Miyuki	3.5	2.0	82
Ayshe	4.2	3.0	135
Beth	7.5	3.0	107
Karen	5.5	0.4	285
Wendy	7.0	3.0	55

diameter coaxial cable was deployed offshore of the FRF. This cable contained three breakout points for instrument placement at the far end, 600 m in, and 1200 m in. At these points, three secondary armored, 5/8-inch-diameter, 200-m-long coaxial cables were deployed. In Table 1 the six instrument positions are given in meters cross-shore and longshore (x and y , respectively) from the origin of the FRF coordinate system, latitude $36^\circ 10' 38.77''$ N and longitude $75^\circ 45' 0.28''$ W. The six instrument packages were buried using divers and a hydraulic pump jet system which liquefied the sediment allowing the instruments to settle to depths of 1 m. The accelerometers were leveled by hand. Instrument tilts and headings (direction of horizontal seismometer labeled 'transverse') are given in Table 2.

The instrument package consisted of three separate units. The first was an accelerometer unit containing three orthog-

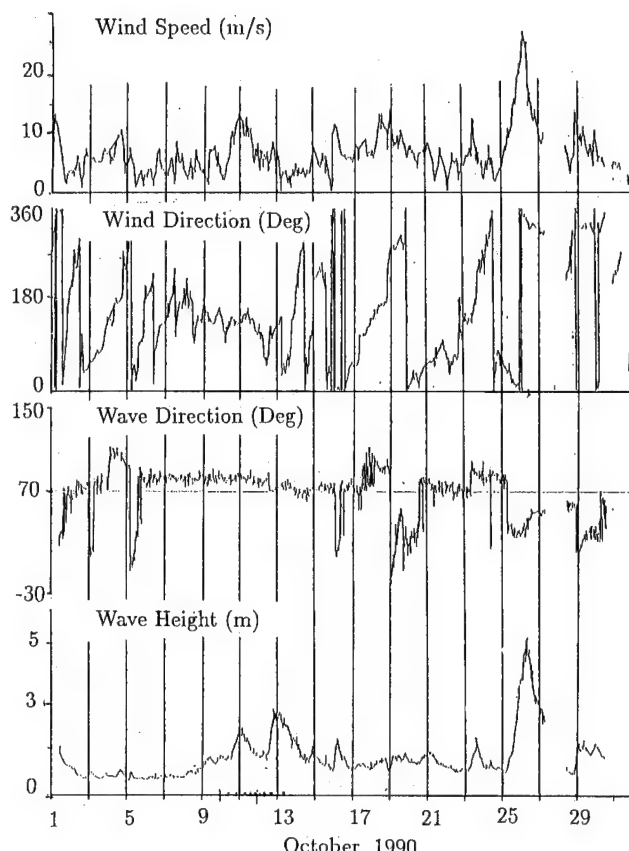


Figure 3. Wind and wave data for the month of October, 1990 collected from the Field Research Facility's pier gauges.

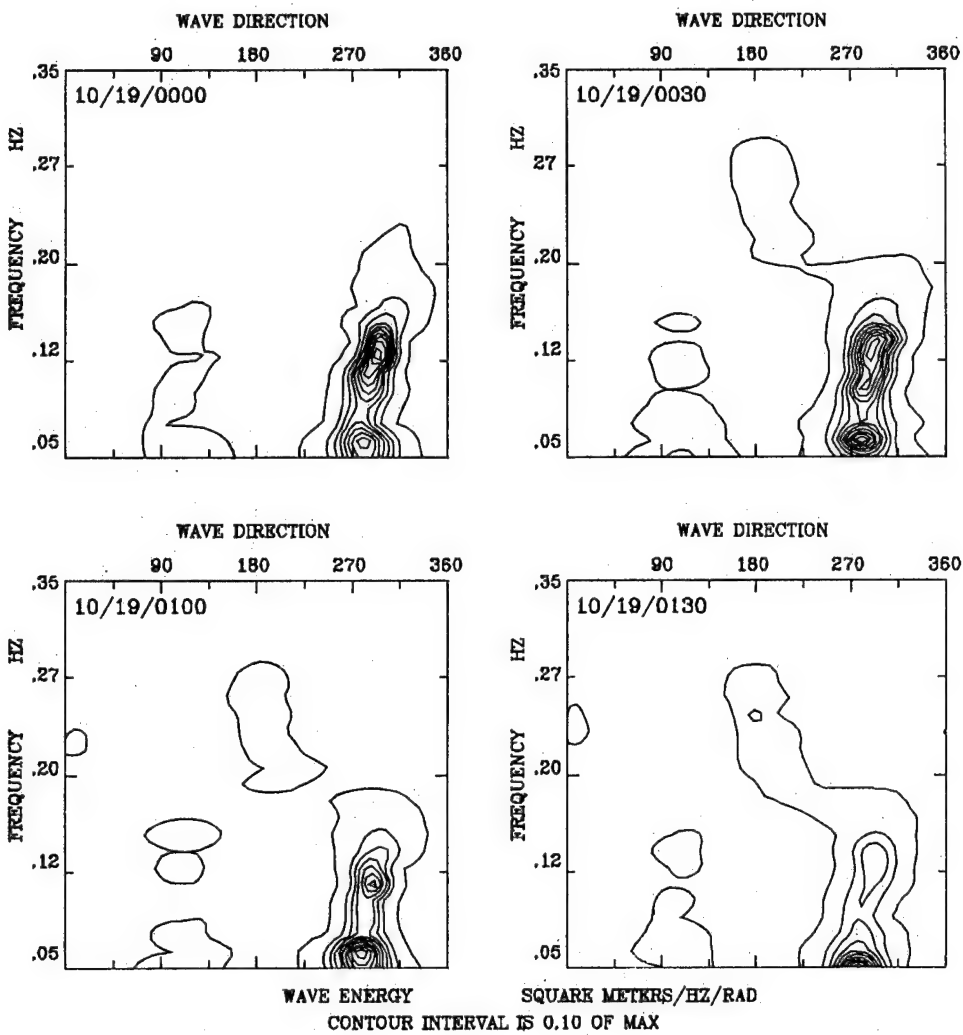


Figure 4. Directional spectra results from the 1990 SAMSON experiment for the Joanna unit for four 30-minute time periods beginning October 19, 0000, 0030, 0100, and 0130 UT, respectively.

onally mounted seismometers (Teledyne-Geotech models S-750 or S-510), a compass (Aanderaa model 1248), and two pendulum tiltmeters (Sperry model 02383-01). The accelerometer unit was cased in an aluminum alloy cylinder (diameter, 30.5 cm; height, 25.5 cm) which was approximately of neutral density in sediment to provide adequate coupling with the sea bottom. This housing is buried, with its axis oriented vertically, to a depth of 1 m. The second unit in the instrument package was an electronics container which consisted of an aluminum alloy housing (diameter, 23 cm; height, 48 cm) containing instrumental amplifiers, filters, digitizers, and digital multiplexer electronics. This unit served as a junction between the seismometer unit, the pressure sensor, and the electromechanical cable to shore. The final piece of the package was the pressure sensor (Precision Measurements Engineering model 109). The electronics housing and the pressure sensor were buried to depths of approximately 0.5 m to protect them from fishery activity.

During a period of repair to an instrument umbilical by cable manufacturers, a short to seawater apparently caused inductors in two instruments (Ayshe and Karen) to overheat. These inductors were on the digital multiplexer boards built by Teledyne-Geotech and could not be replaced by the start

date of the SAMSON project. Therefore these two units were out of commission and the experiment began with a four-point accelerometer array. Data acquisition began on October 9 and concluded on January 3, 1991.

Results

Wind and wave amplitude and direction are given in Figure 3 for the month of October 1990. Wind measurements were collected by anemometers on the FRF pier, while wave measurements are made by the FRF's array (wave height is given as significant wave height). This figure was produced by FRF personnel. A major wind shift occurred on October 18 while the wind speed remained high (8–15 m/s). The wind veered clockwise from northeast to northwest from the morning of October 17 to the morning of October 19. Most of the shift comes in the late evening of October 18. FRF instruments show that the mean wave direction shifted 120° (first coming from east and then coming from north-northwest) on the morning of October 19.

Figures 4 and 5 show the evolution of these seas as measured by the unit labeled Joanna. These plots represent the directional spectra of the surface gravity waves using a

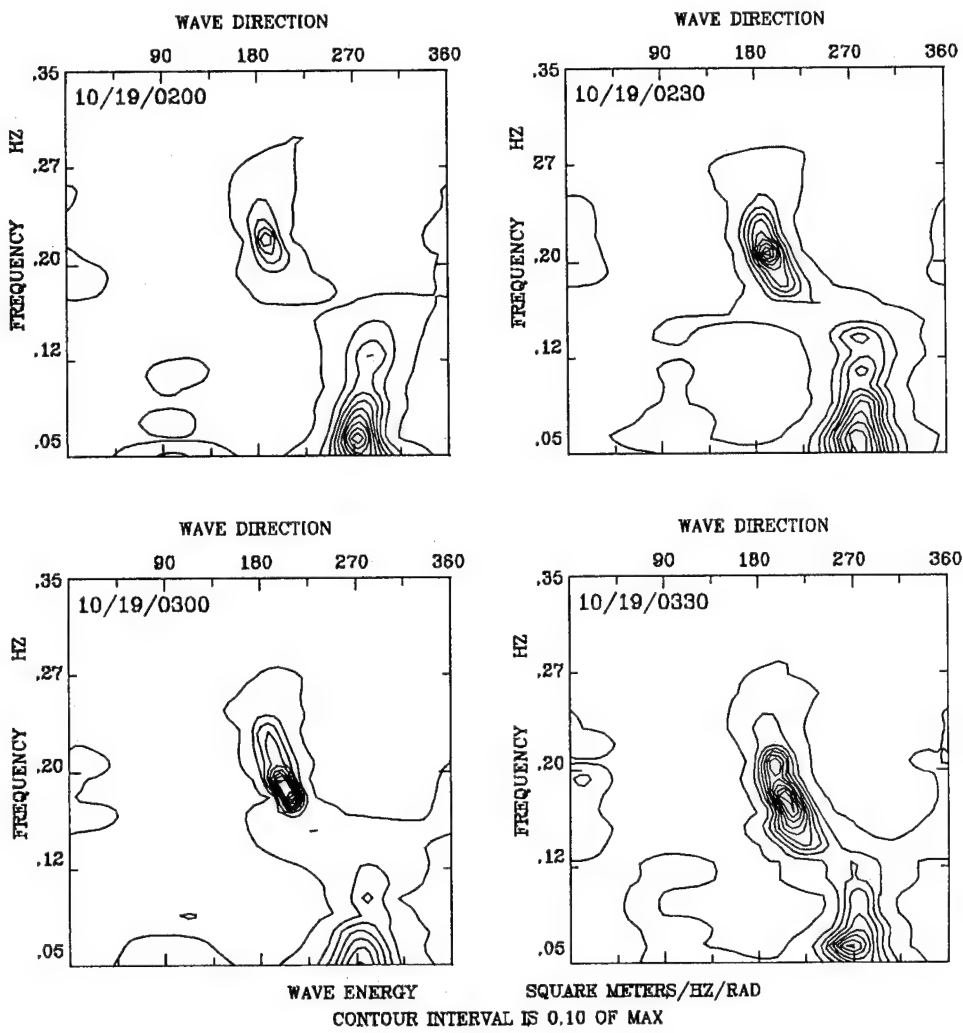


Figure 5. Directional spectra results from the 1990 SAMSON experiment for the Joanna unit for four 30-minute time periods beginning October 19, 0200, 0230, 0300, and 0330, respectively.

point, three-axis measurement (two directions of horizontal acceleration and pressure), and the maximum entropy analysis. The single-point measuring device favorably compared to FRF's bottom-mounted array of pressure sensors [Nye, 1992; Nye and Yamamoto, 1993]. The FRF plots are averaged over too long a time period (3 hours) to adequately show the evolving seas. The *x* axes of Figures 4 and 5 represent the direction of wave propagation from north. The FRF pier extends into the ocean at 70° perpendicular to the shore, therefore waves which perpendicularly approach the beach propagate toward 250°. The *y* axes are the wave frequency in Hz increasing from 0.05 Hz to 0.35 Hz. Any wave information at frequencies higher than 0.25 Hz is suspect owing to the shallow water cutoff (water depth is about 12 m). Figure 4 represents the directional spectra for the Joanna unit for four 30-minute time periods October 19, 0000 UT–October 19, 0130 UT from upper left to lower right respectively. The first plot (October 19, 0000 UT) shows wave energy propagating toward 280° at 0.06 Hz and 300° at 0.13 Hz. By 0030 UT, another sea begins to develop at 0.2–0.27 Hz, propagating toward 180°. This energy slowly builds through the next hour (graphs 10/19/0100 and 10/19/0130) as the 0.13 Hz/300° energy diminishes. Figure 5 dis-

plays the four 30-minute segments of the directional spectra of the Joanna unit from beginning at October 19, 0200 UT to beginning at October 19, 0330 UT from upper left to lower right. During the first segment (0200 UT) the waves propagate toward 180°/0.22 Hz and 270°/0.06 Hz. The following three time frames indicate wave energy building in the southerly direction and abating in the westerly direction. The peak frequency in the wind generated spectra moves from 0.22 Hz to 0.17 Hz during this interval. A closer inspection of graph 10/19/0230 reveals a bidirectional sea state at 0.16 Hz with the opposing vectors being 210° and 280°. This corresponds to an interaction coefficient of approximately -0.01 m^{-1} using Figure 1 with f_0 at 0.4 Hz (which is slightly high for this data). This is approximately 3% of the nonlinear interaction one could expect from truly opposing seas at exactly the same frequency. It will be shown that this is sufficient to create long-wave energy that impinges the seafloor to the same order of magnitude as the attenuated surface waves themselves. The vector sum of these two seas resides at 245°, which is the direction that the resulting double-frequency energy should propagate with a frequency near 0.32 Hz.

Figure 6 displays the power spectra for the Joanna unit's

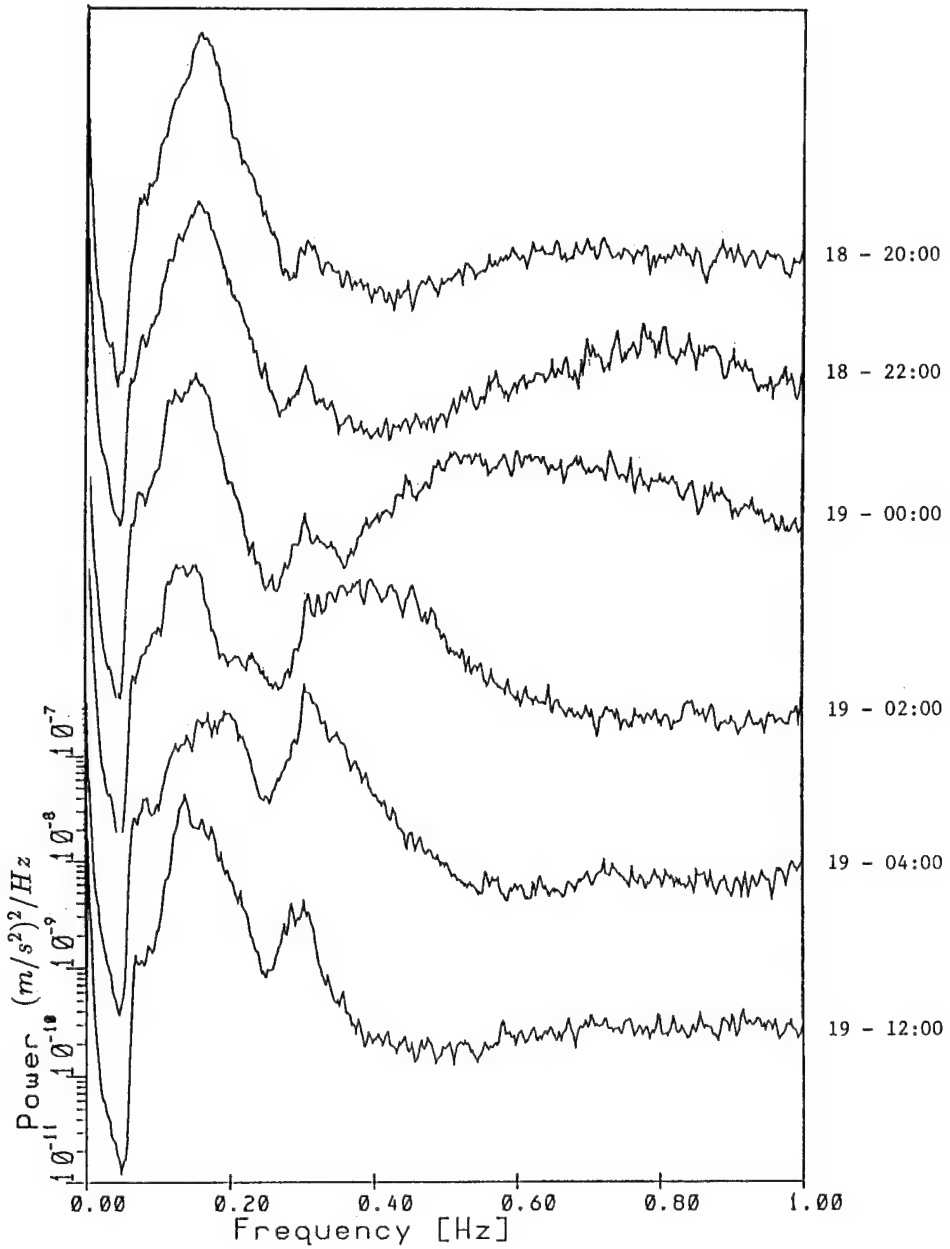


Figure 6. Vertical seismometer power spectra versus frequency for the Joanna unit time periods October 18, 1990, 2000 UT to October 19, 1990, 1200 UT.

vertical seismometer for 2-hour averaged data sets (October 18, 1990, 1800–2000 UT through October 19, 1990, 1000–1200 UT). This figure is given in frequency versus log power ($(\text{m/s}^2)^2/\text{Hz}$) with the October 18, 1800 UT data set displayed at the top. Because the wind is veering during this time one expects the high-frequency band to first develop wave energy aligned with the new wind. Young *et al.* [1987] indicate that there is a strong frequency dependence in directional relaxation with the low-frequency wind-driven waves lagging behind the high-frequency waves. However, there is more than one environmental factor working during this period. The wind has begun to shift by October 18, 1800 UT, but the waves which follow this shift at high frequencies are not yet measurable by bottom-mounted sensors. The small peak at 0.3 Hz on the first line of Figure 6 is long-wave microseismic energy which is not generated by opposing

seas because the spectrum is unidirectional at 0.15 Hz during this time segment. This energy is suspected to be long-wave energy because the spatial coherence is good and the spatial phase is steady between instruments far enough apart (up to 650 m) to safely rule out the possibility of it being gravity wave energy (to be shown later in Figures 13–16).

By 1800–2000 UT the high-frequency energy begins to produce double-frequency microseisms centered at $f_0 = 0.80$ Hz. The single-frequency (0.4 Hz) surface wave energy that presumably creates this peak is still immeasurable at the bottom, however the 0.3-Hz long-wave energy is still apparent during this segment of data. For the 0.8-Hz energy to be locally generated (a valid assumption given the weather conditions and the spectral plots that follow), it could be produced only as long-wave, double-frequency energy caused by the 'sum' nonlinear interactions of opposing wave

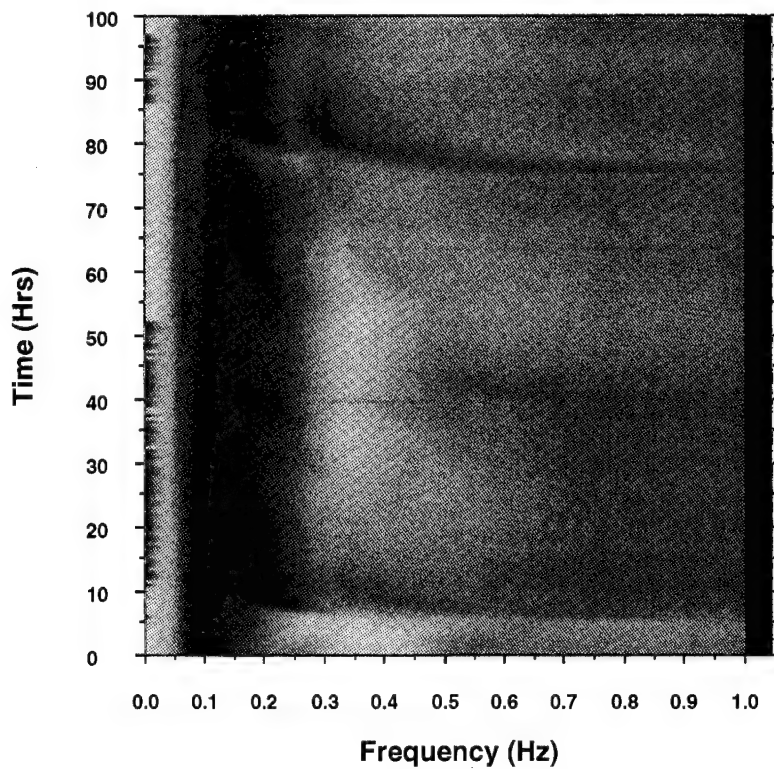


Figure 7. Vertical seismometer power spectra versus frequency for the Joanna unit time periods October 15, 1800 UT to October 19, 2000 UT.

trains. The single-frequency gravity waves at 0.4 Hz are attenuated by an inverse $\cosh(kd)$ term of the order of 10^{-12} and cannot affect the bottom. The Stoke's nonlinear interactions are double-frequency, half-wavelength and are attenuated even more. The long-wave energy attenuates very little, which causes the double-frequency microseism peak to be higher at the seafloor than the peak of the waves which created it. During the following 2 hours the peak of the long-wave energy moves toward lower frequencies and becomes broad band but centered around 0.6 Hz. This indicates that lower-frequency wave trains are becoming bidirectional, which is in agreement with the findings of Young *et al.* [1987]. This data set (October 18, 2200 UT–October 19, 0000 UT) labeled 10/18/22:00 indicates a 0.3-Hz peak which could be a combination of the long-wave microseisms and the new wind-driven surface waves which slightly affect the bottom at 0.3 Hz. The directional spectra plot does not yet notice this surface wave energy, however. The next vertical seismometer power spectra line, 19:00:00 (October 19, 0000–0200 UT), corresponds to the bidirectional seas which are represented in Figure 4. The surface waves show two directions of propagation near 0.2 Hz. Figure 6 indicates a strong double-frequency peak centered at 0.4 Hz for the 19:02:00 data set. Where the previous microseismic energy could only be assumed to be double frequency, for this data set it has been shown that bidirectional seas exist at half the frequency of the intense 0.4-Hz microseismic peak, corroborating the theory of Longuet-Higgins. In this time segment the gravity wave peak of the new wind energy begins to merge with the peak of the spectra. The double-frequency peak (centered at 0.4 Hz) is

of the same order of magnitude as the spectral peak. During the following 10 hours the long-wave energy peak settles to approximately 0.3 Hz and narrows to a band width of less than 0.1 Hz. The energy level where the seas are bidirectional (0.15–0.2 Hz for these data sets) is very low, yet the energy this produces through nonlinear interactions is of the same order of magnitude on the seafloor as the peak of the spectra. The ocean acts as a natural filter in which very small amounts of long-wave energy can dominate the higher-frequency bands. In the deep ocean this long-wave, double-frequency energy is the major source of ambient noise in the 0.1–1.0 Hz frequency range because other wave-induced sources are attenuated to zero.

To understand the time evolution of the microseismic energy, a more detailed graph of the power spectra of the Joanna vertical seismometer signal is given in Figure 7. This figure shows spectral information from October 15, 1800 UT to October 19, 2000 UT for two hundred 30-minute intervals. The intensity ranges from 10^{-7} $(\text{m/s}^2)^2/\text{Hz}$ (black) to 10^{-12} $(\text{m/s}^2)^2/\text{Hz}$ (white). The x axis is frequency in hertz, while the y axis is time in hours, where October 15, 1800 UT is the zero hour. Therefore the time when it was shown that bidirectional seas existed in Figure 4, October 19, 0030 UT, is represented at 78.5 hours on this graph. The main features on this figure are the band of gravity wave energy from 0.05–0.3 Hz and the streaks of double-frequency energy at approximately 5 and 75 hours. While there is more energy in the frequency band above 0.5 Hz than was seen in other weeks, the two high-energy double-frequency features from 5–10 hours and 75–90 hours dominate this band. In Figure 7 the shift from high to low frequency of the passing event is

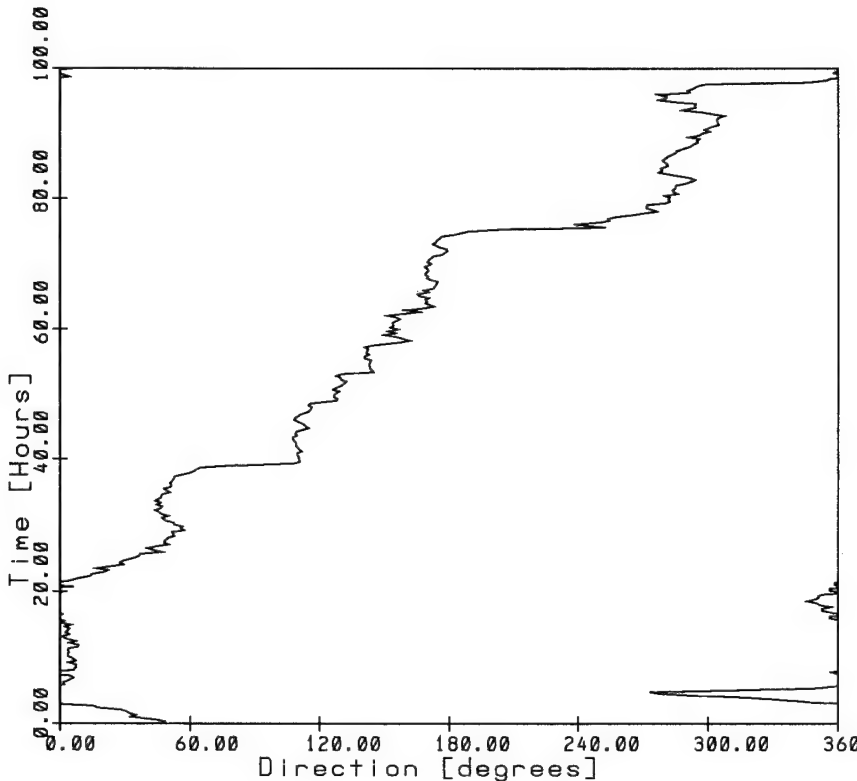


Figure 8. Wind data for October 15, 1800 UT to October 19, 2000 UT collected from the FRF's pier gauges.

readily apparent by the curved nature of the streak. The double-frequency energy increases dramatically at 75 hours at high frequencies, which is precisely when the wind begins to shift, as seen in Figure 8 (the same October wind conditions as in Figure 3 with the October 15, 1800 UT–October 19, 2000 UT data blown up to match Figure 7). As the wind shifts from southerly to northwesterly, the long-wave energy develops.

It is of interest to also look at the power spectra from horizontal units to inspect for differences from the vertical to the horizontal plane. Figure 9 displays the power spectra of the transverse seismometer of the Joanna unit for the same 100-hour time frame beginning October 15, 1800 UT. The energy scale for the vertical, transverse, and radial seismometers will remain constant ($10^{-7} \text{ (m/s}^2)^2/\text{Hz}$ to $10^{-12} \text{ (m/s}^2)^2/\text{Hz}$) throughout this paper. The energy measured by the transverse accelerometer closely matches that of the vertical and the events at 5 and 75 hours are clearly evident. Figure 10 depicts the same 100-hour data set beginning at October 15, 1800 UT for the power spectra of the radial seismometer in the Joanna instrument. Because this seismometer is oriented nearly parallel to shore, very little energy is measured during periods of onshore swell as seen between the twenty-fifth and seventy-fifth hours. The energy between 0.3 and 0.4 Hz near 70 hours now becomes apparent (it can also be seen in the vertical and transverse spectra, but stands out against the lower background energy in this figure). This energy exists well before the major wind shift at 75 hours and remains nearly unchanged until the double-frequency energy curve caused by the new bidirectional sea overwhelms it at approximately 79 hours.

One advantage to having a wide aperture array of OBS units buried at the SAMSON site was that spatial coherence and phase between instruments could be calculated. Figure 2 showed the relative positions of each instrument with respect to shore. Distances between instruments ranged from 183 m (Joanna–Miyuki) to 647 m (Joanna–Wendy). Figure 11 displays the spatial coherence and phase between midrange (≈ 400 m) units Joanna and Beth for the 2-hour data set terminating at October 18, 2000 UT. The gravity waves near 0.06 Hz are coherent with respect to these instruments, with the double-frequency energy showing good coherence from 0.3 to approximately 0.7 Hz. According to Figure 6, energy in the frequency band 0.4–1.0 Hz was low compared to other frequency bands and also compared to later data sets; however, the coherence between instruments remains high. The wave energy from 0.3 to 0.35 Hz is also coherent. Figure 12 (October 19, 0200 UT) indicates an increase in coherence from approximately 0.65 to 0.90 for energy in the frequency band centered at 0.4 Hz (0.3–0.5 Hz). As the microseismic energy level increases in a frequency band, the coherence between instruments generally increases also.

In order to see more detail in the spatial coherence and phase, Figures 13–16 have been included. These figures show coherence and phase between instruments for 200 thirty-minute data sets beginning at October 15, 1800 UT. Figure 13 depicts the coherence between vertical seismometers in the Joanna and Beth units (separation distance, 400 m). The x axis represents frequency from 0.0 to 1.0 Hz and the y axis is time in hours where October 15, 1800 UT is the zero hour. The scale ranges from a coherence of 0.0 (white) to 1.0 (black). Although some coherence exists throughout

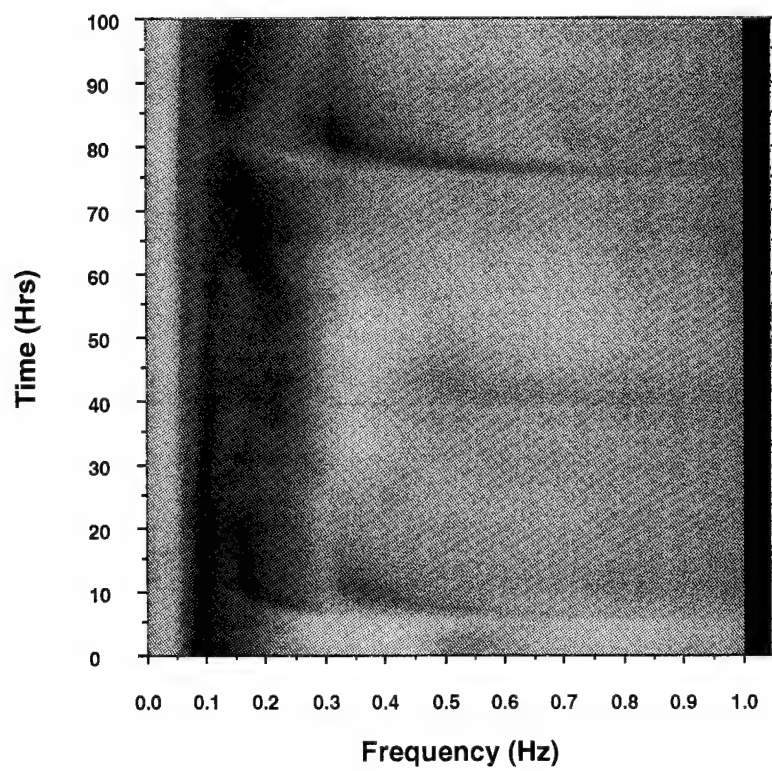


Figure 9. Transverse seismometer power spectra versus frequency for the Joanna unit time periods October 15, 1800 UT to October 19, 2000 UT.

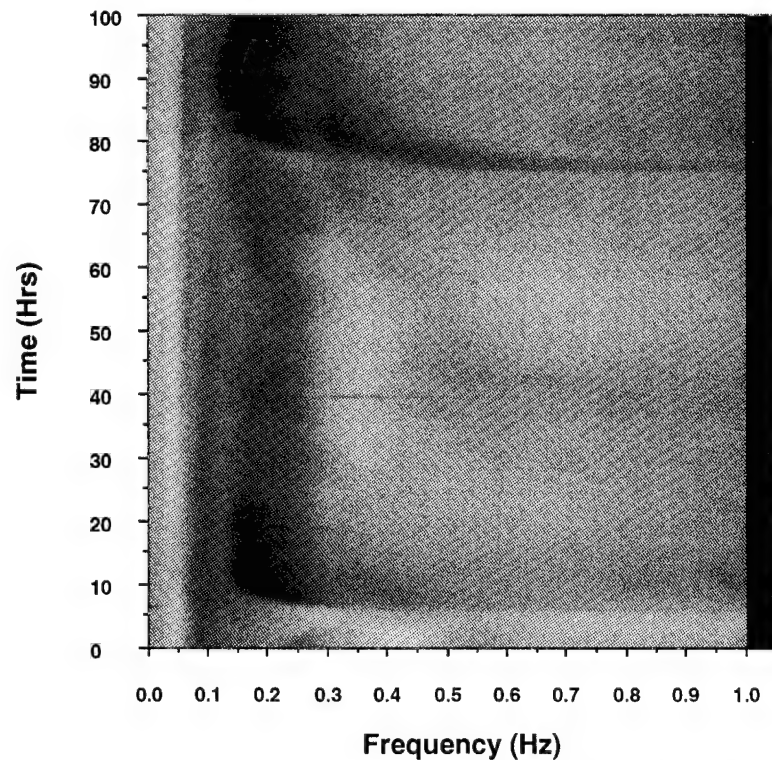


Figure 10. Radial seismometer power spectra versus frequency for the Joanna unit time periods October 15, 1800 UT to October 19, 2000 UT.

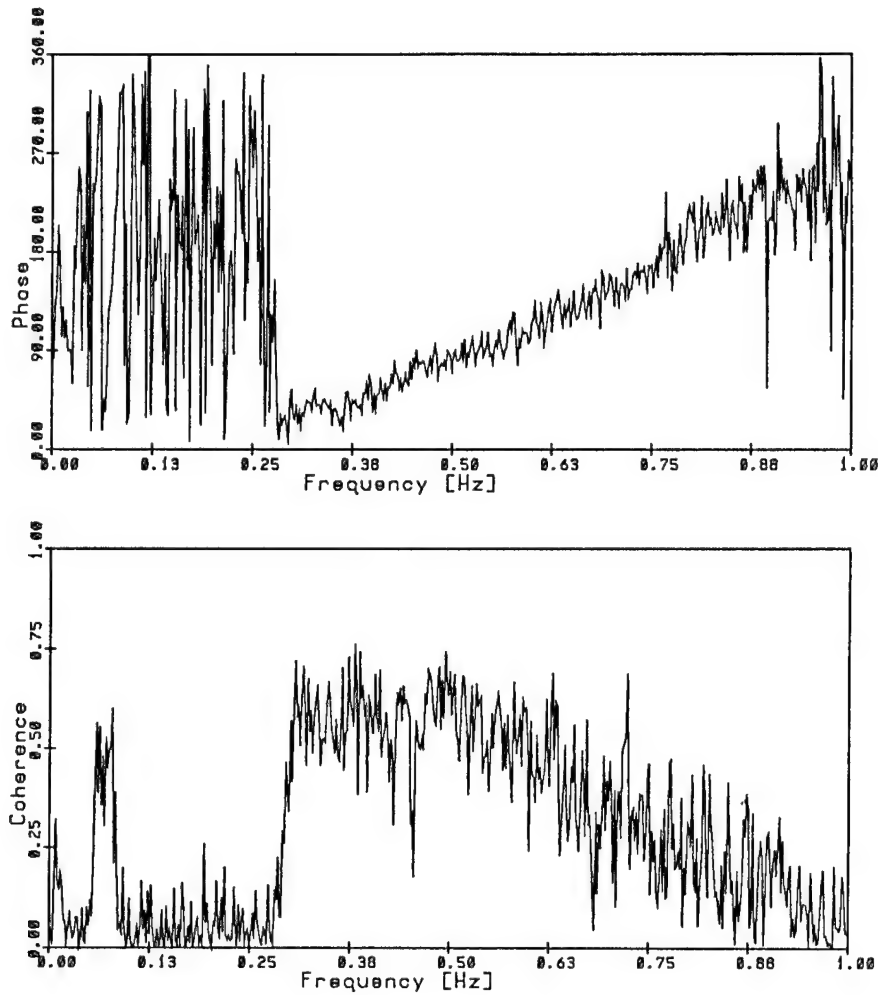


Figure 11. Phase and coherence between the vertical seismometers in the Joanna and Beth units for the 2-hour data set terminating at October 18, 2000 UT.

the 4-day period, the two measured bidirectional events at 5–10 hours and 75–90 hours stand out. The shorter-wavelength gravity wave band (0.1–0.3 Hz) has zero coherence across this distance. However, the swell energy at 0.06 Hz is slightly coherent (0.06-Hz waves have a wavelength of 400 m in this water depth). The long-wave, double-frequency microseismic energy shows good coherence down to nearly 0.25 Hz at 85 hours. At 75 hours (October 18, 2100 UT), there is good spatial coherence at 0.3 Hz which is an indication that the energy measured in this frequency band in Figures 6, 7, 9, and 10 during the late evening of October 18 is not due to the relatively short wavelength gravity waves. Figure 14 shows the spatial phase between the Joanna and Beth vertical seismometers for the 100-hour time frame starting at October 15, 1800 UT. Phase between signals range from 0° (white) to 359° (black). This plot indicates that the phase between these two signals is steady throughout the 4-day period. The phase is near 0° in the 0.3 Hz range and increases slightly with increasing frequency to 0.75 Hz, which is an indication of higher-frequency microseisms having shorter wavelengths. At the swell frequency (near 0.05 Hz) and to a lesser extent the gravity wave frequencies (0.1–0.25 Hz) the phase is banded, indicating wavelengths shorter than the separation distance repeating all phases with

increasing frequency. Between 70 and 75 hours and at 0.3 Hz, however, the phase is stable, which again is an indication of long-wave propagation. The two bidirectional sea events at 5–10 and 75–90 hours are noticed as a slight change toward lower phase. It follows that the direction in which these events propagate is not wildly different than the low-energy propagation of the entire 4 days.

Figure 15 shows the coherence between the Joanna vertical seismometer and the Miyuki vertical seismometer (separation distance = 180 m). Although the units are much closer, because they lie roughly parallel to shore, the swell energy near 0.05 Hz is not coherent, as it was in Figure 13 between Joanna and Beth. The two strongly coherent events lie between 0–10 hours and 75–90 hours. The most notable feature being the curve to lower frequency (0.25 Hz) of the strongly coherent 75–90 hour event. Figure 16 displays the spatial phase between the same two instruments. The scale now ranges from -180° (white) to +180° (black) with the 0° phase being indicated by the grey of the border. The phase between these two signals is generally zero with very little frequency dependence. The banded nature of the gravity wave frequency band is again apparent as is the hourglass shape on the left-hand side as the event passes to lower frequencies. The dark streak at 75 hours indicates a positive

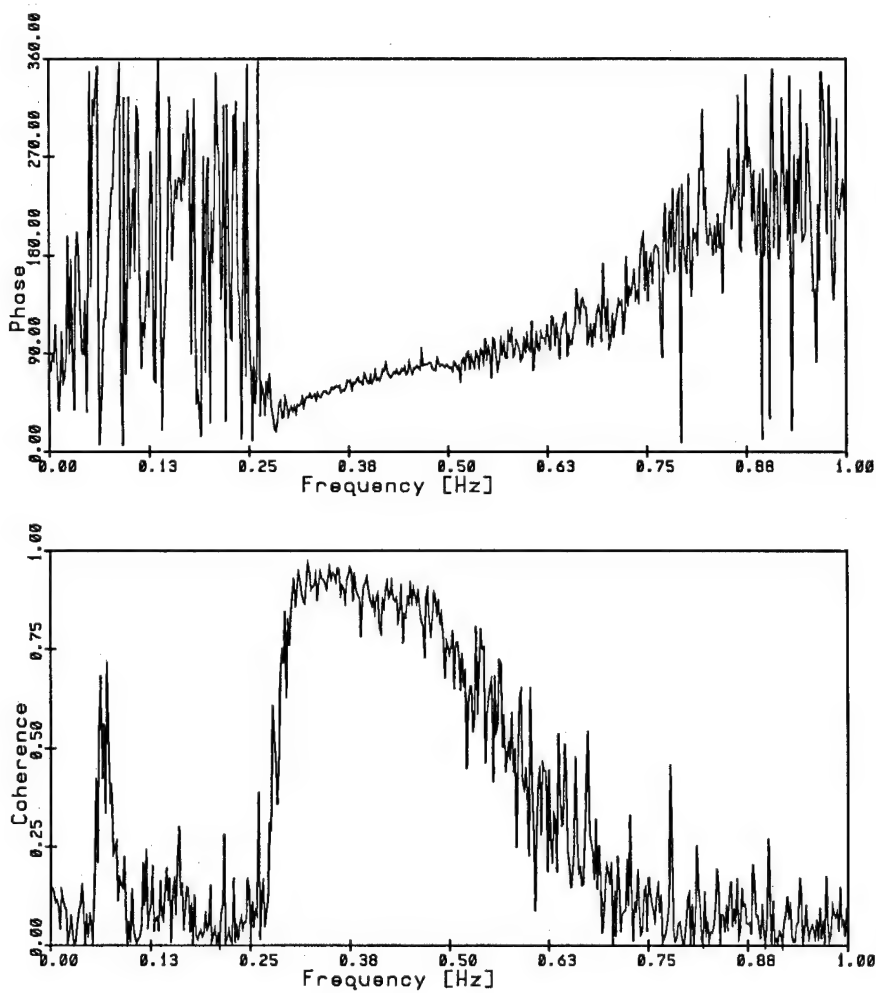


Figure 12. Coherence and phase between the vertical seismometers in the Joanna and Beth units for the 2-hour data set terminating at October 19, 0200 UT.

phase swing as the double frequency event passes by. Also, the energy at 0.3 Hz and 75 hours is characterized by steady phase, again indicating long-wave energy. The general nature of the spatial coherence and phase indicates that finding the directional spectra of this long-wave energy is possible, and given the very high coherence, the spectra plots should have good resolution to the limits of the response function of the array.

The array of four OBS units (Joanna, Miyuki, Beth, and Wendy) is used to estimate the directional spectra of seafloor, double-frequency microseisms during the SAMSON experiment. An ideal array would require an infinite number of cross spectra between instruments with varying spatial lags. Because only four units are available the response of this array has significant sidelobes and a broad primary lobe [Nye, 1992]. The response, however, is sufficient to show propagation directions of the long-wave energy in order to complete the analysis of microseism generation due to bidirectional sea states. In his thesis, *Goodman* [1990] describes the maximum likelihood method (MLM) algorithm used to find the following spectra. He also suggested that beam forming be used instead of MLM in cases where the cross spectrum is noisy. Beam forming was tried and found unfavorable in comparison to MLM's resolution (the cross

spectra show high coherence, low noise for these data). Therefore the long-wave directional spectra estimates are calculated by MLM.

It has previously been estimated that the propagation direction of the long-wave energy should be 245° for 0.32-Hz energy during the 30-minute time frame starting at October 19, 0230 UT. This was based upon Longuet-Higgins' theory that the arms of the bidirectional sea add to produce the propagation direction of the double frequency energy. Figure 17 presents the directional spectra of this double frequency energy for four frequency bands. From upper left to lower right the estimated spectra are centered around f_0 equal to 0.3, 0.4, 0.5, and 0.6 Hz. The spectrum is averaged over $\Delta f = 0.02$ Hz for f_0 equal to 0.3 and 0.4 Hz, and $\Delta f = 0.04$ Hz for f_0 equal to 0.5 and 0.6 Hz because the lower frequencies tended to have higher coherence (less noise) than the higher frequencies. Each graph displays wave direction of propagation versus phase speed (meters per second). The algorithm varies phase speed (c) and calculates wavenumber (k) as $k = 2\pi f_0/c$. The directional spread is found for each value of c to find the most likely direction and speed. For small c , and therefore small wavelength, spatial aliasing can occur in the higher-frequency graphs. The contours are normalized by the maximum of each graph and

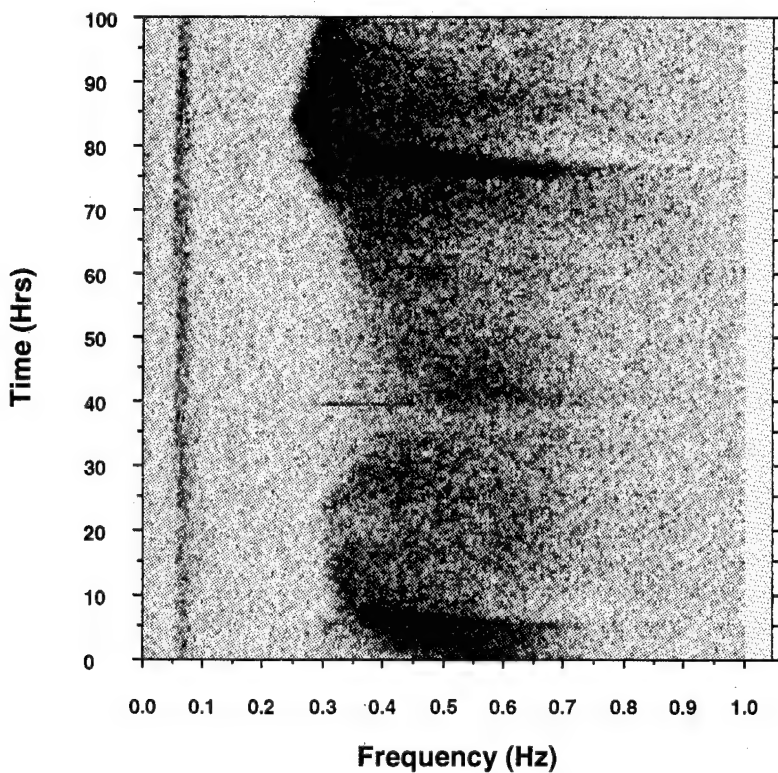


Figure 13. Spatial coherence between Joanna and Beth's vertical seismometers (400 m apart) versus frequency for time periods October 15, 1800 UT to October 19, 2000 UT.

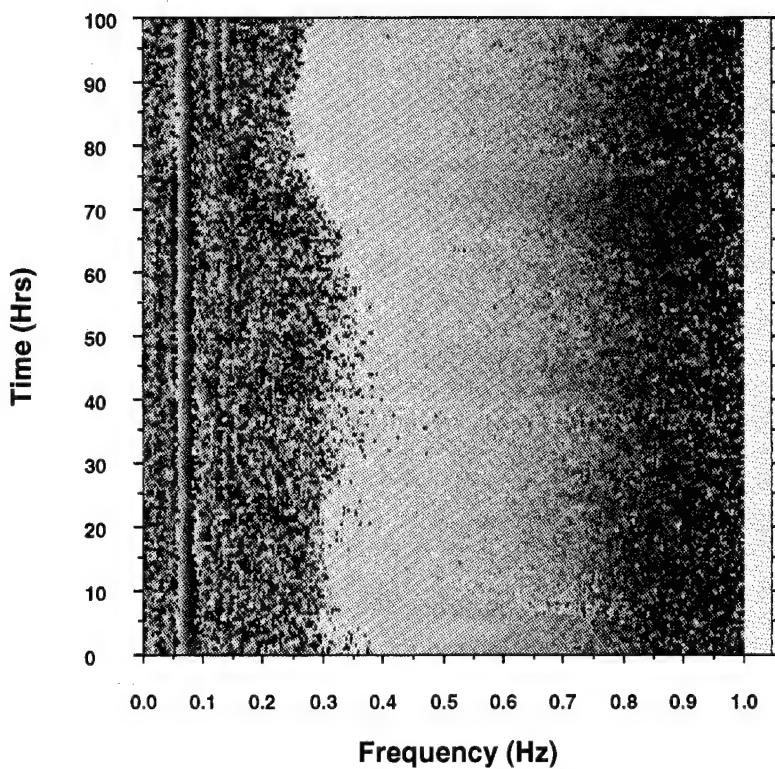


Figure 14. Spatial phase between Joanna and Beth's vertical seismometers (400 m apart) versus frequency for time periods October 15, 1800 UT to October 19, 2000 UT.

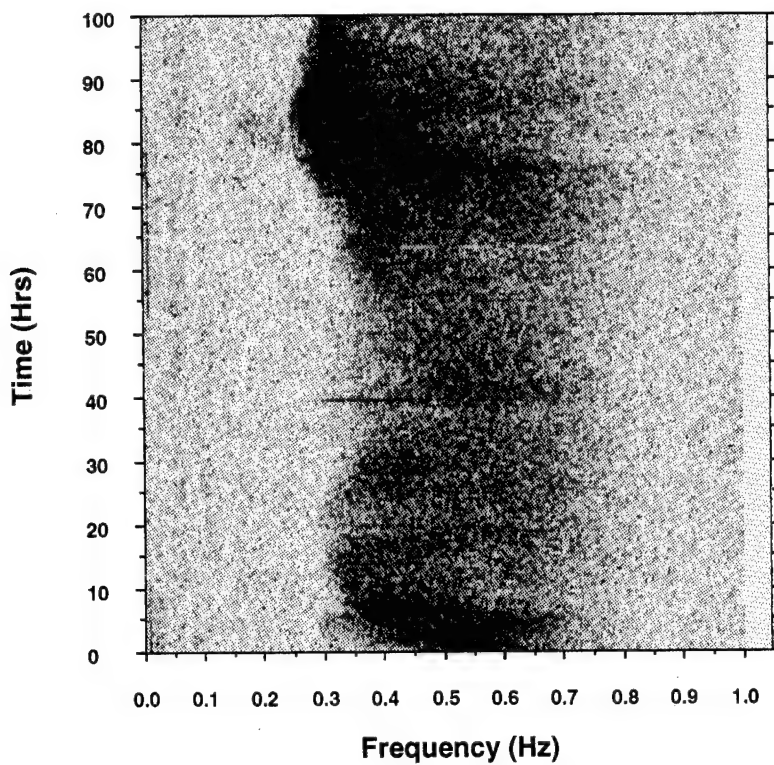


Figure 15. Spatial coherence between Joanna and Miyuki's vertical seismometers (180 m apart) versus frequency for time periods October 15, 1800 UT to October 19, 2000 UT.

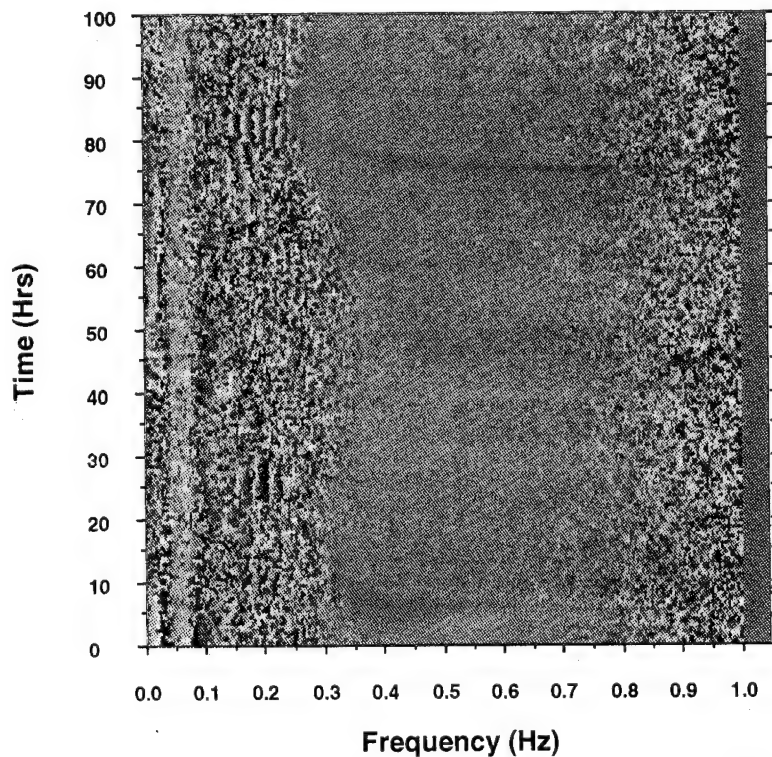


Figure 16. Spatial phase between Joanna and Miyuki's vertical seismometers (180 m apart) versus frequency for time periods October 15, 1800 UT to October 19, 2000 UT.

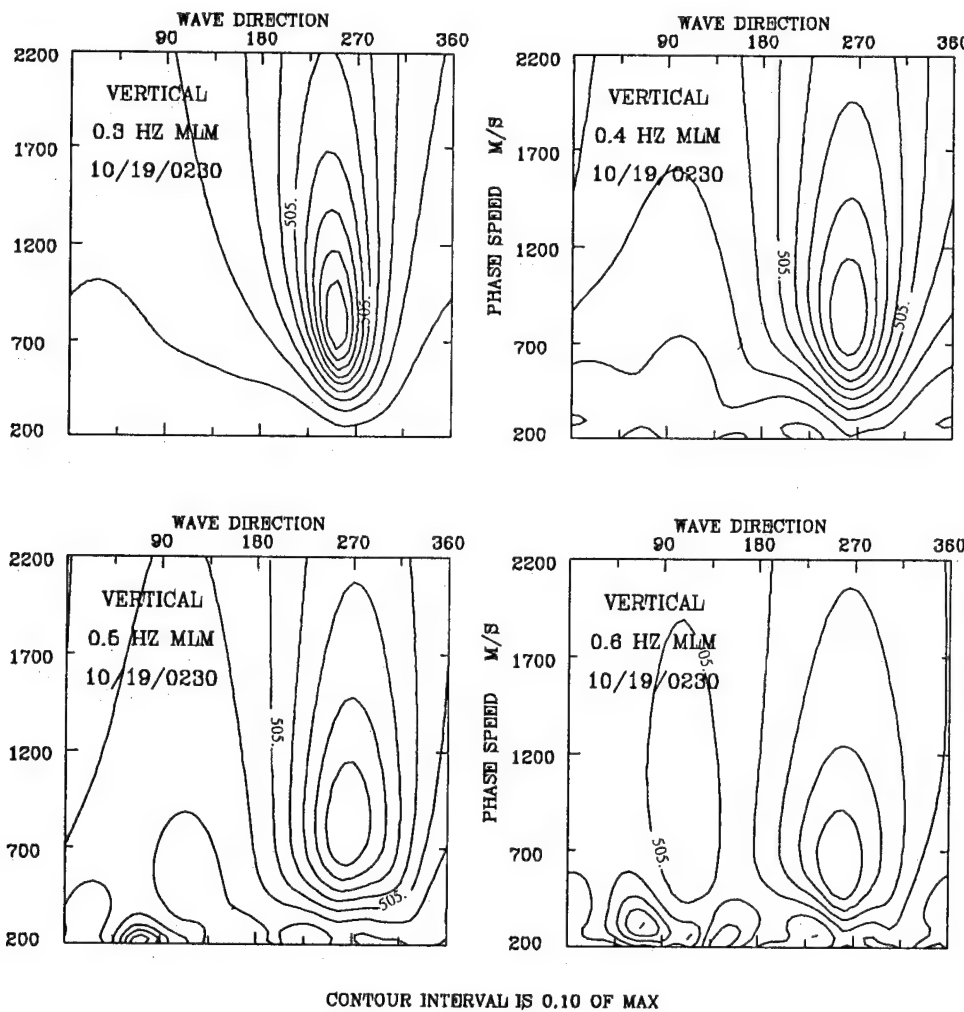


Figure 17. Double-frequency directional spectra estimation from the vertical seismometer four-point array using the maximum likelihood method during the 30-minute data set beginning at October 19, 0230 UT for frequency bands centered at 0.3, 0.4, 0.5, and 0.6 Hz, respectively, from upper left to lower right.

the contours are given in tenths of the maximum. Figure 17 indicates that the most likely propagation direction of the 0.3 Hz energy is 250° at a phase speed of 850 m/s, which closely agrees with the vector sum of the opposing seas which was estimated at 245°. The next frequency investigated was 0.4 Hz which shows a maximum at 260°, 900 m/s but is less sharp than the 0.3-Hz case. The higher-frequency cases, 0.5 Hz and 0.6 Hz, show maxima at 270°, 900 m/s and 260°, 700 m/s, respectively, with the resolution decreasing in each case. Some spatial aliasing can be seen at very low phase speeds on these graphs, which can be ignored. This time period represents the double-frequency event, as it was well established in the gravity wave band. However, investigating further back in the progression of this event, where the bidirectional sea state cannot be measured at the ocean floor but only assumed, the directional spectra graphs of Figure 18 are produced. This figure shows four frequency bands, 0.3, 0.4, 0.5, and 0.6 Hz with the same band widths as the Figure 17. In this case, at October 18, 2200 UT, the resolution in all four frequency bands are approximately equal. The 0.5 Hz and the 0.6 Hz bands at 230°, 650 m/s and 245°, 650 m/s, respectively, most likely are the summation of the opposing

vectors of the new wind and old wind-driven energy. The more southerly direction of propagation coincides with the north winds, which would most likely create high-frequency surface waves traveling toward 180°. At the lower frequencies is the result of the long-wave energy from 0.3 to 0.4 Hz, which exists before the wind shift event but whose generation mechanism has not been accounted for. The peaks of the 0.3 and 0.4 Hz energy are 270°, 1100 m/s and 260°, 850 m/s, respectively. There is a gradual change between the 0.3 Hz graph presented here and the one from Figure 17, which occurs 4.5 hours later.

In order to substantiate the results from the October 19 event, another data set is investigated. The ocean surface directional spectra plotted in Figure 19 are a representation of the November 29, 1990, 1000 to 1200 UT data from the Joanna unit. The x axis describes direction of wave propagation in azimuthal direction from north, and the y axis is frequency from 0.05–0.35 Hz. The wave energy is normalized by the maximum of each plot and is given in square meters per hertz per radian where the contour interval is tenths of the maximum. The graphs represent 30-minute averages of the data beginning at November 29, 1000, 1030,

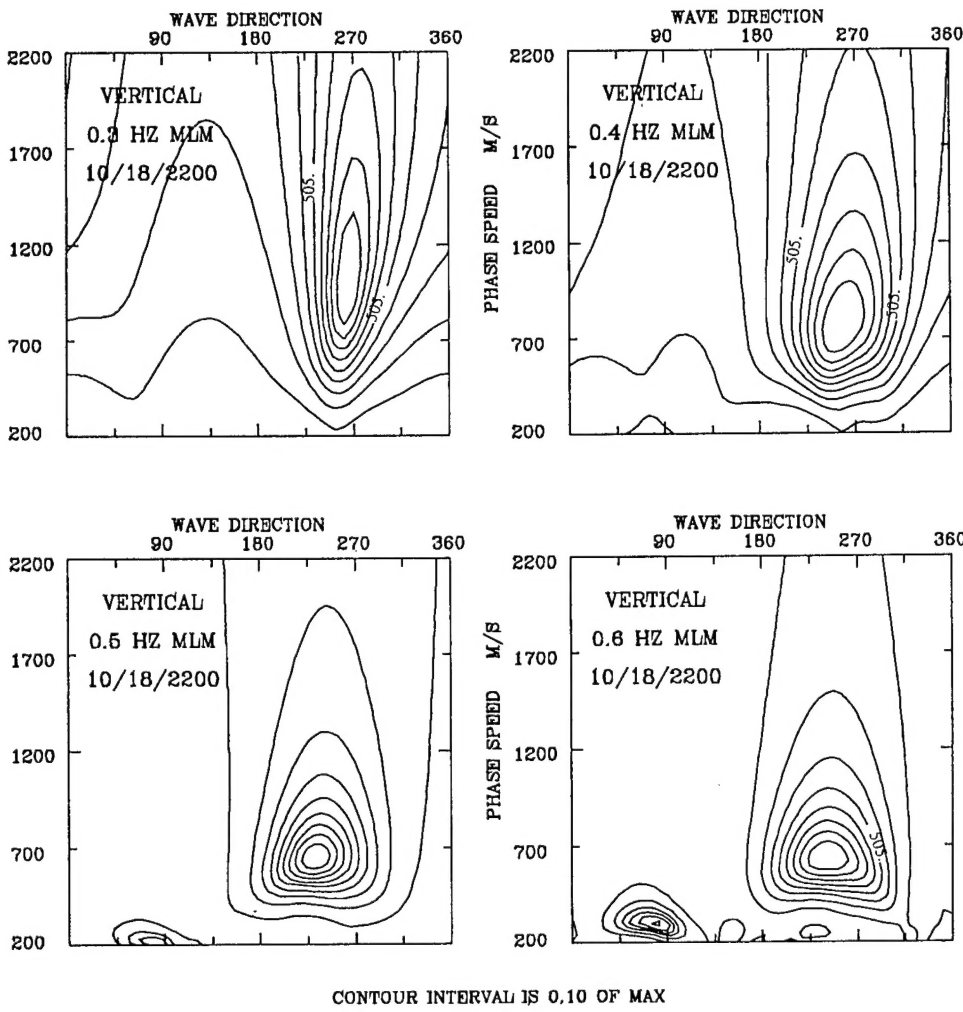


Figure 18. Double-frequency directional spectra estimation from the vertical seismometer four-point array using the maximum likelihood method during the 30-minute data set beginning at October 18, 2200 UT for frequency bands centered at 0.3, 0.4, 0.5, and 0.6 Hz, respectively, from upper left to lower right.

1100, and 1130 UT from upper left to lower right, respectively. The sea state propagating toward 180° near 0.27 Hz in the 11/29/10:00 plot increases in energy, moves to lower frequency, and shifts slightly west of south in the following 1.5 hours. The old energy includes a long-period swell to 270°, 0.06 Hz and a wind-driven peak at 300°, 0.12 Hz, both of which diminish throughout the time frame. An approximate summation of wavenumber vectors for each of the four time periods indicates vectors toward 235° at 0.5 Hz, 250° at 0.36 Hz, 255° at 0.3 Hz, and 245° at 0.28 Hz, respectively.

Figure 20 shows the power spectra of the vertical seismometer of the Joanna unit for the 4-day period beginning at November 28, 1000 UT. The *x* axis represents frequency from 0 to 1 Hz and the *y* axis is time in hours. The time frame discussed in the previous figure, November 29, 1000–1200 UT is represented as 24 to 26 hours. The intensity again ranges from 10^{-7} (m/s^2) $^2/\text{Hz}$ (black) to 10^{-12} (m/s^2) $^2/\text{Hz}$ (white). The double-frequency nature of this energy is clearly evident in Figure 20 as two curves, one with twice the frequency of the other, appear at 24 hours. The wall of microseismic energy has a width of the order of the resolution of this diagram, which is 30 minutes. *Herbers and Guza*

[1992] found the double-frequency energy to increase an order of magnitude in 16 minutes for this same data set.

The array of transverse seismometers is used to find the directional spectra of this double-frequency energy using the MLM algorithm. Figure 21 shows the directional spectra results for the microseism energy in four frequency bins centered at 0.3, 0.4, 0.5, and 0.6 Hz, respectively, from upper left to lower right for the 30-minute time period November 29, 1000 UT. The bin widths are 0.02 Hz around the 0.3 and 0.4 Hz cases and 0.04 Hz around the 0.5 and 0.6 Hz cases. The graphs are in wave direction of travel versus phase speed. The 0.3-Hz case shows little resolution at this time. The 0.4-Hz case indicates the direction of propagation to be 225° at 700 m/s. The 0.5-Hz bin gives 230° at 650 m/s and the 0.6-Hz bin gives 250° at 600 m/s. The 0.5-Hz graph has the tightest resolution and matches the prediction from the vector sum of the opposing seas to 5°. The final 30-minute data set in this period of interest (November 29, 1130 UT) is given in Figure 22. Here the 0.3-Hz frequency band indicates spectra at 255° at 900 m/s, which is within 10° of the predicted vector (the energy in this frequency band competes with the higher-frequency gravity waves and therefore

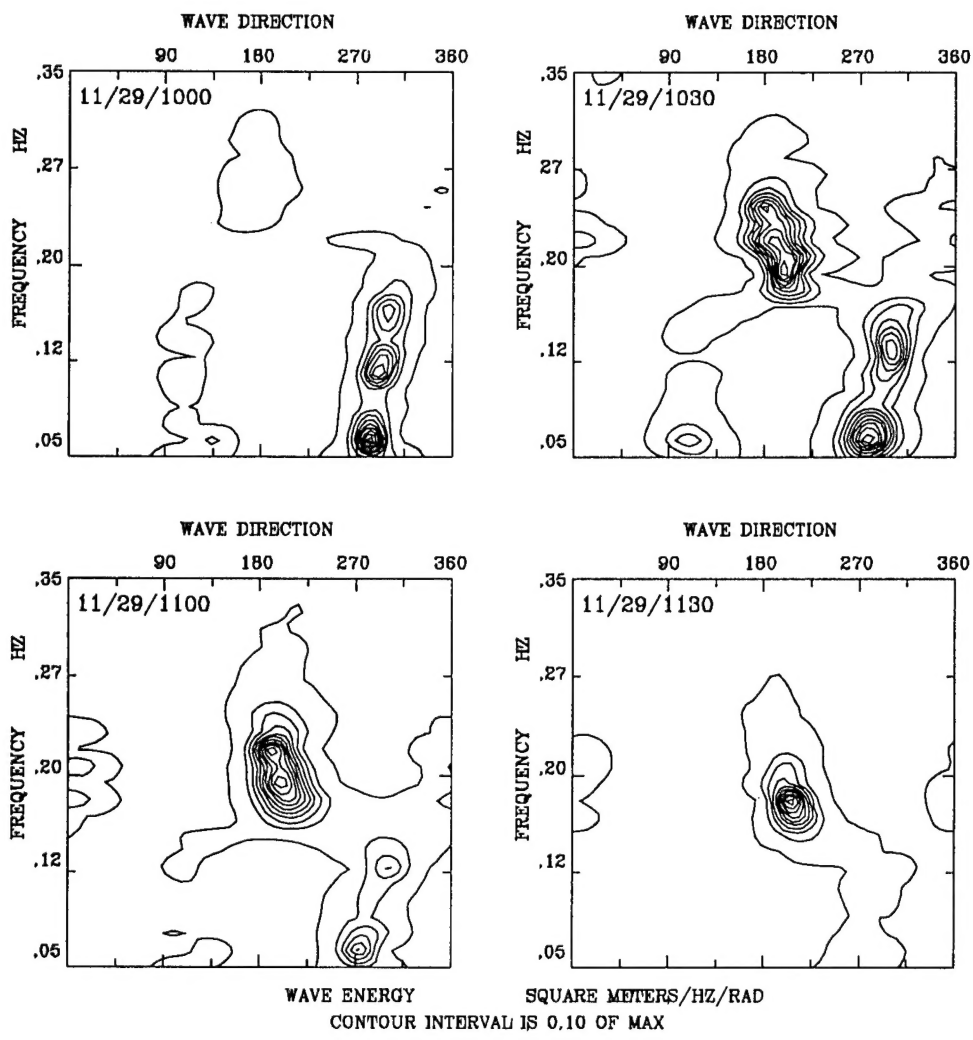


Figure 19. Ocean surface directional spectra results from the 1990 SAMSON experiment for the Joanna unit for four 30-minute time periods beginning November 29, 1000, 1030, 1100, and 1130 UT, respectively.

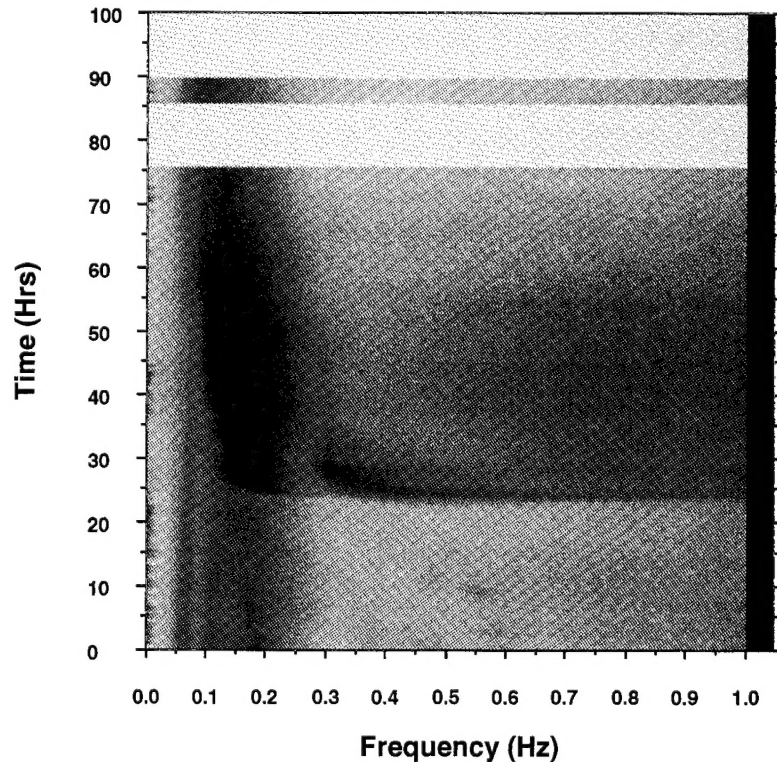


Figure 20. Vertical seismometer power spectra versus frequency for the Joanna unit time periods November 28, 1000 UT to December 2, 0200 UT.

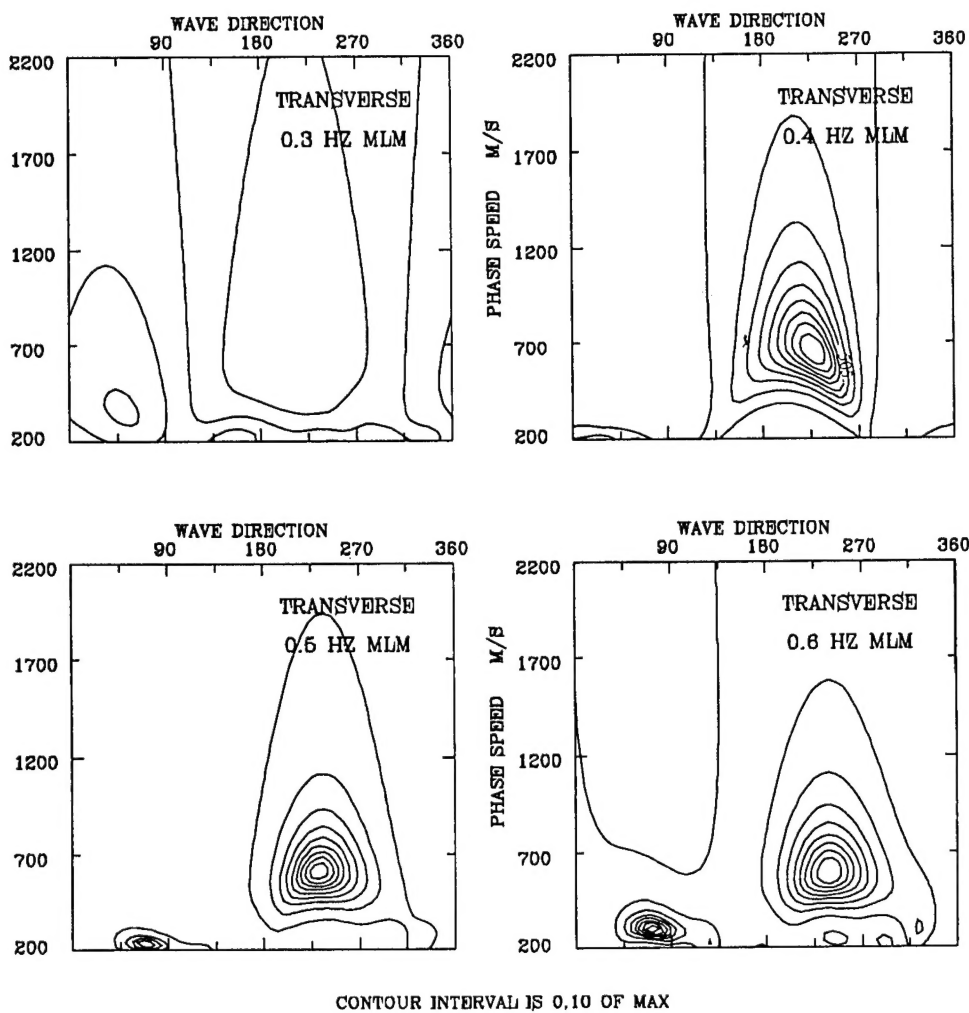


Figure 21. Double-frequency directional spectra estimation from the transverse seismometer four-point array using the maximum likelihood method during the 30-minute data set beginning at November 29, 1000 UT for frequency bands centered at 0.3, 0.4, 0.5, and 0.6 Hz, respectively, from upper left to lower right.

tends to have weaker resolution. The 0.4-Hz figure shows 245° at 700 m/s, the 0.5-Hz bin gives the same 245° at 700 m/s, and the 0.6-Hz bin shows 250° at 700 m/s. In general, the spectral peak moves from higher to lower frequency with time and to a more westerly direction, as was predicted by the bidirectional sea state. *Herbers and Guza* [1992] have also shown that the wavenumber vectors of the opposing arms of the bidirectional seas sum to a vector in the same direction as the direction of propagation of the long-wave, double-frequency energy in this data set.

Discussion and Conclusion

During the SAMSON experiment, concurrent measurements of surface wave directional spectra and double-frequency, long-wave microseisms were made. The results indicate that long-wave energy rapidly develops during periods of shifting winds which create bidirectional sea states. Theoretically, nonlinear sum interactions of opposing wavenumber vectors of approximately the same frequency create long-wave energy at twice the frequency, which is only slightly attenuated in shallow water. Bidirectional sea states have been found using the buried OBS measuring system,

during which the long-wave energy has been measured at double frequencies. As the wind shifts, this energy forms at high frequencies and moves to lower frequencies following the single-frequency (surface wave) energy in a 2:1 ratio. Because of the insignificant attenuation the measured energy levels of the double-frequency microseisms at the seafloor are of the same order of magnitude as the single-frequency, surface wave energy induced seafloor motion. Indeed, very little energy needs to be directionally opposing to create long-wave energy at measurable levels, because this energy dominates the 0.4–1.0-Hz frequency bands in the water depths of the study area. All other locally generated sources of microseisms do not reach the bottom in this frequency band.

The double frequency microseism energy has been found to be coherent between vertical seismometers across the array with steady phase. Some coherence exists even during periods of low energy in the double-frequency band. However, the coherence increases dramatically during bidirectional sea events. The phase can also change during the event depending upon the direction of the double-frequency energy. The horizontally oriented seismometers also show good coherence with similar phase. The directional spectrum

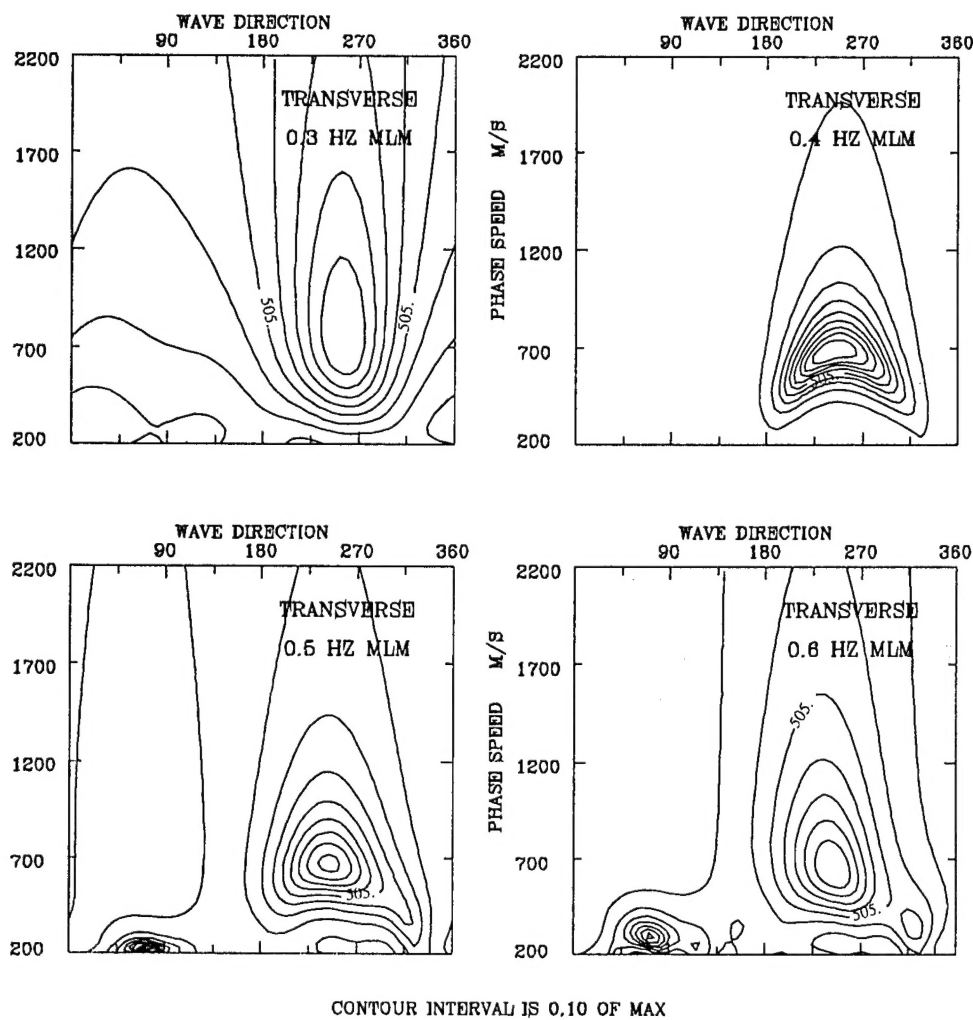


Figure 22. Double-frequency directional spectra estimation from the transverse seismometer four-point array using the maximum likelihood method during the 30-minute data set beginning at November 29, 1130 UT for frequency bands centered at 0.3, 0.4, 0.5, and 0.6 Hz, respectively, from upper left to lower right.

of the double-frequency energy was found using the four-point array with the maximum likelihood method. Various data sets were analyzed to confirm Longuet-Higgins' theory which proposes that the propagation direction of double-frequency microseisms occurs in the direction of the vector sum of the opposing single-frequency seas.

Acknowledgments. This work was supported under several Office of Naval Research contracts between 1990 and 1993 in the sections of Ocean Acoustics and Geology and Geophysics. I would also like to thank the staff of the Field Research Facility of the Army Corps of Engineers in Duck, North Carolina, headed by Bill Berkemeyer and the crew of the R/V *Cape Henlopen* out of the University of Delaware.

References

Goodman, D., Analysis and observations of spatially coherent seafloor microseisms, Ph.D. dissertation, Univ. of Miami, Fla., 1990.

Herbers, T., and R. Guza, Wind-wave nonlinearity observed at the seafloor, I, Forced-wave energy, *J. Phys. Oceanogr.*, 21, 1740-1761, 1991.

Herbers, T., and R. Guza, Veering winds, directionally opposing seas, and double-frequency pressure fluctuations at the sea floor, *J. Acoust. Soc. Am.*, 91(4), 2345, 1992.

Longuet-Higgins, M. S., A theory of the origin of microseisms, *Philos. Trans. R. Soc. London, A*, A243, 1, 1950.

Miche, M., Movements Ondulatoires de la Mer en Profondeur Constante ou Decroissante, *Ann. Ponts. Chaussées*, 114, 25-406, 1944.

Nye, T., Measurements of the directional spectra of surface gravity waves and seafloor microseisms using a pressure sensor and two buried horizontal seismometers, Ph.D. dissertation, Univ. of Miami, Fla., 1992.

Nye, T., and T. Yamamoto, Field test of the Buried Ocean Wave Directional Spectrometer (BOWDS) System, *J. Waterw., Port Coastal Ocean Eng.*, in press, 1994.

Young, I. R., S. Hasselman, and K. Hasselman, Computations of the response of a wave spectrum to a sudden change in wind direction, *J. Phys. Oceanogr.*, 17, 1317-1338, 1987.

T. Nye and T. Yamamoto, Division of Applied Marine Physics, RSMAS, University of Miami, 4600 Rickenbacker Causeway, Miami, FL 33149.

(Received August 31, 1993; revised December 2, 1993; accepted February 1, 1994.)